Coordination of hippocampal input and output pathways during sleep-like states

by

Tara Alice Whitten

A thesis submitted in partial fulfillment of the requirements for the degree of

Doctor of Philosophy

Centre for Neuroscience
University of Alberta

Abstract

Hippocampal activity is characterized by two state-dependent, mutually exclusive large-amplitude oscillations: theta (3-12 Hz) and the hippocampal slow oscillation (SO; ~1 Hz). These two rhythms have been implicated in different stages of memory processing. Theta occurs during awake exploratory behaviour and REM sleep, while the hippocampal SO occurs during nonREM sleep and is coordinated with the neocortical SO. Coordination between the neocortex and the hippocampus during the SO is of particular importance because this state has been implicated in sleep-dependent consolidation of hippocampal-dependent memories, and this process likely involves bidirectional communication between these two brain structures. The overall goal of this thesis was to understand how hippocampal input and output pathways are coordinated with neocortical activity during the SO, and to compare hippocampal network patterns during SO and theta oscillations. To approach this question, I used urethane anaesthesia as a model for the activity patterns seen during natural sleep.

In Chapter 2, I present independent component analysis (ICA) as a method to separate the contributions of distinct hippocampal afferent pathways to the local field potential (LFP) recorded in the dorsal hippocampus, and to assess its reliability across different algorithms, epochs and animals. Five components that were consistent across animals were found which likely correspond to the major afferent pathways to the dorsal hippocampus, in addition to a component representing a volume conducted signal from the neocortex. Two potential applications of the ICA approach are discussed, including the removal of artifacts such as the volume conducted portion of the signal, and the detection of oscillatory activity in separated components using a modification of the Better Oscillation (BOSC) detection method.

In Chapter 3, I describe oscillatory activity patterns in the major hippocampal input and output pathways during SO and theta states. During theta, gamma frequency (20-100 Hz) synaptic inputs arriving at CA1 at stratum lacunosum moleculare (SLM) and stratum radiatum (SRad) occur at opposite phases of the theta cycle. During the SO, we found that the gamma-frequency inputs at these layers also arrive at opposite phases with respect to the neocortical SO cycle. Interestingly, we found that synaptic inputs to SLM periodically skip cycles with respect to the neocortical SO, and that this skipping of cycles results in a slowing of the hippocampal SO compared to the neocortical SO. Finally, we found that sharp wave-ripples (SPW-Rs), an activity pattern that has been implicated in the reactivation of firing sequences that might underlie memory consolidation, can occur at two distinct phases with respect to the neocortical slow oscillation. Specifically, SPW-Rs that occur after the peak of the neocortical UP-state were associated with higher power of the neocortical SO than SPW-Rs that precede the peak of the UP-state.

In Chapter 4 I describe a novel ultra-slow (0.1-0.5 Hz) hippocampal oscillation that co-occurs with both theta and the SO and modulates faster activity during both states. This rhythm, which we call iota, has maximal power at SLM and a phase reversal 100 μm below the theta phase reversal. Inactivation of the medial septum (MS), which abolishes theta oscillations, significantly amplifies the iota rhythm during activated states. Interestingly, inactivation of the MS with lidocaine, but not muscimol, disrupted the hippocampal SO as well, and led to an iota-like but arrhythmic activity pattern that remained phase-modulated by the neocortical SO. This important finding suggests that fibers passing in the vicinity of the medial septum are critical for the expression of the hippocampal SO. During spontaneous activity, iota in the superficial layers of the entorhinal cortex was highly coherent

with iota in the hippocampus, and the maximum iota-related multi-unit activity occurred in entorhinal cortex layer III, which projects directly to SLM. These results suggest that iota might be a default state of entorhinal-hippocampal networks that influences hippocampal processing during both states.

Taken together, the results in this thesis show that the coordination of hippocampal circuits with the neocortex during the SO is dynamic, likely involves the integration of entorhinal and non-entorhinal inputs at SLM, and can be modified based on the strength of the neocortical SO.

Preface

In addition to data that I collected, the work presented in Chapters 2-4 of this thesis includes data collected by Trish Wolansky and Jon Kerber. The work presented in Chapter 4 was a project initially led by Zahid Padamsey, and includes data collected by Trish Wolansky, Zahid Padamsey and Phillip de Guzman. Trish made the initial observations of iota activity following medial septal inactivation with lidocaine, as noted in her lab book: ‛at about 0.25 Hz, there is a "dip" in the RHPC static trace (a "not-so-sharp" sharp wave or something).’ Zahid followed up on this observation and collected data on hippocampal activity following muscimol-inactivation of the medial septum. I completed the project by integrating the septal inactivation data with evidence for iota during spontaneous activity in the hippocampus and entorhinal cortex, as well as using ICA to evaluate the effect of septal inactivation on the synaptic inputs to SLM specifically. I was responsible for all final analyses and writing presented in Chapter 4.

In all other cases, the ideas, data and analysis presented here are my own, developed in collaboration with my supervisor, Dr. Clayton Dickson. This thesis was a part of a larger project that received ethics approval from the University of Alberta Biosciences Animal Care and Use Committee (AUP00000092_AME1; Project name: Cellular and Network Dynamics of Neo- and Limbic-Cortical Brain Structures).

Now this is very profound, what rhythm is, and
goes far deeper than any words. A sight, an
emotion, creates this wave in the mind, long before
it makes words to fit it

Virginia Woolf, 1926

From personal letters collected in Woolf et al. (1975)

Acknowledgements

The work in this thesis was supported by a Natural Science and Engineering Council of Canada (NSERC) grant #249861 to Clayton Dickson. I was additionally supported by an Izaak Walton Killam Memorial Graduate Scholarship, an Alberta Innovates – Technology Futures Graduate Scholarship and an NSERC Alexander Graham Bell Canada Graduate Scholarship – Doctoral (CGS D).

I would like to acknowledge the guidance and support provided by my supervisor, Dr. Clayton Dickson. Throughout my tenure in his lab, which began many years ago as an undergraduate student, Clayton has seen me at my best and at my worst, but has always believed in my abilities and pushed me just far enough to bring out my best. I have appreciated his passion for understanding the mysteries of the hippocampus. In many cases Clayton's insights and intuition about my project provided the critical element necessary for untangling the most intractable problems, even in cases when I didn't believe him at first. My path through graduate school was not typical, and I also appreciate Clayton's support when I left to pursue other goals. Clayton is a supervisor who understands and cares for his students as people first and scientists second.

I would also like to acknowledge the help of my supervisory committee, Dr. Kelvin Jones and Dr. Jeremy Caplan. The analysis methods that I learned in Jeremy's lab shaped much of my approach to the work in this thesis, and Kelvin's reading suggestions challenged me to better understand my methods in particular and the theory of oscillatory processes in general.

My own as well as several other projects have stemmed from the work of a former student in the Brain Rhythms lab, Dr. Trish Wolansky, whose tireless and Herculean efforts in the lab still leave me in awe. I have had the good fortune to use some of the data she collected, and her attention to detail and meticulous notes have been of incredible value. I would also like to acknowledge all past and current members of the Brain Rhythms Lab whom I have had the good fortune to know and work alongside. Countless conversations over the years with fellow lab members have helped to shape the ideas that have ended up in this thesis. Furthermore, though people have come and gone, the lab as always maintained a healthy balance between a passion for neuroscience and a good amount of fun. It has been an environment that I will be sad to leave.

I would like to acknowledge the support of my parents, David and Deborah Whitten, who gave me the belief that I could accomplish any goal, and who fostered my curiosity, which led to my interest in understanding the brain. Finally, thank-you also to Tanya Dubnicoff, who put up with my obsessiveness and many near-breakdowns in the last 6 weeks of preparing this thesis, and without whose support I might never have finished.

Table of Contents

Table of Figures

List of Tables

1 **Introduction**

Introduction

When Virginia Woolf wrote, in 1926, that '*a sight or an emotion creates this wave in the mind'* (from personal letters collected in Woolf et al., 1975), it is unlikely that she was referring to neuronal oscillations. Rhythms of the human electroencephalogram had yet to be described (Berger, 1929). In fact, Woolf was born in 1882, just 7 years after Richard Caton first reported on the electric currents recorded with a galvanometer from the brain of the rabbit and the monkey. In the British Medical Journal (1875), Caton wrote presciently that '*the electric currents of the grey matter appear to have a relation to its function'*. Even in this first report, Caton described '*feeble currents of varying direction passing through the multiplier when electrodes are placed at two points of the external surface'*. Thus, the first description of visible fluctuations of neural activity accompanied the first description of the electric currents themselves. Neuronal oscillations across a vast range of time scales have proven to be fundamental to the operation of the nervous system (Buzsaki, 2006). It is therefore not surprising that rhythms in the environment, such as the beat of a drum, or the waves of the sea, affect us so profoundly. Our experience of the world is shaped by the brain processes that allow us to perceive it, and our conscious experience can indeed feel like Woolf's '*wave in the mind'*.

In the proceeding pages, I will present background that is important for my thesis work as well as ideas that have shaped my conception of brain function. In section 1.2 I will discuss the importance of synchrony in the nervous system, and the role of rhythmic oscillations in mediating that synchrony, with a particular focus on gamma oscillations. In section 1.3 I will focus in particular on rhythms that are prominent while we sleep, as well as recent evidence that certain stages of sleep are critical for strengthening hippocampal-dependent memories. This will bring me to a description in section 1.4 of the hippocampus itself, including its role in memory, its anatomical connections, and its oscillations during sleep. Finally, in section 1.5 I will briefly overview the methods that I have used to study these oscillations, and the work I have done to understand the oscillatory dynamics in the functional hippocampal networks that underlie memory.

1.1 Oscillations and synchrony in neural systems

There exist two possibilities for how information is encoded in the nervous system: through the rate of neuronal firing, or through the precise timing of each spike. The importance of precise timing in certain forms of synaptic plasticity (Roberts and Bell, 2002) suggested that the timing of spikes on a millisecond scale was critical. However, the noisy responses of neurons to repeated stimuli was taken by some to suggest that only a rate code was theoretically possible (Shadlen and Newsome, 1994). A year later, Mainen and Sejnowski (1995) elegantly showed that while cortical neurons respond with high variability to a constant depolarizing input, they can respond with millisecond precision to a noisy input, suggesting that information can indeed be carried in the precise timing of spikes. Oscillations are an efficient mechanism to achieve this precision in spike timing (Gray et al., 1989; Gray and Singer, 1989; Engel et al., 1999; Buzsaki and Draguhn, 2004). Through synchronization of membrane potential oscillations at particular frequencies, narrow time windows are created in which action potentials can be elicited in each cell. This potentially allows cell assemblies to coordinate their output to downstream neurons.

The first oscillation described in the human EEG was the alpha oscillation (Berger, 1929). This large amplitude signal, with a frequency of around 10 Hz, was recorded over the occipital cortex when the subject (Berger’s son) closed his eyes. Upon opening his eyes, the alpha rhythm disappeared and in its place Berger saw what he called beta oscillations, which were faster (13-30 Hz) but much lower amplitude. This highlights an important characteristic in neural oscillations: that amplitude is inversely related to frequency (Pritchard, 1992). Larger amplitude oscillations imply synchronization (and therefore summation) across larger populations of neurons. At the low(er) end of the frequency spectrum, the ~1 Hz slow oscillation, which occurs during nonREM sleep in the neocortex, involves the synchronization of all cortical cells in a coordinated rhythmic alternation between activity and silence. The slow oscillation will be discussed in more detail in sections 1.3 and 1.4. At the high(er) end, gamma (20-100 Hz) oscillations are synchronized much more locally, although long-range gamma synchronization can occur and is one mechanism for linking distributed cell assemblies.

1.2 Gamma oscillations for precision and synchrony

In the context of the millisecond precision of spike timing alluded to at the beginning of this section, gamma oscillations, with a period length of 10-50ms, seem optimally suited to shape neural output at the relevant time scales. Gray et al. (1989) showed that synchronization of gamma oscillations is important for our visual perception of object properties. They recorded from the primary visual cortex of anaesthetized cats, and showed that bars of light crossing the visual fields of two separate cells elicited synchronization at gamma frequency only if the bars were connected, but not if they were two separate bars. Importantly, the differences between the stimuli (i.e. connected or not connected) were outside the visual fields of either cell. Thus, gamma oscillations appear to synchronize across cells responding to the same, but not different objects. Gamma oscillations have therefore been suggested to play a role in perceptual binding, allowing us to see objects as distinct from other objects and from the background (Tallon-Baudry and Bertrand, 1999).

In another modality, Stopfer et al. (1997) showed that gamma oscillations are important for the discrimination between similar stimuli. They disrupted gamma oscillations in honey bees trained on an odour discrimination task using the $GABA_A$ antagonist picrotoxin. Notably, this did not disrupt the slow dynamics of the responses to various odours in the antennal lobe neurons, but only the 30 Hz gamma oscillations. Without gamma, bees could no longer discriminate between similar odours, although they could still respond correctly to dissimilar odours.

That antagonism of receptors for GABA, the brain's most ubiquitous inhibitory neurotransmitter, would disrupt gamma oscillations specifically highlights the role of inhibition in shaping and synchronizing this rhythm. Indeed gamma oscillations are thought to be generated by feedback inhibition from inhibitory interneurons onto principal cells (Buzsaki and Wang, 2012). Optogenetic stimulation of parvalbumin-positive fast-spiking interneurons over a range of frequencies in the rat barrel cortex increased power at the corresponding frequency in the local field potential only for stimulation in the gamma range (20-80 Hz), but not for other frequencies (Cardin et al., 2009). By contrast, optogenetic stimulation of excitatory principal cells only increased LFP power for lower (8-24 Hz) frequencies, showing differential roles for interneurons and principal cells in shaping oscillatory synchrony at various frequencies. Indeed, a recent review suggests that bottom-up, or stimulus driven processes may operate in the gamma range, while top-down processes such as attention may operate at lower frequencies (Fries, 2015).

The waxing and waning inhibition created by the feedback mechanism from inhibitory interneurons onto principal cells also creates a situation in which the principal cell receiving the greatest excitation on a given cycle will fire first, leading to inhibition of less excited cells before they reach their threshold for firing. This winner-takes-all mechanism has been suggested to increase the signal to noise ratio in the nervous system (Fries et al., 2007). A further consequence of the influence of gamma phase on principal cell firing is that inputs arriving at downstream neurons will be gamma-modulated. The precise timing of these inputs relative to those from other areas as well as the local gamma rhythm will influence the response of the target cell, as the cycle starts again.

1.3 Rhythms of sleep

In a series of papers in 1993, Steriade and colleagues described a novel slow (<1 Hz) rhythm appearing in natural sleep and anaesthesia. This slow oscillation (SO) consists of alternating periods of activity (ON/UP phase) and silence (OFF/DOWN phase) of neocortical neurons (Steriade et al., 1993d; Steriade et al., 1993b, c; Steriade, 2001). The SO is unique among brain rhythms, in that the OFF periods are not associated with active inhibition (as with the gamma oscillation described above), but simply membrane potential hyperpolarization and neural silence. Although individual cycles of the SO appear to have local origins, and to propagate across the cortex in travelling wave (Massimini et al., 2004), large-scale synchrony across cortical neurons produces a large amplitude rhythm clearly visible in the EEG. Faster rhythms, such as thalamocortical spindle oscillations (8-16 Hz) as well as local gamma activity, are grouped into the ON phase of the SO.

In the history of sleep research, ground-breaking discoveries have stemmed from observations that other researchers had ignored or explained away when they didn’t fit with the dominant theories of the time. The discovery of rapid-eye-movement (REM) sleep (Aserinsky and Kleitman, 1953) occurred 18 years after the characteristics of the human EEG during sleep were first described (Loomis et al., 1935b, a). William Dement, working in the Kleitman lab, described the cyclical nature of REM-nonREM alternations within the sleep cycle in humans (Dement and Kleitman, 1957) as well as the completely activated (wake-like, low-voltage fast activity) EEG associated with REM sleep in cats (Dement, 1958). In a historical account, Dement recalls the extremely controversial nature of his findings at the time (his 1958 paper was rejected 4 or 5 times), and also points out that other groups had seen these activated states during sleep but ignored them as periodic awakenings (Dement, 1990). Likewise, when Steriade first introduced the slow oscillation, he commented: '*with the benefit of hindsight, these aspects may also be seen in previous recordings of humans and experimental animals'* (Steriade et al., 1993b). Thus, the history of sleep research tells us to pay attention to observations that don't fit with our expectations.

1.3.1 Sleep and memory

The relationship between sleep and memory has a long history. In 1885 when Hermann Ebbinghaus described his classic forgetting curve in recalling long lists of nonsense syllables, he observed a slower rate of forgetting when the retention interval included sleep (original citation: Ebbinghaus, 1885; reviewed in: Rasch and Born, 2013). Jenkins and Dallenbach (1924) later found improved memory retention for lists of nonsense syllables when sleep instead of wakefulness followed learning, and they attributed this to the effect of reduced interference during sleep. However, when the amount of sleep and wake (and therefore the amount of interference) was controlled for, it was found that the timing of sleep relative to learning is critical, suggesting an important window immediately following learning when memory can be enhanced by sleep (Benson and Feinberg, 1977). This study and others (reviewed in Rasch and Born, 2013), suggested that sleep in a critical window can protect memory against the effects of future interference. Thus, an active process, often called memory *consolidation*, might be occurring during sleep.

Attempts to separate the differential effects of REM and nonREM sleep on memory were initially challenging. For example, a paradigm used in rodent studies to selectively deprive animals of REM sleep is called the flower pot or pedestal method. Animals sleep on a small platform surrounded by water. Due to the complete muscle atonia associated with REM sleep, as soon as they enter this stage they fall into the water and wake up. This paradigm is clearly confounded by stress (Vertes and Eastman, 2000). Using a different approach, some researchers took advantage of the fact that nonREM sleep occurs preferentially early in the night, while REM sleep is more prevalent later (Yaroush et al., 1971; Fowler et al., 1973). Plihal and Born (1997) found a double dissociation between early (nonREM-rich) vs late (REM-rich) sleep, where nonREM (early night) sleep enhanced memory for paired associate lists (declarative memory) but not for mirror tracing (procedural memory), whereas REM (late night) sleep had the opposite effect. Correlational evidence also pointed to a relationship between specific sleep stages and memory. Spindle oscillations (8-16 Hz), which occur during nonREM sleep, were correlated with performance on a verbal memory task (Clemens et al., 2005), and were selectively increased after human subjects explored a virtual maze (Meier-Koll et al., 1999) and in rats after an odour-reward association task (Eschenko et al., 2006).

1.3.2 The slow oscillation and memory

More recent work has pointed to a direct role of Steriade’s slow oscillation in enhancing declarative memories. Incredibly, trans-cranial electrical stimulation at SO frequency during nonREM sleep enhanced performance on a paired associate memory task, but not on a procedural finger-tapping task compared to a sham stimulation condition (Marshall et al., 2006). In contrast, stimulation at faster (5 Hz) frequencies did not improve memory performance. This finding in humans was replicated by the same group in rats, using an object-place recognition task (Binder et al., 2014b), although the effects using a radial arm maze task were harder to interpret (Binder et al., 2014a), with the stimulation-induced improvements seen primarily in working memory and not necessarily long-term memory. Again from the same group, Ngo et al. (2013) found that auditory stimulation that was in phase with the subject's endogenous slow oscillation (using a closed-loop feedback system) enhanced SO power and, in parallel, enhanced performance on a declarative memory task. By contrast, stimulation that was out of phase with the SO did not have an effect.

Chauvette et al. (2012) proposed a potential mechanism for the enhancing effects of nonREM sleep on memory. First, they showed that evoked potentials in the somatosensory cortex of head-restrained cats were increased during wake that followed nonREM sleep but not following REM sleep. To assess the mechanism of this increase, they recorded the time courses of both single unit activity during nonREM sleep, as well as the membrane potentials marking the ON and OFF state transitions. Using these experimentally derived parameters, they showed that the combination of nonREM sleep-like spiking activity AND the ON/OFF state membrane potential fluctuations induced a longer-lasting potentiation of evoked potentials compared to the spike trains alone. Therefore it appears that the hyperpolarization phase and associated neural silence during the SO might be critical for mediating the declarative memory-enhancing effects of nonREM sleep.

1.4 Role of the hippocampus in memory and sleep

The above discussion ignores an important point – the memories that seem to be enhanced during nonREM sleep are those memories that rely on activity of that unique structure deep in the temporal lobe known as the hippocampus. Much of our understanding of the role of the hippocampus in memory stems from what might be considered an unfortunate mistake. On September 1, 1953, Henry Molaison, known by many until his death in 2008 simply by his initials H.M., underwent experimental surgery to bilaterally remove his medial temporal lobes as a last-resort treatment for intractable epilepsy (Scoville and Milner, 1957). Although the surgery reduced the severity of his seizures, the deleterious effect on his memory was dramatic and profound. When examined 19 months after his surgery by Brenda Milner in April 1955, Molaison reported that the date was March 1953 (Scoville and Milner, 1957). In a striking dissociation, his IQ was 8 points *higher* than measured prior to the operation, despite a complete loss of memory for events after his surgery. Other aspects of Molaison's deficits included an impairment in spatial memory, a finding that preceded the discovery of the place cells in the hippocampus and the structure's role as a cognitive map (O'Keefe and Dostrovsky, 1971). Importantly, he still retained memories for events preceding the surgery, although there was a retrograde pattern such that his memory was better for more distant events than for recent ones. This suggested that the hippocampus was only involved in memory acquisition and storage of recent memories, but that older memories might reside somewhere else in the brain.

The other significant finding that came from studying the effects of temporal lobectomy was the existence in the brain of multiple memory systems for different types of information. First, while Molaison could hold items in memory through verbal rehearsal, in a visual task in which rehearsal was not possible his memory decayed after ~30 seconds (Sidman et al., 1968). Thus, a distinction was made between the role of the hippocampus in working or short-term memory and longer-term memories (Milner, 2005). A further distinction was discovered with Molaison's performance on a procedural memory task (Corkin, 1968). This involved the mirror tracing task, where the subject must trace the outline of a star using only its mirrored reflection. Molaison's performance matched the normal learning curve over a 30 day period, despite his having absolutely no recollection of any of the practice sessions. Milner recollected many years later that '*we are now used to the idea that such dissociations are possible after a circumscribed brain lesion, but witnessing this for the first time was an astonishing experience'* (Milner, 2005). Thus, with the help of Milner and Molaison and others, a picture emerged of the hippocampus as a structure important for the acquisition of spatial and declarative, but not procedural memory or short-term memory, that has continued to guide research to this day (Eichenbaum, 2013).

1.4.1 Hippocampal neuroanatomy

If the hippocampus is so critical for declarative memory processes, an examination of its structure and connections might give us some clues as to the nature of memories and how they are stored. The striking appearance of the hippocampus as a distinct structure in the brain has inspired neuroanatomists across the centuries to describe it in terms of visual analogies. So the hippocampus was originally given its name from the Greek word for sea horse (original citation Arantius, 1587; as cited in Schultz and Engelhardt, 2014). Later, an analogy was made with a ram's horn, leading to the naming of the hippocampus as Ammon's horn after the Egyptian god Ammon, who was sometimes depicted with a ram's head or as a ram. This led Lorente de Nó to use the name Cornu Ammonis, from which the name for the well-known CA subfields of the hippocampus are derived (original citations Winslow, 1732; Croissant de Garengeot, 1742; Lorente de No, 1934; as cited in Schultz and Engelhardt, 2014). Once the hippocampus is sliced transversely across its long axis, it is no less impressive, although the more contemporary analogy of a jelly roll to describe the interlocking "C" appearance of hippocampal slices is perhaps less romantic than the image of the horn of an Egyptian god.

At the beginning of the 20th century, When Santiago Ramon y Cajal created his beautiful drawings of Golgi (silver nitrate)-stained hippocampal slices, he drew arrows suggesting the primarily unidirectional flow of information through the hippocampal circuit, and his ideas have largely proven correct (Andersen et al., 2007). Unlike the 6-layered neocortex, the hippocampus retains the more ancient three-layered architecture, and is therefore labelled archicortex. The following description will focus on the rat neuroanatomy, but the structure and circuitry of the hippocampus are remarkably conserved across species although they are not identical (Andersen et al., 2007). The long axis of the hippocampus is called the septo-temporal axis (Figure 1.1), although the septal portion is also referred to as the dorsal hippocampus, and the temporal pole as the ventral hippocampus. The transverse plane is perpendicular to the septo-temporal axis. Many figures in this thesis use the idealized diagram of a transverse section from the dorsal (septal) hippocampus (Figure 1.2). In the human brain, the position of the hippocampus is shifted due to the massive development of the frontal cortical areas, so that the equivalent of the temporal (ventral) hippocampus is anterior (rostral) in the human, while the equivalent of the septal (dorsal) hippocampus is posterior (caudal).

Before delving into the hippocampal circuitry itself, it is important to keep in mind the type of information it receives. The pattern of hippocampal connections with the neocortex make it clear that it holds a unique position in the chain of

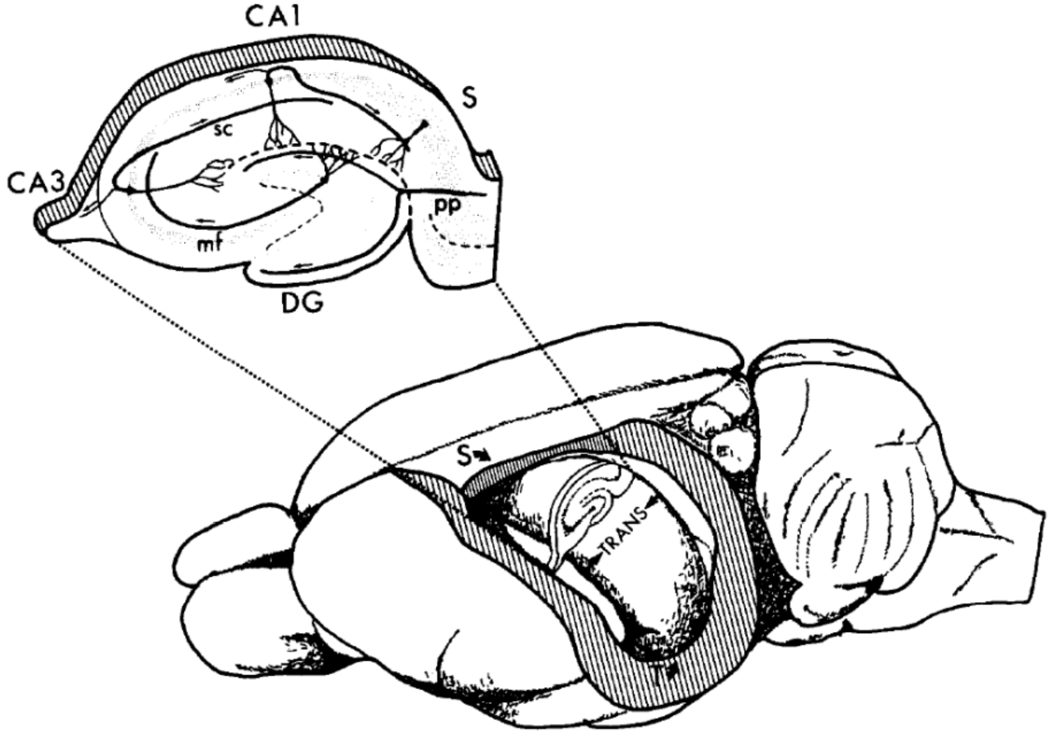

Figure 1.1 Position of the hippocampus in the rat brain

This drawing of a rat brain with the cortex overlying the hippocampus removed depicts the position of the septal (S) and temporal (T) poles. A transverse slice perpendicular to the long (septo-temporal) axis is enlarged, depicting the major hippocampal subfields as well as the major fiber pathways of the trisynaptic loop (pp: perforant pathway; DG: dentate gyrus; mf: mossy fiber pathway; sc: Schaffer collateral pathway; S: subiculum) as well as the direction of information flow (arrows). Reprinted from: Neuroscience, vol. 31(3), Amaral DG and Witter MP, The three-dimensional organization of the hippocampal formation: A review of anatomical data, pp. 571-591, 1989, with permission from Elsevier.

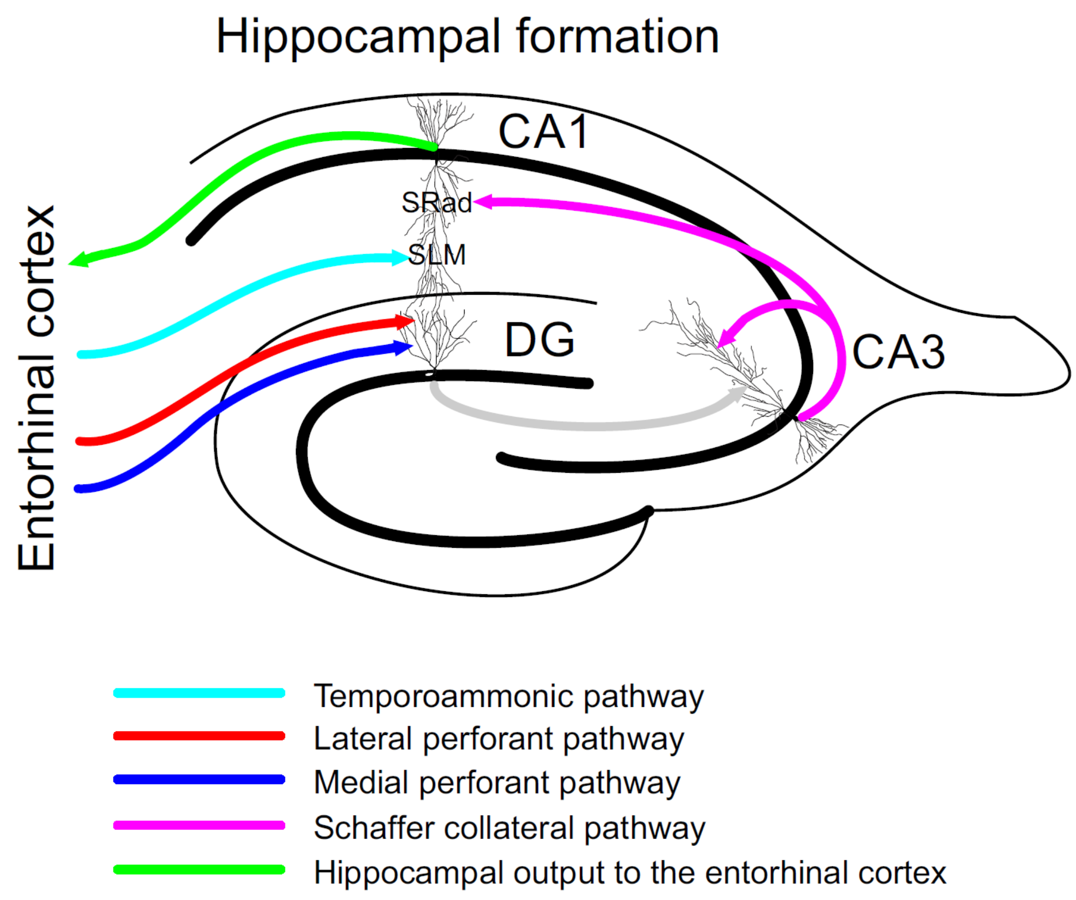

Figure 1.2 Schematic representation of dorsal hippocampus

This diagram, repeated throughout the thesis, depicts the laminar organization of the major projections from the entorhinal cortex to the hippocampus. Note that this Figure and Figure 1.1 depict the left and right hippocampi respectively and are therefore flipped horizontally. The medial and lateral perforant pathways (blue and red) project to the middle and outer thirds of the molecular layer of the dentate gyrus (DG). The temporoammonic pathway (cyan) projects directly to SLM in CA1. The Schaffer collateral pathway (magenta) projects to SRad in CA1. The pyramidal cell layer in CA1 projects back to the entorhinal cortex (green).

information processing in the brain. Highly processed information from primary sensory and multimodal association areas of the neocortex projects first to the perirhinal and pararhippocampal cortices before arriving at the entorhinal cortex, although some other cortical inputs do project directly to the entorhinal cortex (Lavenex and Amaral, 2000). It has been suggested that the rhinal cortices might serve an inhibitory gating function between the neocortex and the hippocampus (de Curtis and Pare, 2004). The entorhinal cortex is 6-layered, with two acellular layers: layer I and layer IV (also known as lamina dessicans), and four cellular layers. The superficial layers (II and III) project to the hippocampus, while the deep layers receive the processed information from the hippocampus, either directly or through the subiculum, and relay it back to the rest of the neocortex.

From the entorhinal cortex, the primarily uni-directional circuit of the hippocampus suggested by Cajal (the so-called tri-synaptic loop) begins. Stellate and pyramidal cells in entorhinal layer II give rise to the perforant pathway, travelling in the angular bundle before ‘perforating’ the subiculum to synapse on dentate granule cell dendrites in the molecular layer of the dentate gyrus. More specifically though, the lateral entorhinal cortex projects to the outer third of the molecular layer (lateral perforant path; LPP), while the medial entorhinal cortex projects to the middle third (medial perforant path; MPP). This is significant because medial and lateral entorhinal cortices are thought to integrate different types of information from different primary sensory areas: spatial information in the medial and non-spatial information in the lateral (Manns and Eichenbaum, 2006). Therefore, spatial and non-spatial information might be integrated at this point.

From the first stop in the relay, the dentate granule cells give rise to the mossy fibers that project to CA3, with many mossy fibers terminating in stratum lucidum, a layer only seen in CA3. Among several unique features of this projection, including very large synapses with many active zones, as well as a presynaptic form of potentiation (Andersen et al., 2007), it is the only point of the trisynaptic loop that confines its projections primarily to the same septo-temporal level as its cell bodies (Amaral and Witter, 1989). This in addition to the fact that a single dentate granule cell only projects to ~15 CA3 pyramidal cells, while a single CA3 pyramid likely receives input from ~70 dentate granule cells (Andersen et al., 2007), suggests a high degree of convergence of information at this point in the loop. From this point, CA3 pyramidal cells form a large associational projection to stratum radiatum (SRad) of other CA3 pyramidal cells, in addition to the Schaffer collateral (SchC) projection to SRad of CA1 (both ipsilateral and contralateral through the hippocampal commissure). The pyramidal cells of CA1 then complete the trisynaptic loop by projecting to the deep layers of the entorhinal cortex (either directly or through the subiculum).

In addition to this trisynaptic loop and the associational connections in CA3, there is a direct projection from layer III of the entorhinal cortex to the distal dendrites (stratum lacunosum moleculare, SLM) of CA1. This projection, known as the temporoammonic pathway, also travels in the angular bundle with the perforant path fibers, but instead of perforating the subiculum it travels in the alveus. An interesting facet of the temporoammonic projection is that the medial entorhinal cortex projects to proximal CA1 (closer to CA3) while the lateral entorhinal cortex projects to distal CA3 (closer to the subiculum). This is distinct from the perforant path projection, in which medial and lateral entorhinal cortex projections are segregated into the middle and outer thirds of the molecular layer at all proximo-distal points. The computational consequence of this arrangement is that medial and lateral entorhinal inputs, carrying different types of information, might be integrated in the dentate gyrus but remain segregated in CA1.

SLM and layers I and III of the entorhinal cortex also receive a subcortical projection from the nucleus reuniens (NRe) of the thalamus (Wouterlood et al., 1990; Dolleman-Van der Weel et al., 1997; Dolleman-Van der Weel and Witter, 2000). In addition, the medial septum sends GABAergic and cholinergic projections to multiple hippocampal layers (Pignatelli et al., 2012), and this projection is critical for the expression of the hippocampal theta rhythm which will be discussed below (Winson, 1978; Bland et al., 1996). Finally, brainstem inputs from the median raphe and hypothalamic inputs from the supramamillary nucleus also influence hippocampal function (Vertes and McKenna, 2000; McKenna and Vertes, 2001). A diverse network of interneurons targeting distinct cellular compartments in each of the hippocampal subfields also modulate the dendritic and somatic responses and oscillatory dynamics of hippocampal principal cells (Freund and Buzsaki, 1996; Klausberger, 2009; Lasztoczi and Klausberger, 2014).

An interesting aspect of hippocampal organization is that all of the major pathways described above reside in a 2-dimensional transverse plane perpendicular to the septo-temporal axis of the hippocampus (Figure 1.1). This led to the lamellar hypothesis that the hippocampus consists of parallel laminae that can operate as separate functional units (Andersen et al., 1971). Although anatomical investigations have since shown that connections are highly divergent in the septo-temporal axis at every stage of the trisynaptic loop except for the mossy fiber pathway (Amaral and Witter, 1989), the functional consequence of this divergence from a strict lamellar arrangement has not been elucidated (Sloviter and Lomo, 2012). The computational capacity of the hippocampus, with the combination of divergent and convergent connections, is clearly immense, and hopefully the combination of experimental and computational approaches in the future will elucidate more about how memories are acquired within its circuits.

1.4.2 Hippocampal oscillations

The circuitry of the hippocampus supports several oscillatory patterns that are somewhat unique to this structure. The theta rhythm (3-12 Hz) in rodents is one of the most thoroughly studied oscillations in neuroscience, and its striking appearance and strong rhythmicity have hypnotized many a graduate student (see Figure 1.3B). Its complex generation involves interactions with the entorhinal cortex as well as cholinergic, GABA-ergic and possibly glutamatergic inputs from the medial septum (Bland, 1986; Buzsaki, 2002; Pignatelli et al., 2012), although CA1 can generate theta independently as well (Goutagny et al., 2009). Theta oscillations are strongly associated with the behavioural states of active exploration and REM sleep, although the generation of theta under these two states is subtly different, such that REM-associated theta is abolished by the muscarinic antagonist atropine, but movement/exploration-associated theta is not (Vanderwolf, 1969; Whishaw and Vanderwolf, 1973; Kramis et al., 1975).

Strong gamma frequency oscillations are seen in the hippocampus during theta activity (Bragin et al., 1995). Gamma coherence between different subfields can change as a function of behavioural state (Montgomery et al., 2008), and distinct frequencies within the gamma band (fast vs slow gamma) in CA1 have been associated with the different synaptic inputs and different theta phases (Colgin et al., 2009). Although this latter finding is controversial (see Schomburg et al., 2014, especially supplementary material), other groups have also shown that localized gamma oscillations in the CA1 dendritic compartments reflect synaptic inputs from upstream regions (Lasztoczi and Klausberger, 2014; Schomburg et al., 2014).

In general, the amplitude of gamma oscillations is modulated by the phase of the theta rhythm. This type of cross-frequency coupling has been studied more and more in recent years (Canolty and Knight, 2010; Tort et al., 2010; Hyafil et al., 2015), and has potential implications for understanding the neural code (Lisman and Buzsaki, 2008; Lisman and Jensen, 2013). The attempt to 'decode' neural activity has been particularly fruitful in the hippocampus because the firing of pyramidal cells in CA1 is strongly correlated with an animal's position in its environment (O'Keefe and Dostrovsky, 1971). As an animal runs on a linear track, each place cell in a sequence marking the animal's trajectory fires on successive gamma cycles within the theta oscillation (Dragoi and Buzsaki, 2006). Tantalizingly, with respect to the role of sleep and memory, these sequences have been shown to replay in the hippocampus during subsequent nonREM sleep, suggesting a possible mechanism by which sleep can strengthen memory (Wilson and McNaughton, 1994; Skaggs and McNaughton, 1996; Nadasdy et al., 1999; Buhry et al., 2011).

This has brought us back to the story of nonREM sleep and declarative memory consolidation, now with a better appreciation for how the hippocampus might participate. During the deep stages of nonREM sleep, while neocortical cells are exhibiting the rhythmic alternations between activity and silence that characterize the SO, the hippocampus was long thought to exhibit a non-rhythmic state called large-amplitude irregular activity, or LIA (Whishaw and Vanderwolf, 1973). However, some coordination of hippocampal activity with the SO was apparent (Sirota et al., 2003; Sirota and Buzsaki, 2005; Isomura et al., 2006), and Wolansky et al. (2006) demonstrated that the hippocampus does exhibit a ~1 Hz rhythm (the hippocampal SO) that is distinct from, but coordinated with, the SO in the neocortex. Just as gamma oscillations during theta are modulated by theta phase, gamma oscillations during the hippocampal SO are modulated by SO phase (Wolansky et al., 2006), confirming that local networks are involved. Gamma-modulated synaptic inputs are likely underlying the coordination of hippocampal activity with the neocortex during nonREM sleep, but this has received much less attention than the gamma-theta interactions described above. Understanding these dynamics is a primary focus of this thesis, and the work I have done will be presented in Chapter 3.

Aside from gamma, a striking activity pattern co-occurs with slow oscillations in the hippocampus during nonREM sleep: the hippocampal sharp wave-ripple (SPW-R; Buzsaki et al., 1983; Csicsvari et al., 2000; Sullivan et al., 2011). This brief (~100 ms) event involves a massive and synchronous synaptic input from the CA3 through the Schaffer collaterals to SRad of CA1. This produces a large negative-going wave in the LFP (sharp wave), and triggers a high-frequency (100-200 Hz) oscillation in the CA1 pyramidal cell layer (ripple). It is during these ripples that the reactivation or replay of place cell sequences described above are observed (Lee and Wilson, 2002; O'Neill et al., 2008; O'Neill et al., 2010). Furthermore, direct online disruption (by electrical stimulation) of ripple events impairs memory (Girardeau et al., 2009; Ego-Stengel and Wilson, 2010). These ripple events at the pyramidal cell layer modulate pyramidal cell output back to the cortex, thereby potentially reactivating the neocortical cell assemblies important for a particular memory.

1.5 Probing hippocampal activity during sleep-like states

My thesis work was motivated by the evidence presented above that the slow oscillation is critical for sleep-dependent consolidation of hippocampal-dependent memories, and the assumption that this must require bidirectional communication between neocortical and hippocampal circuits. My main goal was therefore to understand the coordination of hippocampal input and output pathways and the associated gamma and SPW-R activity patterns with the neocortex during the SO, and to compare this coordination to that seen during theta oscillations.

1.5.1 Sleep-like activity under urethane anaesthesia

To approach this question, I used the urethane model for sleep, which recapitulates most of the network activity patterns seen during natural sleep in a much more controlled environment (Figure 1.3; Wolansky et al., 2006; Clement et al., 2008). In fact, Steriade first described the intracellular dynamics of the SO using urethane (as well as other anaesthetics), which were later confirmed in naturally sleeping animals (Steriade et al., 1993b; Steriade et al., 2001). All of the major oscillatory activity patterns described above have been found in urethane anaesthetized animals (Ylinen et al., 1995b; Isomura et al., 2006; Lasztoczi and Klausberger, 2014), although the frequency of the theta rhythm is reduced along with subtle changes in its spatial profile (Kramis et al., 1975; Ylinen et al., 1995a), and ripples might also occur at a lower frequency (Ylinen et al., 1995b). Urethane is thought to act by potentiation of a potassium leak channel, thereby hyperpolarizing cells with minimal disruption of signal transmission (Sceniak and MacIver, 2006). Animals anaesthetized with urethane cycle rhythmically between an activated state characterized by hippocampal theta oscillations and a deactivated state characterized by the slow oscillation in the neocortex and hippocampus. This was an ideal model to examine the coordination of activity during both states.

1.5.2 Recording local field potentials

Using the urethane model, we recorded the electrical activity across multiple layers of the hippocampus (or in some cases the entorhinal cortex) during both theta and the SO. At any given point within the brain, an electrical potential can be measured (with respect to a reference point) which represents the summed contributions of all electric currents in the brain (Buzsaki et al., 2012). This is known as the local field potential (LFP). Historically, the largest contributor to the LFP was

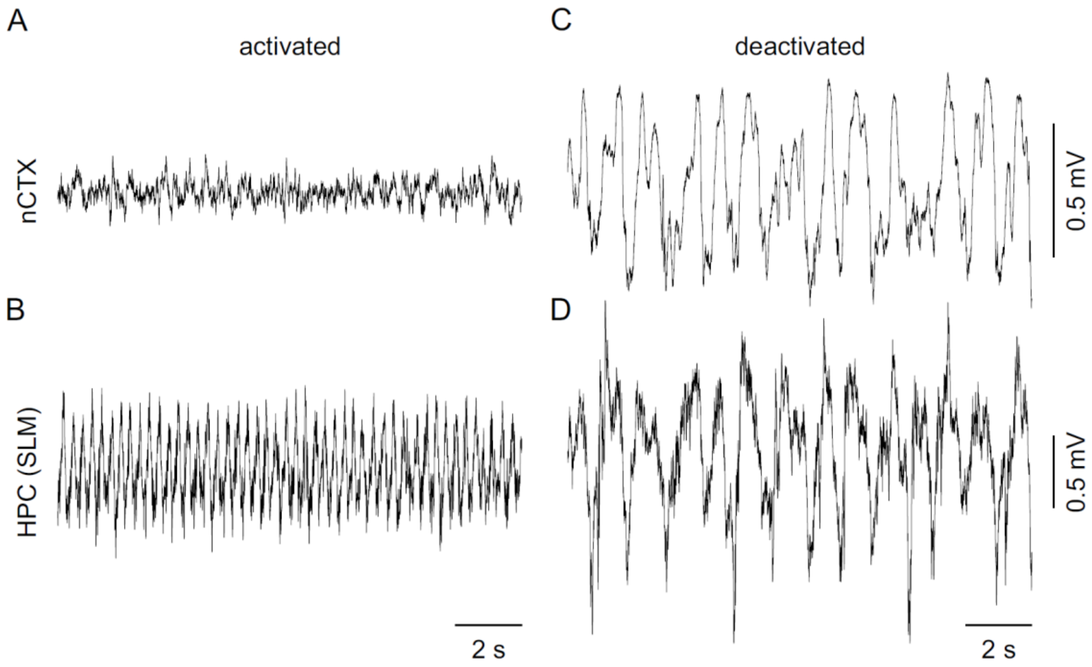

Figure 1.3 Oscillatory activity patterns recorded under urethane anaesthesia

Activity patterns recorded from urethane anaesthetized rats during the activated (REM-like) and deactivated (nonREM-like) states. (A) Low voltage fast activity in the neocortex (nCTX) during the activated state. (B) Theta (3-12 Hz) activity recorded from the hippocampus (SLM) during the activated state. (C) The ~1 Hz SO recorded from the neocortex during the deactivated state. (D) The ~1 Hz hippocampal SO recorded from SLM during the deactivated state.

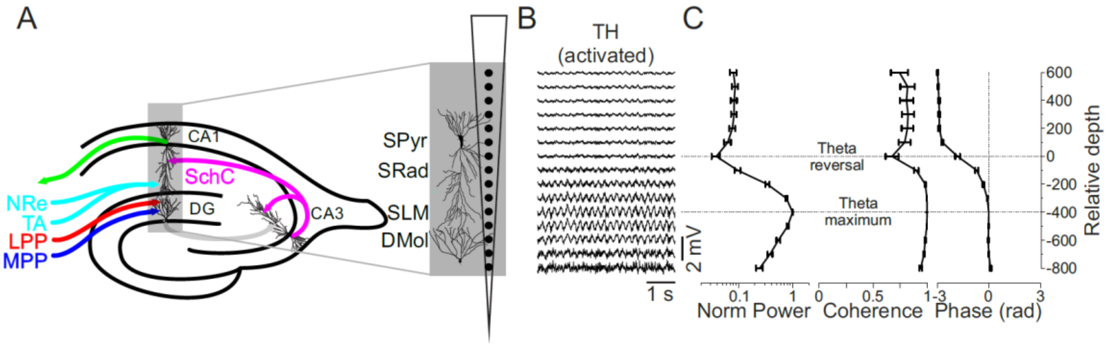

Figure 1.4 Profile of theta activity relative to hippocampal laminae

(A) Schematic representation of recording sites in the dorsal hippocampus using a linear array (DMol: dentate molecular layer; SLM: stratum lacunosum moleculare; SRad: stratum radiatum; SPyr: stratum pyramidale). (B) Short epoch of theta activity recorded with a linear array in the dorsal hippocampus with 100 µm contact separation. (C) Power, coherence and phase profiles of theta activity as a function of depth. Notice clear drop in coherence and reversal of phase. Depth measures are relative to this phase reversal. Note also clear peak in theta power at -400 µm. Profiles are averages across 16 animals, aligned to theta reversal and theta maximum.

assumed to be synaptic potentials, because their slow dynamics compared to action potentials result in greater summation at any given time (Mitzdorf, 1985), although recently the potential for spiking activity to influence the LFP signal at higher frequencies has been revealed (Scheffer-Teixeira et al., 2013; Waldert et al., 2013). At the level of individual cells, when a neuron is depolarized, due to the influx of positive ions, current is essentially leaving the extracellular space, creating a current sink. That sink must be balanced by a return current, creating a nearby passive source. The sink/source pair creates a dipole. A single electrode located near the sink in the extracellular space will register a negative voltage deflection, while an electrode near the source will register a positive deflection. This means that if the depolarization of the cell is happening rhythmically, the oscillations recorded near the sink and near the source will be 180° out of phase with each other.

The disadvantage of LFP recordings, that they sum activity over large areas, is also its advantage. In order for strong signals to be recorded, large populations of cells must be coordinated. By its nature, the LFP is a measure of neural synchrony. Some improvement can be attained in the ability to localize signals recorded by the LFP by using multi-site electrodes. As alluded to above, the phase of activity located near the sink and the source are reversed with respect to each other. Therefore, by sampling at enough points, the locations of these phase reversals can be identified. Indeed, the typical spatial profile of the theta oscillation in the hippocampus under urethane anaesthesia is so stereotyped that it can be used to assess the location of the multiprobe with respect to the major cell layers based on purely electrophysiological measures (Figure 1.4). Specifically, the maximum theta power occurs at SLM, and a drop in coherence accompanied by a 180° reversal of phase occurs just below the pyramidal cell layer. The distance between these two points is typically 400 μm in the rat brain.

A method to actually localize sinks and sources is current source density (CSD; Freeman and Nicholson, 1975; Mitzdorf, 1985; Rodriguez and Haberly, 1989). Briefly, if the *first* spatial derivative (the change in voltage as a function of distance) is proportional to the current flow between points in the extracellular space (V=IR), then the *second* spatial derivative is proportional to the change in current flow at those two points, which localizes where current is entering and leaving the extracellular space. Therefore, if the active sink is located outside of the recording area, the signal recorded at each electrode will be monotonically decreasing as a function of distance from the sink, but the second spatial derivative will be zero since the rate of change of voltage by distance is the same. One caveat of CSD analysis is that it cannot differentiate between active and passive sinks. Therefore a sink at one location could be due to active depolarization at that point, or to a passive return current to the site of active hyperpolarization at another point. The signal is therefore still mixed, with active and passive sinks and sources overlapping.

A relatively novel approach, Independent Component Analysis (ICA), can be used to unmix the LFP into its underlying sources of activity (Makarov et al., 2010). This approach forms the basis for much of my thesis, and will be described in detail in Chapter 2. Briefly, ICA estimates the underlying sources contributing to a mixed signal such as the LFP by assuming that the sources are statistically independent over time (Hyvarinen, 1999b).

1.5.3 The dynamics of hippocampal input and output pathways during the SO and theta – summary of findings

In Chapter 2, I describe the implementation of the ICA method to separate the mixed local field potential in the dorsal hippocampus into underlying sources. Some important pre-processing steps that were found to greatly improve the reliability of ICA components across epochs within the same animal are discussed. Using ICA, reliable sources were extracted across animals, and I present evidence that these sources represent the separated contributions of the distinct hippocampal afferent pathways. The success of ICA in removing the volume-conducted portion of the LFP will be demonstrated as one potentially valuable application of this approach. Finally, a modification to the Better Oscillation detection (BOSC) method (Caplan et al., 2001; Whitten et al., 2011; Hughes et al., 2012) is presented and applied to ICA-separated components to detect gamma oscillations and SPW-Rs.

Chapter 3 describes our work using the above methods to examine the coordination of activity in hippocampal input and output pathways during SO and theta oscillations. First, we found that gamma oscillations in input pathways are segregated based on the phase of the SO during both states. Secondly, we discovered that the input arriving at SLM is characterized by occasional ‘failures’ or skipping of cycles with respect to the neocortical SO. Finally, we demonstrated that the phase of SPW-R events is related to the power of the neocortical SO, with SPW-Rs preceding the neocortical UP state when SO power is low, but following the neocortical UP state when SO power is high.

In Chapter 4, I describe two previously unreported effects of medial septal inactivation on hippocampal activity. First, the unmasking of a ~0.1-0.5 Hz rhythm during the activated state. Upon closer examination, this slow rhythm, which we call iota, was found to be present during spontaneous theta oscillations as well. Iota appears to also have correlates during the deactivated state, possibly manifested as the cycle skipping found in Chapter 2. The second main finding was a dramatic reduction in activity of the SLM-targetting input during the hippocampal SO following septal inactivation with lidocaine, but not with muscimol. This implicates either the nucleus reuniens or other subcortical afferents in the coordination of the hippocampal SO with the neocortex.

Taken together, these findings paint a dynamic picture of the coordination of hippocampal input and output circuits with the neocortical SO. Chapter 5 will present a summary and integration of the above findings, and discuss important avenues for future research.

2 Independent component analysis for identifying underlying sources of activity in the dorsal hippocampus: Evaluation and useful applications

Authors: Tara A. Whitten[1], and Clayton T. Dickson[1,2,3]

[1]Neuroscience and Mental Health Institute, University of Alberta, Edmonton, AB, Canada, T6G 2E1

[2]Department of Psychology, University of Alberta, Edmonton, AB, Canada, T6G 2H7

[3]Department of Physiology, University of Alberta, Edmonton, AB, Canada, T6G 2E9

Acknowledgments: This work was supported by a Natural Science and Engineering Council of Canada (NSERC) grant # 249861 to CTD. TAW was additionally supported by an Izaak Walton Killam Memorial Graduate Scholarship, an Alberta Innovates – Technology Futures Graduate Scholarship and an NSERC Alexander Graham Bell Canada Graduate Scholarship – Doctoral (CGS D). We would like to acknowledge Trish Wolansky and Jon Kerber for contributing to data collection and an unidentified reviewer of another manuscript (chapter 3) for making helpful suggestions about ICA implementation.

2.1 Abstract

Hippocampal circuits are implicated in episodic memory and spatial navigation processes. Understanding the dynamics of input-output elements in the hippocampus is an important step to decode its processing characteristics. Independent component analysis (ICA) is one approach that has been used to estimate the underlying elements contributing to the mixed signal recorded from multisite electrodes in the dorsal hippocampus. These underlying elements are likely to represent the activity in distinct afferent pathways. Here, we compared and evaluated the results from several ICA algorithms based on their ability to extract a volume-conducted signal, as well as the biological plausibility of the spatial weighting profiles of the extracted components. We then evaluated the robustness of one ICA algorithm to non-stationarities in the signal by assessing how the components change across different epochs. We found that the robustness was vastly improved by pre-filtering to remove slow (<6 Hz) frequencies in the signal prior to ICA implementation. The consistency of ICA results across animals was then assessed, and 5 components were putatively identified as either the volume conducted signal or as one of 4 major afferent pathways to the dorsal hippocampus. Finally, we demonstrated two potential applications of the ICA approach: first, extracting the volume-conducted signal, yielding a 'cleaned' local field potential, and second, quantifying oscillatory activity patterns such as gamma and ripple events in identified pathways using a modification of the Better Oscillation detection (BOSC) method. We suggest that ICA can be used to separate the independent pathways that contribute to network dynamics in the dorsal hippocampus.

2.2 Introduction

The increasing technological capacity to record high density multi-site electrical signals from the nervous system can be seen as both a blessing and a curse in neuroscience. While the greater density of recording sites allows for improved localization of the sources of recorded activity patterns, this localization is hindered to some extent by the fact that each electrode records an unknown mixture of local activity and volume conducted signals from elsewhere in the brain. This situation bears some resemblance to the idea of the 'cocktail party problem', in which the signals from several individual speakers must be recovered from only the mixed signals recorded at different microphones throughout a room (Figure 2.1A; Bell and Sejnowski, 1995). In mathematical terms (with matrices denoted with upper case plain type and vectors denoted with lower case, bold type), the underlying source signals ($\mathbf{s}$), are linearly mixed by some unknown mixing matrix (A), to produce the mixed signal ($\mathbf{x}$): $\mathbf{x} = A\mathbf{s}$. The problem is that only $\mathbf{x}$ is known, making the estimation of A and $\mathbf{s}$ difficult. Independent component analysis (ICA) attempts to solve this problem by using the additional constraint that the source signals should be statistically independent (for an excellent review, see Hyvarinen and Oja, 2000). Therefore the problem is to find A that maximizes the independence of $\mathbf{s}$. This approach has been used increasingly in the analysis of high-density EEG recordings, both for artifact removal (Jung et al., 2000; Castellanos and Makarov, 2006; Delorme et al., 2007; Chaumon et al., 2015; Wang et al., 2015) as well as localizing physiological sources of neural activity (Makeig et al., 1996; Jung et al., 2001; Milne et al., 2009; Bowers et al., 2013; Aoki et al., 2015).

We applied independent component analysis (ICA) to separate the underlying sources making up the mixed local field potential (LFP) signals recorded in the dorsal hippocampus of urethane anaesthetized rats. In contrast to the literature on the use of ICA in human EEG, this approach has only been used by a few groups to analyze local field potentials (LFP) from intracranial electrodes (Makarov et al., 2010; Glabska et al., 2014; Schomburg et al., 2014). Synaptic inputs to the dorsal hippocampus have a laminar organization, with distinct input pathways terminating at distinct layers along the CA1-dentate axis (Figure 2.1B). The CA1 subfield receives synaptic inputs from CA3 via the Schaffer collateral pathway at stratum radiatum (SRad), and from the entorhinal cortex through the temporoammonic pathway at stratum lacunosum moleculare (SLM). The dentate gyrus (DG) receives synaptic inputs from the lateral entorhinal cortex through the lateral perforant path (LPP) and from the medial entorhinal cortex through the medial perforant path (MPP). There is also a hippocampal projection from the nucleus reuniens of the thalamus (NRe) that overlaps spatially with the input from the temporoammonic pathway at SLM (Wouterlood et al., 1990; Dolleman-Van der Weel et al., 1997; Vertes, 2015). The combined activity of these intrahippocampal sources, in addition to volume conduction of activity from sources outside the hippocampus, all contribute to the LFP recorded locally. We conceive of this situation as the ‘cocktail party’ of the brain (Figure 2.1A), which can be unmixed by ICA into distinct sources associated with the major inputs to CA1 and the DG (Figure 2.1B; Benito et al., 2014; Schomburg et al., 2014).

There are currently several algorithms freely available with MATLAB implementation for performing ICA on electroencephalographic data. Hyvarinen (1999b) described all ICA methods as the combination of an objective (or contrast) function (that measures statistical independence) and an optimization algorithm. Different objective functions can lead to different results, and certain measures of statistical independence might be better suited to certain types of data. Furthermore, the interpretation of ICA components relies on their intra- and inter-

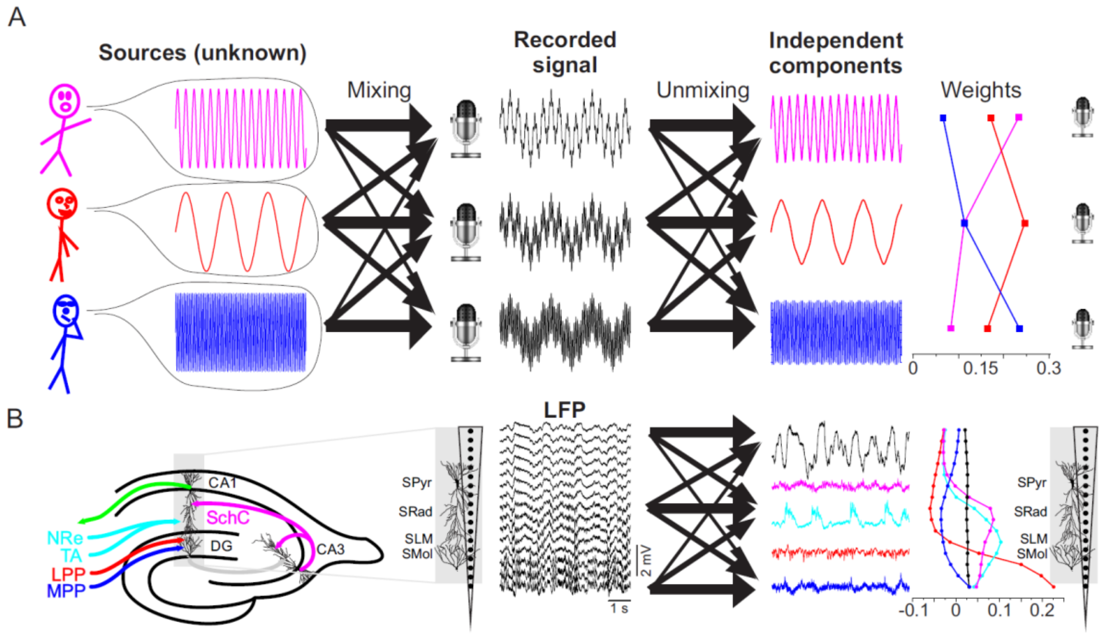

Figure 2.1 Schematic representation of the application of ICA to solving the cocktail party problem.

(A). If three speakers are talking simultaneously, and the signals are recorded at three separate microphones, the recorded signal at each microphone will be a linear mixture of the three signals, with the mixing matrix describing the proportion of each signal recorded by each microphone. The problem of ICA is to find the unmixing matrix that will separate the recorded signal into its underlying source signals without knowledge of the original sources or their mixing. This is achieved by maximizing some measure of independence of the components through some optimization procedure. The result is the separation of the recorded signal into the independent components and their mixing matrix, represented here as the relative weighting of each component at each electrode. (B). Extension of the cocktail party analogy to the LFP recorded in the dorsal hippocampus. Instead of microphones there is a linear array of electrodes, and the speakers are the individual hippocampal afferent pathways.

subject reliability. We wanted assess this approach systematically and to understand how it might be applied to solve important questions related to hippocampal network activity during a particular state: the hippocampal slow oscillation. Our first goal was to assess the reliability of ICA components across different algorithms, across different epochs (including transitions between states), and finally across different animals. Our second goal was to apply ICA results to solve two important problems: the removal of the volume-conducted component of the LFP signal, and the detection of oscillatory activity in separate input pathways.

2.3 Methods

All experimental procedures conformed to the guidelines established by the Canadian Council on Animal Care and followed protocols that were approved by the University of Alberta Biosciences Animal Care and Use Committee.

2.3.1 Animals and surgery

Data were collected from 17 male Sprague-Dawley rats (250 ± 12.5 g). Animals were placed in an enclosed chamber with 4% isoflurane in 100% oxygen until the loss of righting reflexes was observed, at which point they were transferred to a surgical table where isoflurane (1.5-2%) delivered through a nose cone while a catheter was inserted in the jugular vein. Isoflurane was discontinued and urethane (0.67-08 g/mL) was administered in small increments through the implanted catheter to a final dose of 1.71 ± 0.06 g/kg. Final urethane dosage was determined by a lack of behavioural responses including withdrawal to toe pad pressure and being placed in a stereotaxic frame (Model 900; David Kopf Instruments, Tujunga, CA, USA). Body temperature was maintained at 37 °C using a servo-driven heating pad connected to a rectal probe (TR-100; Fine Science Tools, Vancouver, BC, Canada). A subcutaneous injection of atropine methyl nitrate (0.05 mg/kg) was administered to prevent respiratory secretions. Supplemental urethane doses were given if animals showed spontaneous vibrissae movement or a reflex withdrawal to toe pad pressure.

A monopolar electrode consisting of Teflon-coated stainless steel wire (bare diameter 125 μm, A-M Systems, Carlsborg, WA, USA) was implanted in the frontal cortex (coordinates relative to Bregma: anterior-posterior (AP): +2.5 mm; medial-lateral (ML): +1.2 mm), in superficial (n=10, dorso-ventral (DV): -0.23 ± 0.01 mm) or deep (n=6, DV -1.73 ± 0.07 mm) cortical layers. A 16-channel linear multi-site electrode with 100 μm separation between contacts (silicon probes from Neuronexus, Ann Arbor, Michigan, USA or multi-site platinum-iridium electrodes from Plexon, Dallas, Texas, USA) was implanted in the dorsal hippocampus, targeting the CA1/dentate gyrus axis (AP -3.31 ± 0.03 mm; ML -2.27 ± 0.06 mm; DV -3.51 ± 0.07 mm). In a subset of animals, bipolar stimulating electrodes (twisted Teflon-coated wires, bar diameter 200 μm, A-M Systems, Carlsborg, WA) were implanted in the contralateral CA3 (n=2, AP -3.8 mm; ML -3.75 mm; DV -2.68 ± 0.38 mm) and/or in the ipsilateral angular bundle (n=6, AP -7.05 ± 0.12 mm; ML -4.08 ± 0.42 mm; DV -3.12 ± 0.33 mm). All static electrodes were fixed to the skull with dental acrylic.

2.3.2 Data collection

Recordings were referenced to stereotaxic ground. Monopolar electrode signals were amplified with a gain of 1000 and filtered from 0.1 Hz to 10 kHz using a differential AC amplifier (Model 1700, A-M Systems). Linear multiprobe signals were first passed through a headstage with unity gain (Plexon, Dallas, Texas) and then amplified at a gain of 1000 and filtered from 0.07 Hz to 8 kHz (PBX-2 amplifier, Plexon). Signals were then digitized with a sampling rate of 1000 Hz with anti-alias filtering at 500 Hz using a Digidata A/D board (Molecular Devices, Union City, CA) connected to a personal computer for data acquisition in Axoscope (Molecular Devices, Union City, CA). Bipolar stimulation electrodes were connected to an isolated current pulse generator (Model 2100, A-M Systems). Biphasic pulses of 100-250 μA for 0.2-0.5 ms were delivered to the angular bundle, and 100-150 μA for 0.2-0.5 ms were delivered to the contralateral CA3.

Following completion of data collection, animals were perfused transcardially with physiological saline followed by 4% paraformaldehyde, and brains were extracted and stored in a solution of 4% paraformaldehyde and 30% sucrose. After a minimum of 24 hours, brains were frozen with compressed CO_2 and 48 μm slices were taken using a rotary microtome (Model 1320, Leica, Vienna, Austria). Slices were mounted on gel-coated slides and allowed to dry before staining with thionin and cover-slipping. The position of the multiprobe within the CA1-dentate axis was verified.

2.3.3 Data Analysis

Analysis was performed using a combination of built-in and custom-written code in Matlab version 7.14 (The Mathworks, Natick, MA, USA). Matlab implementation of ICA algorithms were freely available (runica: Delorme and Makeig (2004); FastICA: Hyvarinen (1999a) and JadeR: Cardoso (1999)). ICA was computed on both wide-band and filtered (6-250 Hz) signals. Filtering of signals was performed using a zero-phase-lag (forward and backward) 3rd order Butterworth filter. Spatial weight profiles were all aligned with respect to the phase reversal of the theta (3-12 Hz) oscillation, which occurs just below the pyramidal cell layer in

CA1 (see Figure 1.4). Details of a normalization procedure for comparing weighting profiles across animals are found in the Results section.

Power spectra as well as power, phase and coherence profiles were calculated using Welch's averaged periodogram method with a 6-s Hanning window and 2-s overlap, with SLM as the reference channel. Alternatively, in some cases power spectra were computed using a 6-cycle Morlet wavelet across logarithmically spaced frequencies from 0.5-215 Hz. Current source density (CSD) was computed as the 2nd spatial derivative of the voltage traces.

The **B**etter **Osc**illation detection (BOSC) method was used to identify oscillatory events in separated independent components. The details of this method have been described previously, and Matlab code is freely available (Caplan et al., 2001; Whitten et al., 2011; Hughes et al., 2012). In brief, oscillations are detected only when both a power and a duration threshold are exceeded, and both of these thresholds are derived separately for each frequency. In the results we detail some modifications to the method that were found to improve performance in some cases.

2.4 Results

LFP signals were recorded from a linear array in the dorsal hippocampus of urethane anaesthetized rats (n=16; data from one animal were removed due to an electrode position medial to CA1). These animals showed rhythmic alternations between an activated state characterized by theta (3-12 Hz) oscillations in the hippocampus, and a deactivated state characterized by the slow oscillation (~1 Hz) in both the hippocampus and neocortex (Steriade et al., 1993b; Wolansky et al., 2006; Clement et al., 2008). These raw signals were used to assess the reliability of ICA results across algorithms, epochs and animals.

2.4.1 Reliability of ICA results across algorithms

Three different algorithms were evaluated: runica (Makeig et al., 1996; Delorme and Makeig, 2004), which uses the infomax principle to maximize independence of the components by maximizing their information content; FastICA (Hyvarinen and Oja, 2000; http://www.cis.hut.fi/projects/ica/fastica/), which uses one of several contrast functions to maximize non-gaussianity; and JadeR (Cardoso, 1999), which uses the 4th order cumulants to set up the objective function. Multiple options for both the FastICA and runica algorithms were assessed. FastICA can use either a symmetrical (all components at once) or a deflation (one component at a time) decorrelation approach. The default is the deflation approach. Furthermore, there are four different functions that can be used in its fixed-point algorithm: the third power (*pow3*), the hyperbolic tangent (*tanh*), the Gaussian (*gauss*), and the second power (*skew*). The runica algorithm can use either the default or 'extended' approaches (Lee et al., 1999), where the extended approach is better able to deal with sub-gaussian sources such as electrical line noise (Delorme and Makeig, 2004).

As a first pass, the comparability of spatial weightings of the ICA components was assessed. The maximum number of components that can be extracted is equal to the number of recording channels, which was 14 in the case of the representative example in Figure 2.2. With 14 components extracted, there were some components with a high degree of overlap across algorithms (Figure 2.2A*i*), some components with a moderate degree of overlap (Figure 2.2A*ii*), and many components with very flat or jagged spatial profiles, making them difficult to interpret. It seemed likely that results would be improved by reducing the dimensionality of the data prior to running the ICA. This is performed using principal component analysis (PCA) as a pre-processing step, and retaining only the first 'x' number of components. Determining 'x', or the optimal number of PCA components to retain is often done by looking for the bend in the scree plot of the proportion of variance explained by each principal component (Figure 2.2B*ii*, circled, n=16 animals). Based on this criteria, only 3-4 principal components should be retained. A scree plot in loglog space also showed only 4 components before the bend (circled, Figure 2.2B*iii*). However, based on the number of components that appeared consistently across algorithms, we decided to retain the first 6 principal components. While this was admittedly somewhat arbitrary, the reliability of components with similar profiles across subjects (see below) suggests that they are physiologically meaningful.

We identified components 1-6 based on the similarity of their spatial weighting profiles (Figure 2.2C-D). Independent component (IC) 1 (black) was the only one that did not cross the zero- axis (i.e. it did not reverse phase across depth). This suggested that it might represent the volume-conducted signal from the overlying cortex. IC2 (cyan) was maximal at -400 μm (all depths are relative to the phase reversal of theta activity, set as 0 μm). IC3 (red) reversed polarity at -400 μm. IC4 (magenta) was maximal at -100 μm. IC5 (blue) reversed polarity at -500 to -600 μm. Finally, IC6 (green) was maximal at 200 μm.

We first compared all three algorithms (Figure 2.2C*i*; runica *extended*, FastICA *symm*, *pow3*, and JadeR with default settings). ICs 1-4 and 6 were quite similar across algorithms, but IC5 had an unusual profile with the FastICA and JadeR algorithms, crossing the zero-axis 3 times, which seemed unlikely for a physiologically meaningful source. This criteria is based on the assumption that true neural sources should create a dipole in the electrical field, due to current leaving (or entering) the extracellular space from one point and the return current entering (or leaving) the extracellular space from another point. Dipolarity in ICA components of scalp EEG has been suggested as a measure of 'biological plausibility' (Delorme et al., 2012). We therefore excluded the JadeR algorithm from further analysis.

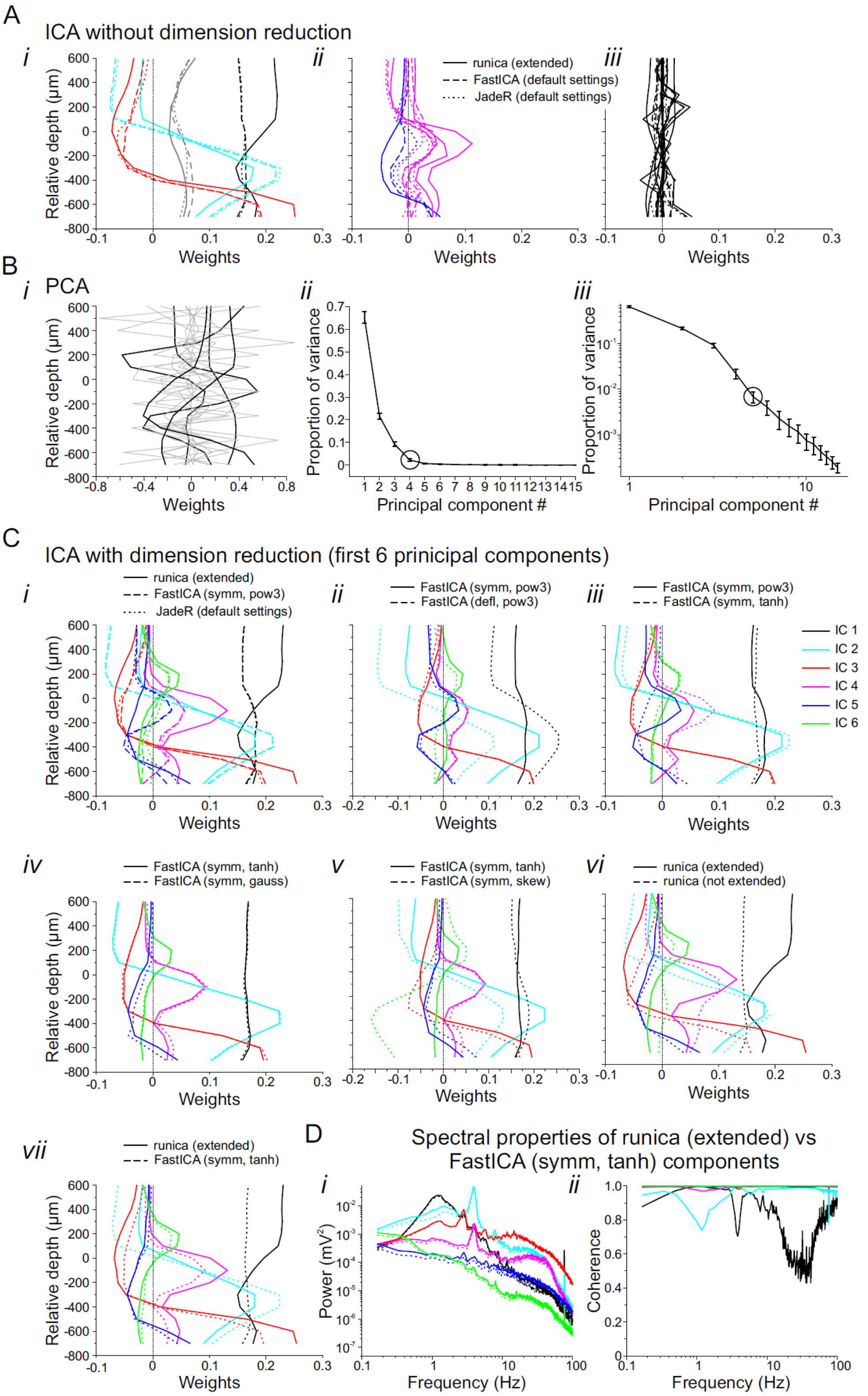

Figure 2.2 Comparison of ICA algorithms applied to the same dataset

Figure 2.2. Comparison of ICA algorithms applied to the same dataset.

(A) ICA component weightings from analysis of 600 seconds of data recorded from the dorsal hippocampus of a representative animal, analyzed using three different ICA algorithms (runica, FastICA and JadeR). The 14 components from each algorithm are separated into those that seem to overlap well across algorithms (*i*), those with a moderate degree of overlap (*ii*), and those with relatively flat or jagged profiles that are difficult to evaluate (*iii*). (B) The use of PCA as a pre-processing step to reduce the dimensionality of the data. (*i*) The first 5 principal components are shown in bold. (*ii*) The proportion of variance described by each principal component on average across animals (n=16). The bend in the scree plot is circled. (*iii*) The proportion of variance as a function of component number in loglog coordinates. (C) Comparison of ICA component weightings across different algorithms following dimension reduction to the first 6 principal components. There is enough similarity between components to classify them as component 1-6 (colour-coded) across algorithms. (*i*) runica (extended) vs FastICA (*symm, pow3*) vs JadeR (default settings). (*ii*) FastICA (*symm, pow3*) vs FastICA (*defl, pow3*). (*iii*) FastICA (*symm, pow3*) vs FastICA (*symm, tanh*). (*iv*) FastICA (*symm, tanh*) vs FastICA (*symm, gauss*). (*v*) FastICA (*symm, tanh)* vs FastICA (*symm, skew*). (*vi*) runica (extended) vs runica (default). (*vii*) runica (extended) vs FastICA (*symm, tanh*). (D) Power (*i*) and coherence (*ii*) spectra of components extracted with runica (extended) vs FastICA (*symm, tanh*).

However, FastICA has several options for its implementation, so we assessed each one at a time. The symmetrical decorrelation approach seemed to produce more plausible IC profiles than the deflation approach (Figure 2.2C*ii*). With the deflation approach, the presumed volume-conducted component (IC1, black), showed a large hump at -400 µm, suggesting that it might be mixed with IC2 (cyan). We therefore used the symmetrical approach for the remaining FastICA analyses. The next options to compare were the *pow3* vs *tanh* options (Figure 2.2C*iii*). In this case the *tanh* option did a better job with IC5 (blue), giving it only one zero-crossing. We therefore compared the next two FastICA options with *tanh*. The *tanh* and the *gauss* options were very similar (Figure 2.2C*iv*), although IC5 was slightly smoother with *tanh*. The final option for FastICA was *skew* (Figure 2.2C*v*), which seemed to mix ICs 2 (cyan) and 6 (green).

We then compared the runica extended and default options (Figure 2.2C*vi*). IC1 (black) with the default option was flatter, which was more realistic for a volume-conducted component. To look at the impact of slightly different component weighting profiles on the extracted components, we compared runica (extended) to FastICA (*symm, tanh*; Figure 2.2C*vii*). These and all other spectral and coherence estimates were calculated on the entire 10 minute epoch used for ICA separation for this animal. The power spectra of components extracted using the two algorithms were quite similar (Figure 2.2D*i*), and the coherence was very high (Figure 2.2D*ii*), with the exception of IC1 (black) at higher frequencies, as well as a dip in coherence at theta frequency (~4 Hz) for IC1 and at SO frequency (1 Hz) for IC2. Based on all comparisons, we found that the runica algorithm and the FastICA algorithm with symmetrical *tanh* or *gauss* approaches are quite comparable and produce components with physiologically plausible spatial profiles. To quantify the similarity between these four approaches, we calculated the average coherence of components extracted with each algorithm averaged over frequencies <100 Hz. The results are reported in the Table 2.1.

Table 2.1 Coherence of ICA components across algorithms

	runica *default*	runica *ext.*	fastica *tanh*	fastica *gauss*
runica *default*		0.87 ± 0.08	0.95 ± 0.04	0.96 ± 0.03
runica *ext.*			0.92 ± 0.07	0.91 ± 0.07
fastica *tanh*				0.99 ± 0.00
fastica *gauss*				

Average coherence in the 0-100 Hz range was calculated between components separated by different algorithms (compared pairwise). Reported values are mean ± SEM for the 6 components. Coherence values were computed on a 10 minute epoch using Welch's averaged periodogram method with a 6 second window and 2 second overlap between windows.

2.4.2 Reliability of ICA results across epochs and animals

Since ICA uses an iterative algorithm to converge on the optimal solution, different results could in theory be obtained from the same dataset. However, in our experience the differences are nearly imperceptible. To demonstrate this, ICA was run on the same dataset 10 times, and the results are overlaid in Figure 2.3. Only at high magnification (Figure 2.3 inset) can any differences be seen, suggesting that ICA results are highly reliable when given the identical dataset. However, a more important question is how robust the ICA components are to non-stationarities in the signal when analyzing different datasets from the same animal. To assess this, we

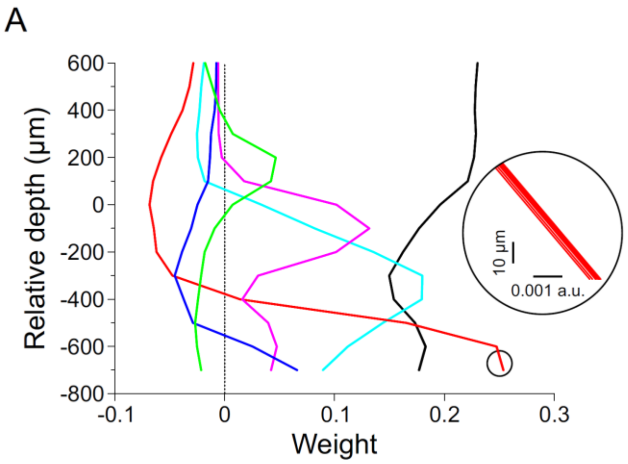

Figure 2.3 Reliability of ICA unmixing of the same dataset

(A) The overlay of component weightings of 10 separate implementations of ICA (runica, extended) on the same dataset. Only by zooming in (inset) are small variations in the results apparent.

separated the data from a representative animal into 6 equally spaced overlapping epochs (Figure 2.4A). Importantly, this included epochs that spanned transitions between deactivated and activated brain states (eg. Epoch 5, where SO power drops suddenly and theta power increases suddenly, corresponding to a transition from a deactivated to an activated state). We then used the unmixing matrix obtained from the individual epochs to unmix the entire dataset, and computed coherence of those components with the corresponding components extracted based on the full dataset. While components 1-6 could be identified reliably based on their spatial profiles across epochs (with the exception of component 5 (blue) in epoch 1; Figure 2.4B), there were obvious differences in the spatial weightings. These differences were more apparent when we looked at the coherence measures for the component time series (Figure 2.4C). The theta frequency (4 Hz) seemed particularly problematic across all epochs, especially for component 1 (black). The worst results for ICA separation were obtained from epoch 5 which spanned a state transition (Figure 2.4B-D*v*). Nevertheless, across most epochs the characteristics of the activations associated with each component were visually similar (Figure 2.4D). We performed the same analysis using FastICA (*symm*, *tanh*), and on average there was a similar pattern with some epochs producing very poor coherence, and particular problems at theta frequency. However, interestingly FastICA performed worst on epochs 1, 2 and 4, and best on epochs 3 and 5, suggesting that its unmixing performance was actually improved by state transitions (data not shown). The runica (default) algorithm performed worse across all epochs compared to both the extended version (shown in Figure 2.4) and the FastICA.

Despite these differences between algorithms, the strong power of theta oscillations seemed to be confounding the ICA analysis to some degree. One approach to mitigate this problem was to filter the signal prior to implementing the

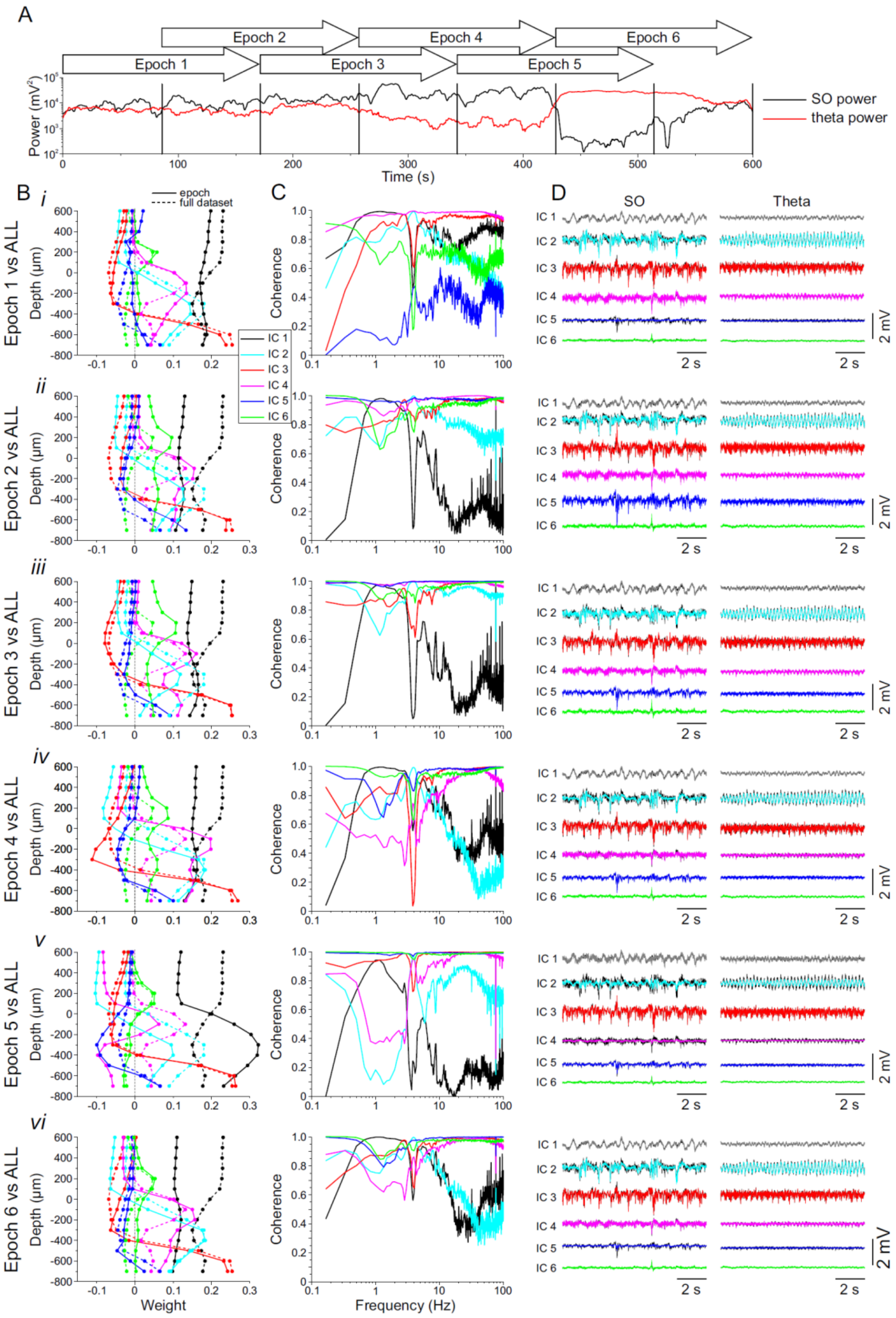

Figure 2.4 Reliability of ICA unmixing across different epochs within the same dataset

Figure 2.4. Reliability of ICA unmixing across different epochs within the same dataset.

(A) The power of SO (black) and theta (red) across 600 seconds of data from a representative animal. Note the sharp state transition at ~420 seconds characterized by a reduction in SO power and an increase in theta power. This dataset was divided into 6 overlapping epochs and ICA (runica, extended), was run on the individual epochs and compared to ICA results from the entire dataset. (B) Overlay of the component weightings from the individual epochs (solid line) vs the full dataset (dashed line) for all 6 epochs (*i*-*vi*). (C) Coherence between components separated based on the unmixing matrix from the epoch or from the full dataset. Notice the poor performance at the theta frequency (~4 Hz) as well as in epoch 5 that includes the state transition. (D) Time series of the components extracted using the unmixing matrix from the epoch (coloured traces) overlayed on the components extracted using the unmixing matrix from the full dataset (black traces) during SO and theta states. (Grey – IC1; Cyan – IC2; Red – IC3; Magenta – IC4; Blue – IC5; Green – IC6).

ICA. When we band-pass filtered the LFP between 6-250 Hz, the ICA reliability across epochs was drastically improved (Figure 2.5A-C). After filtering, we no longer saw component 6 (green), and therefore we reduced the dimensions to the first 5 principal components. The component weights for all 6 epochs are overlaid in Figure 2.5A, and the coherence measures for all components and all epochs are overlaid in Figure 2.5B, with coherence above 0.8 in almost all cases across all frequencies. Notably, this includes cases where the ICA was run only on the activated state or only on the deactivated state, but the unmixing results on the whole dataset were nearly identical. In addition, when we looked at coherence between the runica *default* and fastica *tanh* algorithms (as in Table 1) after pre-filtering, the average coherence increased to 0.9998 ± 0.00005. The time series of these components show some interesting dynamics, including the periodic bursts of high frequency activity in component 2 during SO (Figure 2.5C). Based on the reliability of ICA separation across epochs with the band-pass filtered signal, we recommend filtering out strong oscillations such as theta prior to ICA implementation.

In some cases the dynamics of slow (<6 Hz) frequencies may be of interest. One approach for looking at these slow dynamics would be to use the unmixing matrix from the filtered dataset to unmix the unfiltered (wide-band) signal. This approach produces component time courses that look very similar to those obtained from ICA of the wide-band signal (Figure 2.6C). The coherence of the wide-band vs filtered ICA components shows that these results are not identical. However, which approach best represents the 'true' underlying sources for slow frequencies is unclear. It is interesting to note that the coherence of the presumably volume conducted component (black) is very high using both filtered and wide-band approaches at ~1 Hz, which is the frequency of the slow oscillation. This suggested that in both cases the volume conducted signal is well separated by the ICA. Due to

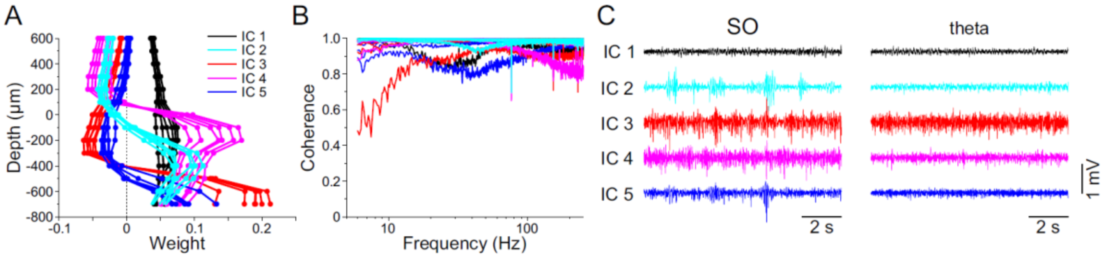

Figure 2.5 Reliability of ICA unmixing across different epochs after pre-filtering

ICA was performed on the same epochs as in Figure 2.4, with band-pass filtering from 6-250 Hz as a pre-processing step. (A) Overlay of component weightings from all 6 epochs. (B) Coherence spectra of components separated based on the unmixing matrix from each epoch compared to those from based on the unmixing matrix from the full dataset. All comparisons for all epochs are overlayed. The only conspicuous drop in coherence is for IC3 derived from epoch 1 at the frequencies below 20 Hz. (C) Time courses of the extracted components based on the full dataset, during the same SO and theta samples shown in Figure 2.4D.

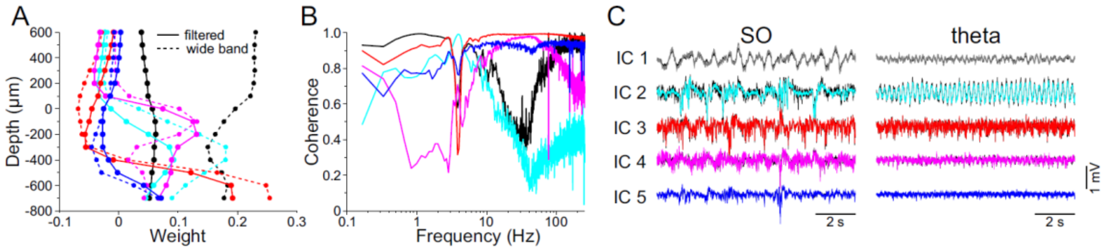

Figure 2.6 Unmixing the wide-band signal using the ICA results from the filtered signal

(A) Comparison of component spatial weighting profiles for ICA performed on the filtered (solid) vs. the wideband (dashed) signal. (B) Coherence between components obtained from the filtered vs the wide-band unmixing matrices. Colours correspond to the components in C. (C) Time courses of components obtained from the filtered (coloured traces) vs. the wide-band (black traces) unmixing matrices.

the better reliability of the band-pass filtered ICA results across epochs (Figure 2.5), we are more inclined to trust the results from this procedure. We also ran the ICA on low-pass filtered signals (<6 Hz), as well as on data that were 'whitened' by taking the differential of the continuous signal, however the separation was worse than for the wide-band signal in both cases (data not shown), so these approaches were not pursued further.

Once we were able to obtain reliable ICA results within a single animal through pre-filtering, the next step was to assess the consistency of ICA components across animals. To compare components across animals, we needed a method to align the spatial weighting profiles. We took advantage of the fact that the peak power of the theta oscillation occurs at stratum lacunosum moleculare (SLM), and the phase of the theta oscillation reverses just below the pyramidal cell layer (see Figure 1.4 of Chapter 1). This gave us two points to use in the alignment. The depth of the theta phase reversal was set as 0 μm. The distance from the reversal to the power maximum was typically 400 μm, however it could range from 300 – 500 μm due to differences in electrode position (Figure 2.7A inset) and individual brain morphology. We therefore scaled the profiles to normalize this distance to 400 μm, and used cubic spline interpolation to derive averages at 100 μm intervals.

The results after scaling of the spatial profiles are shown in Figure 2.7B and D, and the averages for the identified components in Figure 2.7C. While there is some variability when components are compared across animals, some of this could be due to imperfect alignment and scaling (100 μm resolution for estimating theta phase reversal and power maximum could contribute some error). Nevertheless, consistent features such as the depth of maximal activation and the depth of phase reversals made identification of individual components quite clear in most cases. Based on the consistency across animals and the relation to the depths of known

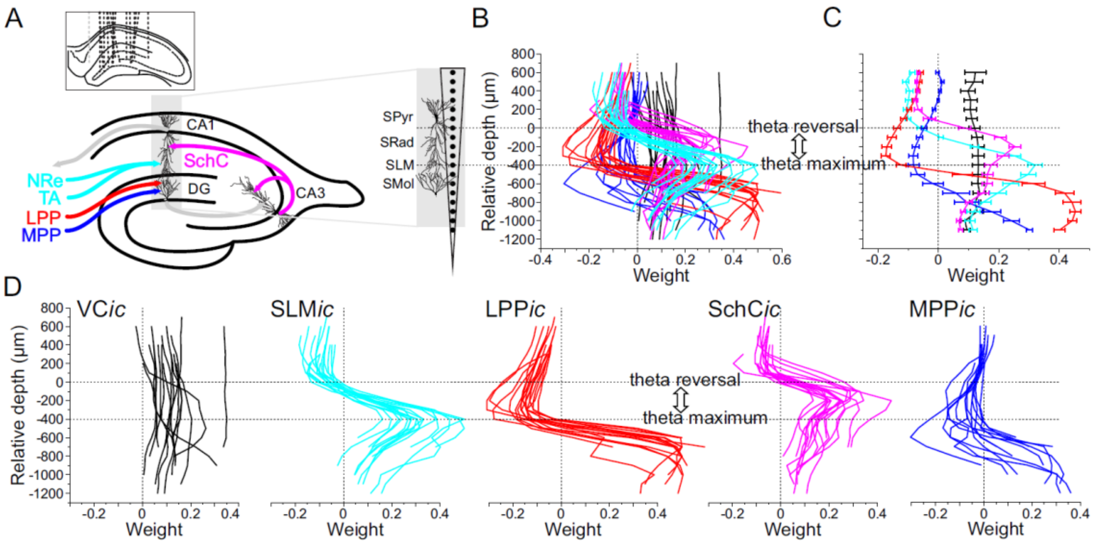

Figure 2.7 Reliability of ICA components across animals

(A) Schematic representation of recording location within the dorsal hippocampus, showing the main synaptic inputs and their spatially organized termination zones. Actual positions of multiprobe across animals are shown in the inset. Data from the light grey electrode were excluded due to medial position with respect to CA1. (B). Overlay of components from all subjects (n=16) after scaling based on the depth of theta reversal and the maximum theta power. ICA was performed using the runica (extended) algorithm after pre-filtering between 6-250 Hz. (C) Average ± SEM of the identified components across all animals. (D) Same plot as in B but separated to show each component individually.

synaptic inputs to the hippocampus, the components were putatively identified (Figure 2.7D): the volume conducted component (VC*ic*, black, no reversal of polarity); the SLM component (SLM*ic*, cyan, peak ~ -400 μm); the lateral perforant path component (LPP*ic*, red, polarity reversal ~ -400 μm); the Schaffer collateral component (SchC*ic*, magenta, peak ~ -200 μm); and the medial perforant path component (MPP*ic*, blue, polarity reversal below -400 μm).

In a subset of animals we stimulated either the CA3 subfield or the angular bundle to activate the Schaffer collateral pathway or the rhinal (perforant and temporoammonic) pathways respectively. When the unmixing matrix from the spontaneous data was used to unmix the evoked potentials, we saw activation exclusively in the SchC*ic* following CA3 stimulation (Figure 2.8A), and activation in one of the SLM*ic*, MPP*ic* or LPP*ic* exclusively following angular bundle stimulation (Figure 2.8B-D). While this was only done in a subset of animals, we took it as one piece of evidence supporting the putative identities of the components.

2.4.3 Applications: removing the volume conducted component of the signal

The spectrum of the VC*ic* was highly similar to that of the signal recorded in the frontal cortex during both activated and deactivated states (Figure 2.9A). When the time series of the cortical signal and the VC*ic* are overlaid, the similarity is striking (Figure 2.9C). A common method for removing the influence of volume conduction from a signal is current source density (CSD), which transforms the signal by taking the second spatial derivative of the voltage traces. However, ICA was originally used primarily to remove eye movement artifacts from human EEG signals (Jung et al., 2000), so we hypothesized that it could be used here as well to remove the volume conduction 'artifact' from the local hippocampal signal (Figure

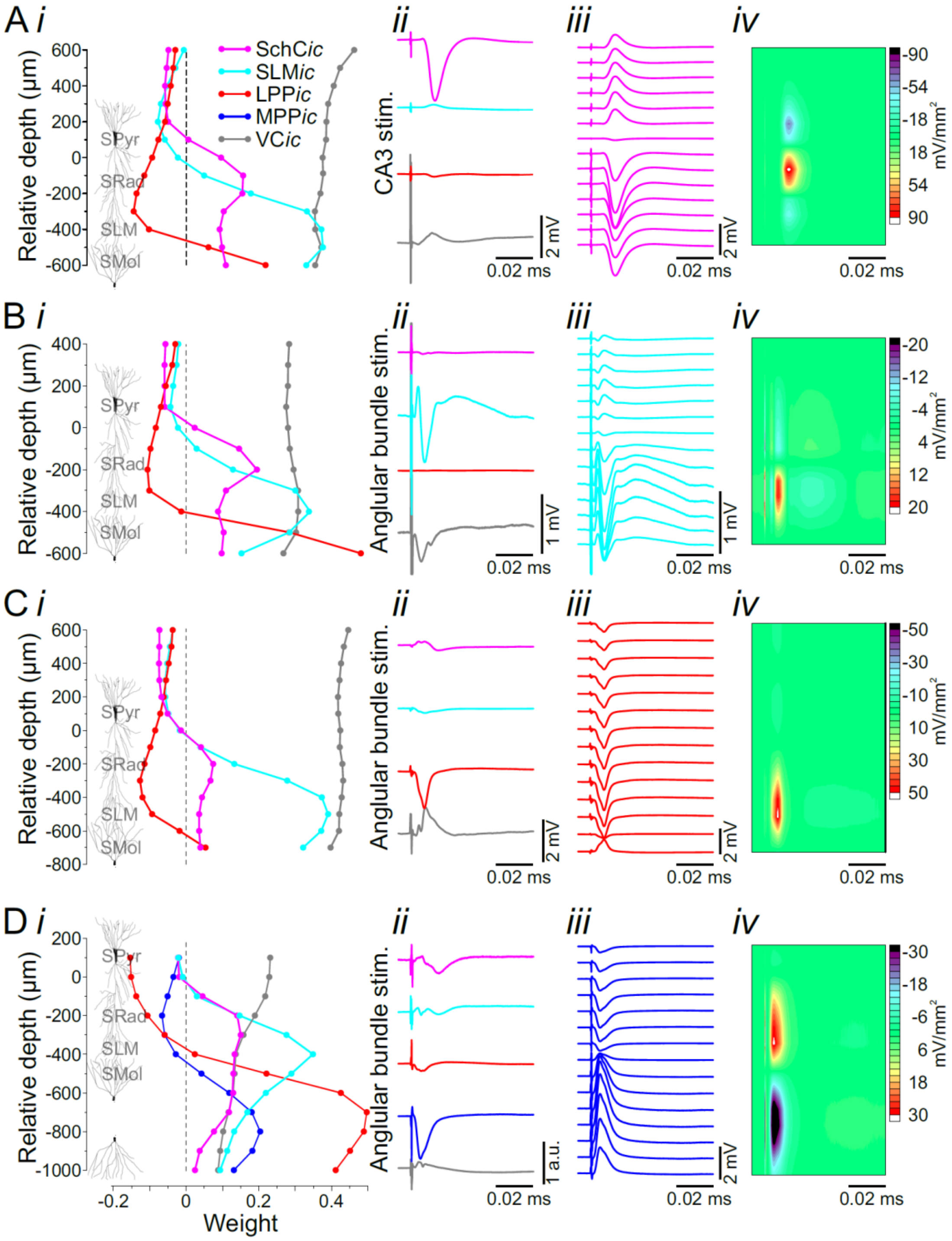

Figure 2.8 Evoked potentials from stimulation of afferent pathways is captured by the corresponding ICA components

Figure 2.8. Evoked potentials from stimulation of afferent pathways is captured by the corresponding ICA components.

(A) Stimulation of CA3 activates the SchC*ic*. (*i*) ICA weights for this subject based on spontaneous activity (no stimulation); colours are consistent with those presented in previous figures. (*ii*) Time course of activation of each component during the evoked potential, obtained by using the inverse of the unmixing matrix from the spontaneous data. Amplitude expressed in mV at the depth of maximal negativity of the raw evoked potential. The evoked potential is clearly captured in the time course of the SchC*ic* with minimal activation of the other components, as expected if the SchC*ic* represents the activity of the SchC pathway. (*iii)* Stimulation-evoked LFP for the SchC*ic*. (*iv*) Stimulation-evoked CSD for the SchC*ic*, showing a large sink at SRad. (B-D) Stimulation of the angular bundle activated the SLM*ic* (B), the LPP*ic* (C) or the MPP*ic* (D) in individual animals. Panels *i*-*iv* are as described in A. In all cases, the stimulation primarily activated a single ICA component (panels *ii*).

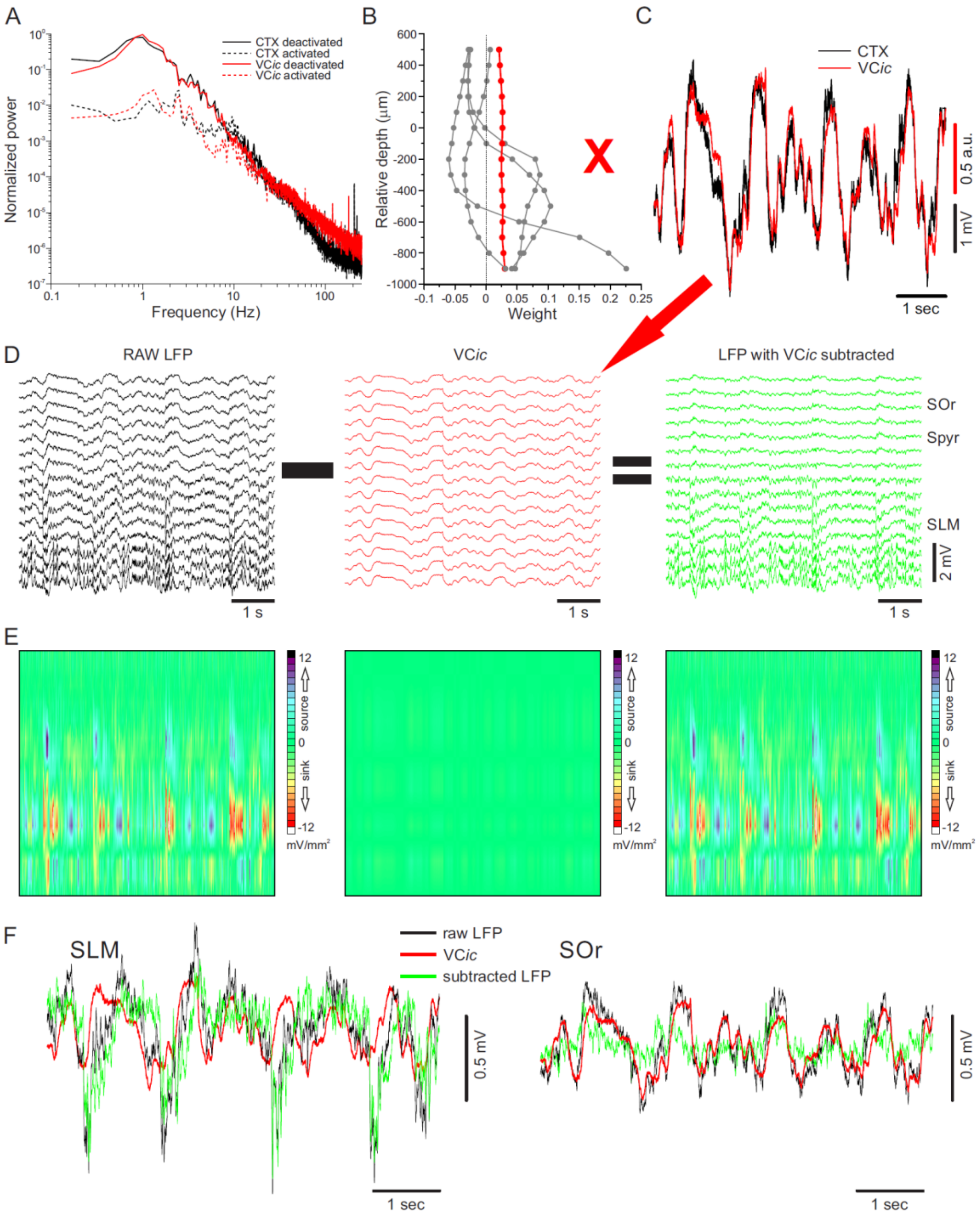

Figure 2.9 Applying ICA to remove the volume conducted component of the LFP signal

Figure 2.9. Applying ICA to remove the volume conducted component of the LFP signal.

(A) Power spectra (normalized by total power during a 2 minute sample of the deactivated state) for the frontal neocortical signal (CTX; black) and for the VCic (red) during both deactivated (solid) and activated (dashed) states. (B) ICA component weightings for this animal with the VCic shown in red. (C) Overlay of the time course of the VCic and the CTX signal. (D) Visual demonstration of the subtraction of the VCic component (red) from the raw LFP (black) to yield the 'local' LFP without the contribution of volume conduction (green). Note that the VCic signal is obtained by multiplication of the component weighting in B by the activation time course in C. While both B and C are unitless, the time series in D is in mV. (E) CSD analysis of the raw LFP (left), VC*ic* (middle) and the subtracted LFP (right). Note that the VC*ic* is not associated with any sinks or sources, as expected for a volume conducted signal. The CSDs of the raw and subtracted LFPs are nearly identical. (F) Overlay of the raw LFP signal (black) with the VC*ic* (red) and the subtracted LFP (green) at SLM and at stratum oriens (SOr). Notice that at SLM most of the signal is local, whereas at SOr most of the signal is volume conducted.

2.9D). The CSD of the subtracted signal was identical to the CSD of the raw signal, while the CSD of the VC*ic* showed no current sinks or sources (Figure 2.9E). Across animals, the average coherence of the raw CSD with the VC-subtracted CSD (averaged across channels and frequencies <100 Hz) was 0.991 ± 0.004 (n=16). We also looked at the coherence for the wide-band ICA separation, which was 0.986 ± 0.004 (n=16), suggesting that both approaches are reliable for subtracting the volume conducted signal. This subtraction showed that the hippocampal LFP at SLM is predominantly locally generated (Figure 2.9F, left panel), while the LFP at stratum oriens (above the pyramidal cell layer) is predominantly volume-conducted from other areas of the brain (Figure 2.9F, right panel). The absence of a full phase reversal of 1 Hz activity in the hippocampus has been used to suggest that the SO is not generated locally in the hippocampus. However, when the influence of volume conduction is subtracted, a 180° phase reversal of 1 Hz activity emerges, approximately 100 μm ventral to the theta phase reversal at 0 μm (Figure 2.10D).

2.4.4 Applications: identifying oscillatory events in ICA components using the Better Oscillation detection method (BOSC)

Once the underlying sources of the hippocampal LFP were separated with ICA and putatively identified, the next step was to identify and characterize oscillatory activity patterns in each of the putative pathways. We wanted to use the BOSC method to identify oscillations based on both an amplitude (power) and a duration threshold (Figure 2.11; Caplan et al., 2001; Whitten et al., 2011; Hughes et al., 2012). Briefly, the duration threshold is set as 3 (or more) cycles of an oscillation at a given frequency. The amplitude threshold is based on estimating the background spectrum by fitting the theoretical 1/f shape of the actual spectrum (Pritchard, 1992), and taking this estimate as the mean of the $\chi^2(2)$ distribution of power values

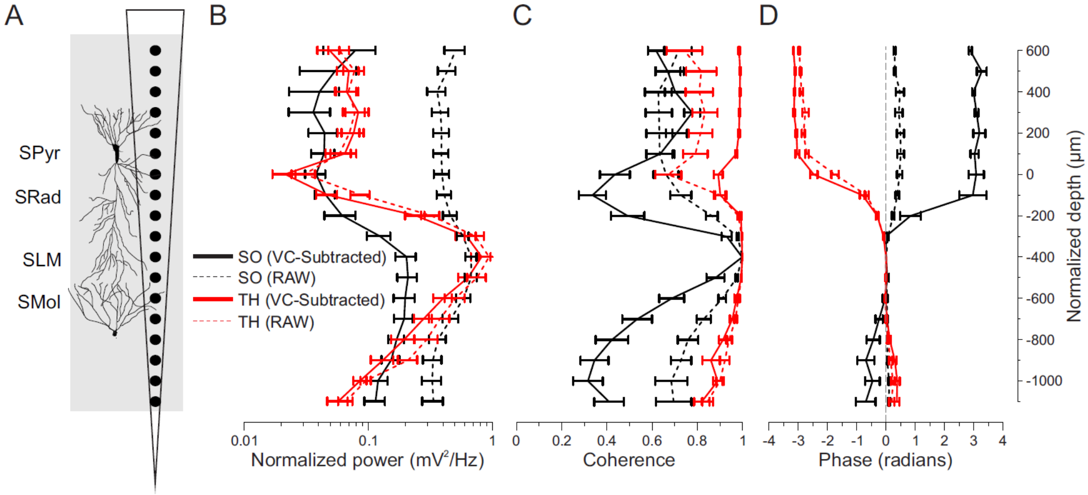

Figure 2.10 Power, coherence and phase profiles of SO and theta activity before and after subtraction of the VCic

(A) Schematic representation of the location of the recording electrode with respect to the cell layers within the hippocampus. Mean power (B), coherence (C), and phase (D) profiles as a function of depth for SO (black) and theta (red) activity before (dashed) and after (solid) the subtraction of the VC*ic* across animals (n=16). Power was normalized by the total power during a 2 minute sample of the deactivated state. Coherence and phase were calculated with reference to the channel at SLM (-400 µm). Note the appearance of a phase reversal for SO activity after subtraction of the VC*ic*.

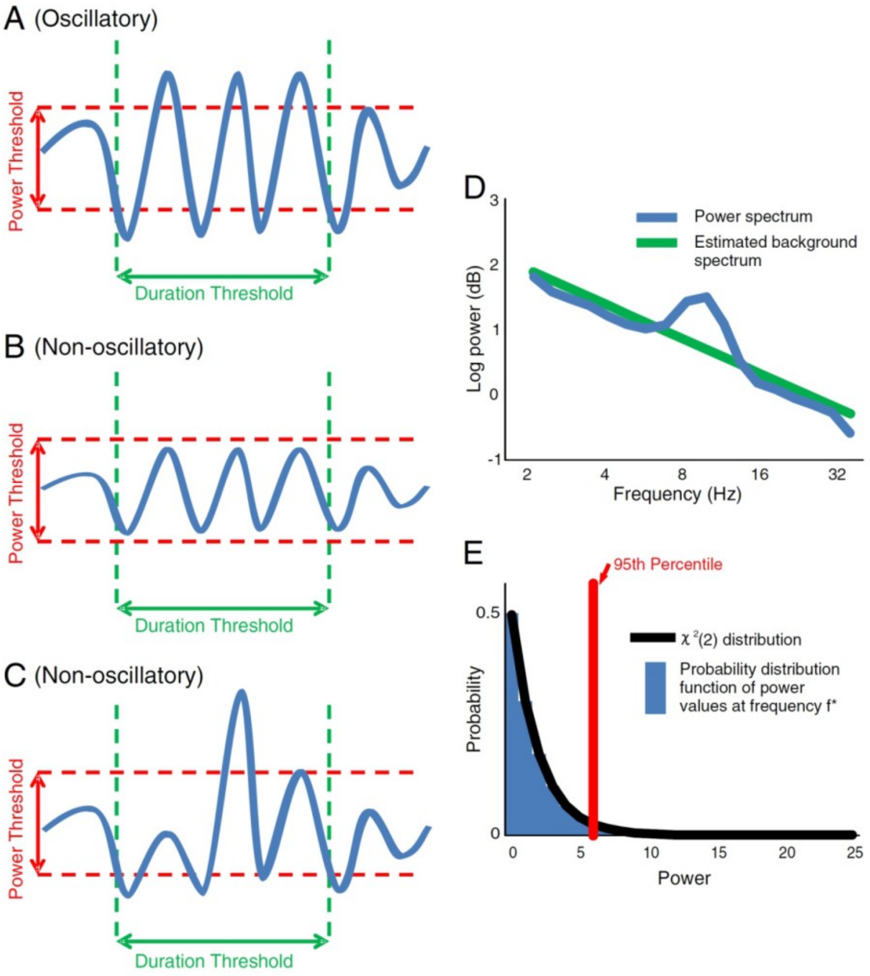

Figure 2.11 Schematic description of the BOSC method for oscillation detection

The BOSC method is based on setting an amplitude (or power) and duration threshold for each frequency, in order to detect oscillatory activity such as that in (A) that exceeds both thresholds, but to exclude activity such as that in (B) that does not exceed the amplitude threshold, as well as activity such as that in (C) that does not exceed the duration threshold. The duration threshold is set based on 3 (or more) cycles of an oscillation at a given frequency. (D) The first step in determining the amplitude threshold is to fit the background spectrum in order to estimate the mean power in the absence of oscillations. (E) The second step is to use the power from the background fit in (D) as the mean of the theoretical $\chi^2(2)$ distribution of power values in order to determine an appropriate power threshold such as the 95th percentile. Reproduced from Whitten et al. (2011).

at each frequency. The threshold can then be set as the 95th or 99th (or other) percentile of this theoretical $\chi^2(2)$ distribution. The reliability of the BOSC method depends on a good fit of the background spectrum. We found that our experimentally derived spectra were deviating significantly from the theoretical 1/f shape, and therefore were not well-estimated by the linear fit (Figure 2.12A, dotted line in all three panels). This was true for both raw and ICA signals. The deviation from 1/f was particularly problematic during the activated state when the spectrum was dominated by the theta (4 Hz) frequency (Figure 2.12A middle panel). We therefore implemented a modification to the BOSC method by fitting the spectrum with a 2nd degree polynomial, thereby allowing a curved estimate of the background spectrum (Figure 2.12A, solid red line).

The problems associated with a poor estimate of the background spectrum are illustrated in Figure 2.12B. The linear fit was over-estimating the mean power at the low end of the spectrum (0.6 Hz, Figure 2.12B*i*, right panel). This is also apparent in the spectra (Figure 2.12A), where the linear fit is always well above the actual spectrum at low frequencies across brain states. This over-estimation of the mean results in too few detections, because the actual distribution of power values is not well fit by the theoretical $\chi^2(2)$ distribution with the inflated mean. The opposite problem is seen at 9.5 Hz, where underestimation of the mean power results in too many detections (Figure 2.12B*ii*, right panel). Many power values lie beyond the 99th percentile of this under-estimated $\chi^2(2)$ distribution. On the other hand, the curved fit does a much better job of fitting the actual distributions of power values (Figure 2.12B, left panels), although at 152 Hz (Figure 2.12B*iv*), the curved fit is under-estimating while the linear fit is over-estimating the mean power.

Using the BOSC method with the modification of a curved fit of the background spectrum and a 36-second sliding window to estimate the background,

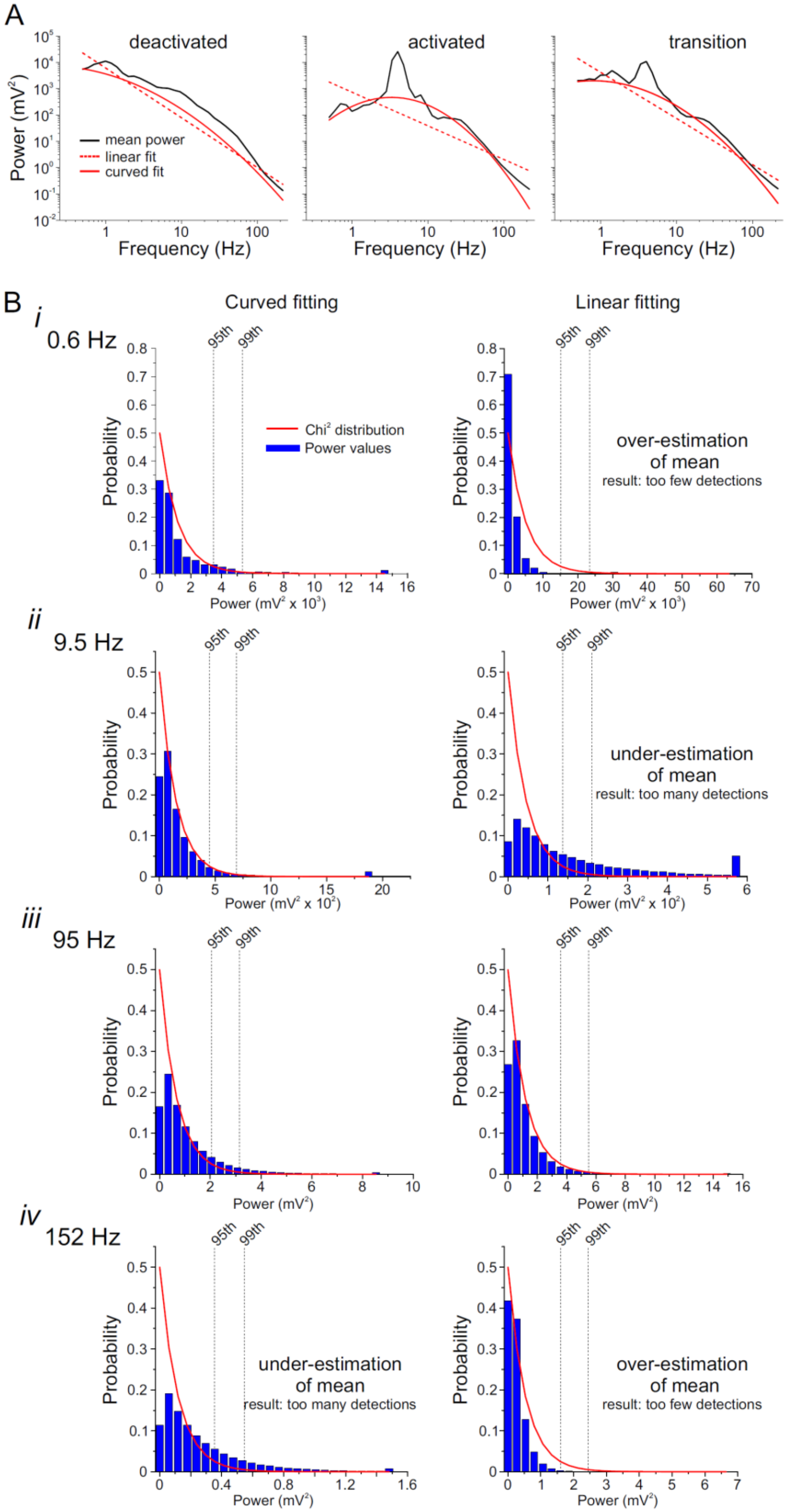

Figure 2.12 Linear vs curved fitting of the background spectrum for BOSC

Figure 2.12. Linear vs curved fitting of the background spectrum for BOSC.

(A) Examples of the estimation of the background spectrum across 36-second windows during deactivated (left), activated (middle) and transition (right) states in a representative animal. The experimentally determined mean power (black) deviates from the theoretical 1/f shape, and is therefore better fit using a curved instead of a linear fit. (B). The consequences for the method of under- or over-estimating the background spectrum are shown across different frequencies (0.6 Hz to 152 Hz) with the actual distribution of power values (blue bars) plotted with the theoretical $\chi^2(2)$ distribution in red. Any values beyond the scale are plotted in the highest bin. Notice that the linear fit (right panels) over-estimates the mean power for low (*i* – 0.6 Hz) and high (*iv* – 152 Hz) frequencies, leading to too few detections, while it under-estimates the mean power for mid-range frequencies (*ii* – 9.5 Hz), leading to too many detections. At ~95 Hz (*iii*), the curved and linear fits are close, and both provide reasonable estimates of the background spectrum as shown in the close fit between the distribution of actual power values and the theoretical $\chi^2(2)$ distribution. The curved fit (left panels) does a better job of fitting the power distributions, however it tends to under-estimate the mean at high frequencies (*iv* – 152 Hz).

we were able to identify oscillations in the SLM*ic* in the gamma range (20-100 Hz). We took two approaches – first, unmixing the wide-band signal and fitting the spectrum from 0.5 – 215 Hz (Figure 2.13A and 13B*i*), and second unmixing only the band-pass filtered signal (6-250 Hz) and fitting the spectrum in the 8-215 Hz range (Figure 2.13B*ii*). Both approaches identified gamma (32 Hz) oscillations at the same time points. The periodic nature of the bursts of gamma that are evident in the SLM*ic* was striking. The question of how these events are related to the phase of the very rhythmic SO in the cortex (Figure 2.13B*iii*) will be addressed in Chapter 3.

A final challenge for the BOSC method was to identify ripple oscillations in the pyramidal cell layer. Ripple oscillations during slow wave sleep have been associated with the replay of firing sequences from prior waking states (Girardeau et al., 2009; Ego-Stengel and Wilson, 2010), and they are triggered by large depolarizing events in the Schaffer collateral pathway. While we sometimes saw a component that was maximal at the pyramidal cell layer (see component 6, green, Figures 2.2 and 2.4), this component sometimes disappeared in the filtered signal and furthermore it was not reliable across animals. Therefore, to examine ripple oscillations we used the CSD of activity at the pyramidal cell layer. Ripples present a unique problem for BOSC because they are quite rare but very large amplitude (see sporadic large spikes in 128 Hz power, Figure 2.14B). The green line in Figure 2.14B represents the 99th percentile threshold based on the $\chi^2(2)$ distribution (Figure 2.14A). It is clear that if we are only interested in the very large ripple events, this threshold is too low. We are likely looking for the very rare events represented by the bin at the far right of the distribution in Figure 2.14A (circled). We therefore set the power threshold at the 99.99th percentile, and found reliable detection of ripple oscillations in the pyramidal layer CSD. These detections (Figure 2.14C, red) coincided very well with the traditional ripple detection method based on the smoothed root-mean-

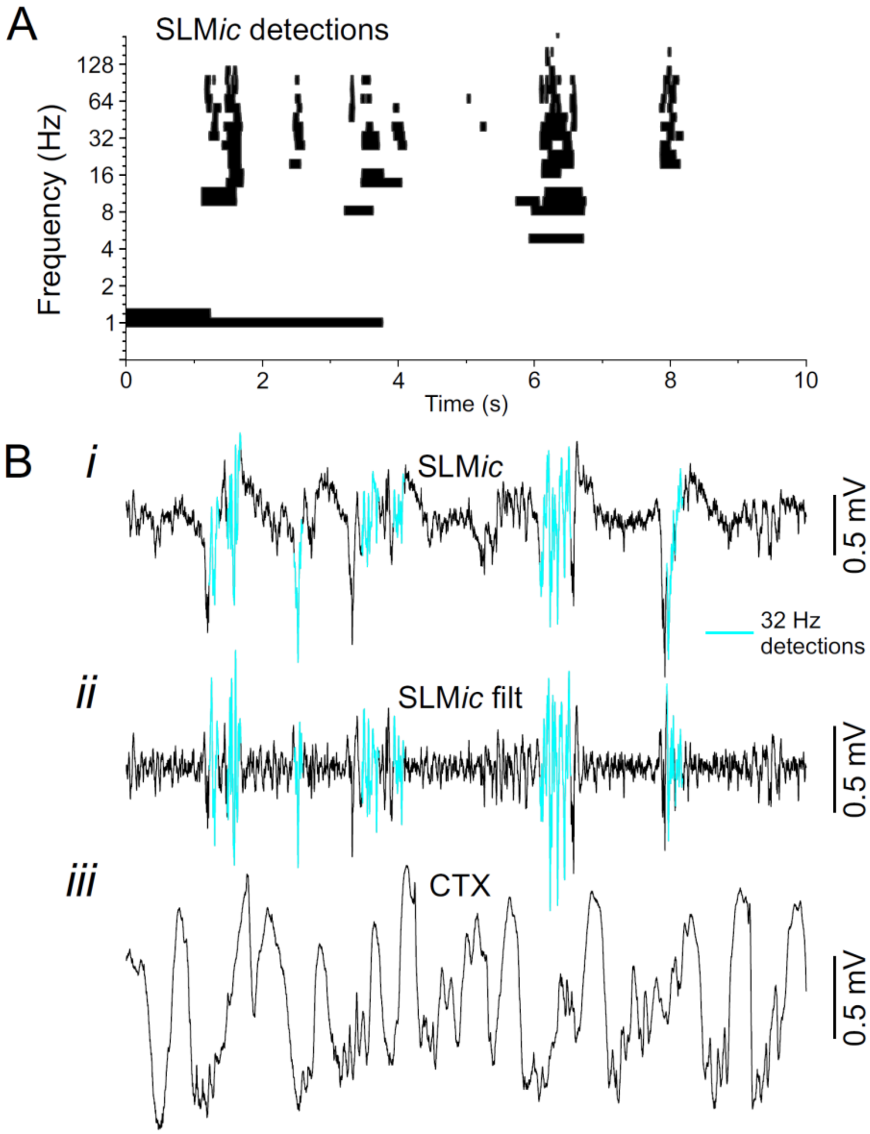

Figure 2.13 Examples of BOSC oscillation detection in the SLM*ic*

(A) Detection of oscillations (black) detected in the SLM*ic* during the 10 second epoch shown in Figures 4-6 (for the SO state). Note the detection of the ~1 Hz SO, as well as periodic detections of higher frequency oscillations in the spindle (8-16 Hz) and gamma (20-100 Hz) ranges. (Bi) Detected oscillations at 32 Hz (cyan) superimposed on the SLM*ic* signal. The background was fit in the range from 0.5-215 Hz. (ii) Detected oscillations at 32 Hz (cyan) superimposed on the filtered (6-250 Hz) SLM*ic* signal. The background was fit in the range from 8-215 Hz. (iii) The simultaneously recorded neocortical signal. Note that the SLM*ic* is only active on some cycles of the neocortical SO.

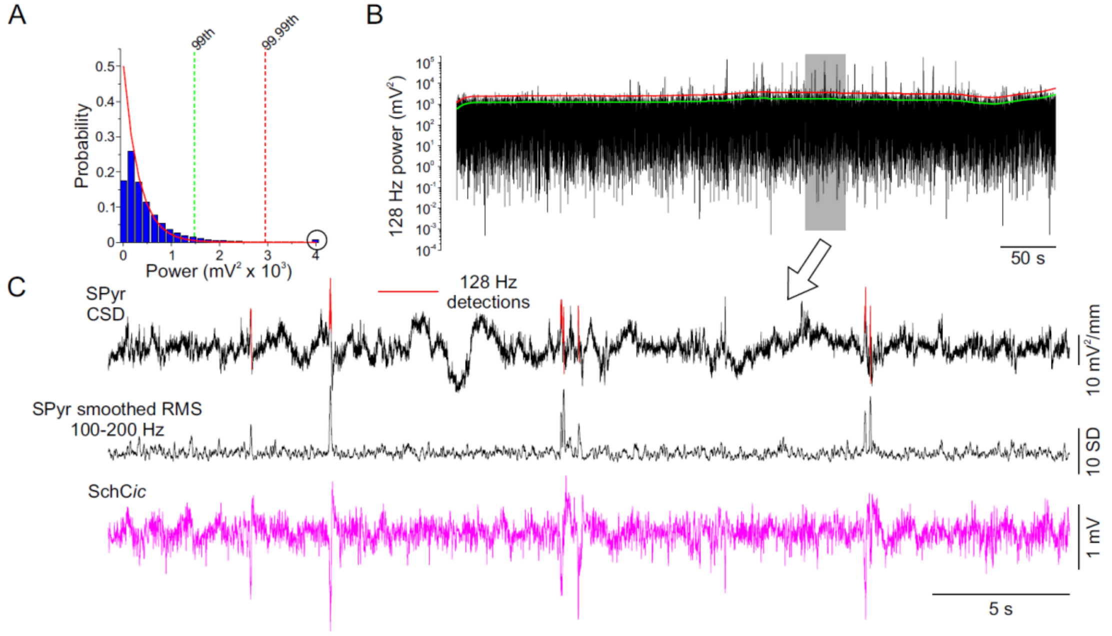

Figure 2.14 Detection of hippocampal ripples using BOSC

(A) The theoretical $\chi^2(2)$ distribution and the actual distribution of power values at 128 Hz for the pyramidal layer CSD for a representative animal. Note the bin at the far end of the distribution (circled) with more than the expected proportion of power values. (B) Wavelet power values for 128 Hz. The sporadic, high power events are likely ripple oscillations. The 99th (green) and 99.99th (red) percentiles shown in (A) are plotted. (C) Top panel: CSD at stratum pyramidale (SPyr) with the detection of ripples (128 Hz) using the 99.99th percentile threshold highlighted in red. The traditional ripple detection method of the smoothed RMS of the 100-200 Hz filtered SPyr signal is shown in the middle panel. The lower panel shows the coincidence of detected ripples with sharp waves in the SchCic.

square of the 100-200 Hz filtered pyramidal layer signal (Figure 2.14C, middle panel). Furthermore, they were strongly associated with the occurrence of sharp waves in the SchC*ic* as expected (Figure 2.14C, lower panel). We therefore suggest that the BOSC method with an increased amplitude threshold is an efficient method for detecting ripple oscillations in the hippocampus.

2.5 Discussion

We have presented evidence that ICA is a valuable tool in understanding the activity of spatially segregated inputs to the dorsal hippocampus. This supports work by other groups, in particular that of the Herreras lab (Makarov et al., 2010; Makarova et al., 2011; Fernandez-Ruiz et al., 2012b; Fernandez-Ruiz et al., 2012a; Fernandez-Ruiz and Herreras, 2013; Fernandez-Ruiz et al., 2013; Martin-Vazquez et al., 2013; Benito et al., 2014; Makarova et al., 2014) as well as others (Schomburg et al., 2014). In comparing results across ICA algorithms, as well as the stability of ICA components across epochs and between animals, we are able to make some recommendations in terms of the implementation of ICA methods to hippocampal signals.

We evaluated the outputs of different ICA algorithms based on the physiological plausibility of the components, as well as the flatness of the spatial profile of the volume conducted signal. Based on this, we found the best performance with the runica algorithm (slightly improved performance with the default vs. the extended versions), and the FastICA algorithm with a symmetrical decorrelation approach and either *tanh* or *gauss* settings for the objective (contrast) function. Hyvarinen (1999a) did suggest that *tanh* was a good all-purpose contrast function, whereas *gauss* was better with super-gaussian components, and *pow3* was only suggested when the sources are sub-gaussian and there are no outliers.

When we assessed the reliability of ICA across different epochs from the same dataset, we found that the theta frequency was particularly problematic, and sharp transitions between brain states also appeared to contribute to unreliable estimates of the unmixing matrix. However, when we filtered out the slow frequencies (band-pass filter, 6-250 Hz), the ICA reliability was dramatically improved and there were no longer problems with state transitions or with particular frequency bands. We therefore recommend filtering out the slow frequencies prior to ICA implementation. If the analysis of slow frequencies is desired, the unmixing matrix from the filtered signals can be used to unmix the original wide-band signals. Simulation studies might be valuable to determine which approach better estimates the low frequency dynamics. We found that both filtered and wide-band ICA approaches reliably separated the volume-conducted signal, which overlapped well with the neocortical signal recorded from several mm away in the frontal cortex. Across animals, we found that the same 5 components were reliably separated by ICA. These components were then putatively labelled based on their anatomical correspondence with the primary inputs to the dorsal hippocampus. To support these putative identities, we stimulated afferent pathways in a subset of animals and found activation exclusively in the expected components.

We next wanted to apply the ICA to important questions in hippocampal network dynamics during the slow oscillation. We found that subtraction of the volume-conducted component from the LFP revealed a phase reversal of 1 Hz (SO) activity within the hippocampus, suggesting local generation of this activity. This phase reversal was 100 μm below that of the theta phase reversal. We then optimized the BOSC method for oscillation detection (Caplan et al., 2001; Whitten et al., 2011; Hughes et al., 2012) in order to identify gamma-frequency activity in the

SLM*ic*, and to detect ripple oscillations in the pyramidal layer CSD that were associated with sharp waves in the SchC*ic*.

Another potential application of ICA for hippocampal signals is the removal of artifacts. In fact, one group has found that a component with a spatial profile resembling the volume conducted component also extracted the high frequency EMG artifacts from recordings during awake behaviour (Schomburg, 2014). It was mentioned that this component also had the largest < 5 Hz power during nonREM sleep, suggesting that it is in fact the same component that we have described as the VC*ic*. ICA may also be useful for removing other types of systematic artifacts that may contaminate local field potential recordings.

In summary we have shown that ICA is a powerful tool for analyzing the LFP in the hippocampus. Similar results are obtained across many different algorithms, but we found the best results with runica and FastICA (symmetrical, *tanh* or *gauss*). Pre-filtering to remove strong low-frequency oscillations such as theta is highly recommended. This approach can be used to remove the volume-conducted portion of the signal, or to assess oscillatory dynamics of separated components, which can be quantified using BOSC.

3 Separation and coordination of fast activity in localized hippocampal networks within and across large-amplitude rhythmic activity states: theta and the slow oscillation

Authors: Tara A. Whitten[1], and Clayton T. Dickson[1,2,3]

[1]Neuroscience and Mental Health Institute, University of Alberta, Edmonton, AB, Canada, T6G 2E1

[2]Department of Psychology, University of Alberta, Edmonton, AB, Canada, T6G 2H7

[3]Department of Physiology, University of Alberta, Edmonton, AB, Canada, T6G 2E9

Acknowledgments: This work was supported by a Natural Science and Engineering Council of Canada (NSERC) grant #249861 to CTD. TAW was additionally supported by an Izaak Walton Killam Memorial Graduate Scholarship, an Alberta Innovates – Technology Futures Graduate Scholarship and an NSERC Alexander Graham Bell Canada Graduate Scholarship – Doctoral (CGS D). We would like to acknowledge Trish Wolansky and Jon Kerber for contributing to data collection and Anastasia Greenberg for helpful comments on the manuscript.

3.1 Abstract

Hippocampal network activity supports many critical memory functions across both waking and sleeping states, from encoding and retrieval, to consolidation. Brain state-dependent changes in the interactions between local hippocampal circuits and their coordination with neocortical inputs and targets likely influence these memory-related processes. The hippocampus exhibits two distinct and mutually exclusive large-amplitude oscillatory activity patterns: theta (3-12 Hz) and the slow oscillation (SO; ~1 Hz). These patterns likely underlie different processing modes, which may be manifested through differential organization of faster frequency (> 8 Hz) operations that reflect activity in afferent inputs and local networks. In an attempt to understand these differences and their implications for the computational constraints imposed during theta and the SO, we partitioned laminar local field potential recordings in the CA1/dentate axis of the dorsal hippocampus of urethane anaesthetized rats using independent component analysis and compared the dynamics of input-specific activity across both states. We found that, similarly to theta, gamma-frequency inputs to the hippocampus during the SO are segregated as a function of phase. In addition, SO-specific fast activity patterns such as spindles and sharp-wave/ripples (SPW-Rs) are also modulated by SO phase. Interestingly, we found that SPW-R phase could vary as a function of SO power in the neocortex. This suggests a complex and dynamic interaction of hippocampal pathways with the neocortex during the SO. Phase- and state-dependent integration and segregation of information flow could provide a powerful mechanism for bidirectional cortico-hippocampal interactions that might support the consolidation of memory during slow wave sleep.

3.2 Introduction

Medial temporal lobe structures, including the hippocampus, have long been implicated in higher-order behavioural functions, including the encoding, retrieval and consolidation of explicit memories as well as spatial navigation and relational processing (Scoville and Milner, 1957; O'Keefe and Dostrovsky, 1971; Carr and Frank, 2012; Buzsaki and Moser, 2013; Eichenbaum and Cohen, 2014). While the anatomical organization of this region has been described since the time of Ramon y Cajal (1899), the functional connectivity and how the underlying neural networks support such a dynamic range of functions has remained elusive. A significant body of work has focussed on network activity during theta (3-12 Hz) oscillations, which are a prominent feature of hippocampal activity during awake exploratory behaviour as well as rapid-eye-movement (REM) sleep in both animals and humans (Bland, 1986; Buzsaki, 2002; Vertes et al., 2004; Lisman and Buzsaki, 2008; Tort et al., 2009; Axmacher et al., 2010; Pignatelli et al., 2012; Lisman and Jensen, 2013; Watrous et al., 2013; Jacobs, 2014). However, another form of large amplitude oscillatory activity, the ~1 Hz slow oscillation (SO) that synchronizes vast networks across the neocortex and hippocampus during the deepest stages of nonREM sleep, has been less well studied (Wolansky et al., 2006). The SO has been implicated in the process of sleep-dependent consolidation of hippocampal-dependent memories (Steriade et al., 1993b; Amzica and Steriade, 1997; Born, 2010), a process that likely involves a complex coordination between hippocampal and neocortical circuits. Therefore, an understanding of neocortical-hippocampal interactions during the SO, and how these interactions differ from those during theta oscillations, could provide critical information in understanding the mechanisms by which memory traces can be strengthened during sleep.

Both the SO and theta co-occur with gamma (20-100 Hz) oscillations in the hippocampus. In addition to gamma, spindles (8-16 Hz) and sharp-wave/ripple (SPW-Rs) are also modulated by the phase of the SO (Isomura et al., 2006; Wolansky et al., 2006; Peyrache et al., 2011). These faster rhythms can be generated by local hippocampal networks, or they can indicate rhythmic synaptic drive from oscillatory synchronization of upstream afferent networks. Within the CA1 subfield, two main sources of gamma-frequency synaptic inputs arrive from the entorhinal cortex (EC) and the CA3 subfield (Bragin et al., 1995). During theta oscillations, these two sources of gamma oscillations are active on different phases of the theta cycle (Colgin et al., 2009; Schomburg et al., 2014).

In the present study, we used urethane anaesthetized rats as a model for the spontaneous and alternating forebrain states that occur during natural sleep. This model mimics the electrographic patterns and their alternations occurring during REM and nonREM including theta and SO activity (Wolansky et al., 2006; Clement et al., 2008). We used independent component analysis (ICA) of multi-channel linear probe recordings across the CA1-dentate axis of the dorsal hippocampus to separate the activity of individual hippocampal pathways including the inputs from the EC and the CA3 subfield. Notably, we compared the coordination of faster (>8 Hz) oscillations in these pathways during both theta and SO. As shown previously, there was a segregation of pathway-specific inputs by theta phase (Schomburg et al., 2014), which we also demonstrated with respect to the SO. Specifically, we show that activity patterns are separated as a function of pathway, phase, and depth of the neocortical SO state. These findings extend our understanding of the functional coordination of individual hippocampal networks and highlight the differences in processing characteristics across different oscillatory brain states.

3.3 Methods

All experimental procedures conformed to the guidelines established by the Canadian Council on Animal Care and followed protocols that were approved by the University of Alberta Biosciences Animal Care and Use Committee.

3.3.1 Animals and surgery

Reported data were obtained from 17 male Sprague-Dawley rats weighing 250.7 ± 12.5g (all summary data are reported as mean ± standard error of the mean (SEM)). Animals were initially anaesthetized in a chamber with 4% isoflurane in 100% oxygen, followed by maintenance of anaesthesia via a nose cone delivering 1.5-2.5% isoflurane while a jugular catheter was inserted for subsequent urethane delivery. Urethane (0.67-0.8 g/mL) was administered intravenously in 0.03 mL increments to a final dose of 1.71 ± 0.06 g/kg over a period of ~30 minutes. Final urethane dosage was based on the attainment of a surgical plane of anaesthesia as assessed by a lack of withdrawal to toe pad pressure. Based on previous work, this intravenous dosage allowed for spontaneous alternations between activated and deactivated states as assessed electrographically (Wolansky et al., 2006; Clement et al., 2008). Animals were then transferred to a stereotaxic frame (Model 900; David Kopf Instruments, Tujunga, CA), and body temperature was maintained at 37°C using a servo-driven heating pad connected to a rectal probe (TR-100; Fine Science Tools, Vancouver, BC, Canada). Atropine methyl nitrate (0.05 mg/kg) was administered subcutaneously to prevent respiratory secretions. Supplemental urethane doses (0.01 mL) were administered if at any point animals showed spontaneous vibrissae movement or a reflex withdrawal to a hindpaw pinch. A monopolar electrode (Teflon-coated stainless steel wire, bare diameter: 125 µm; A-M Systems, Carlsborg, WA) was implanted in the frontal cortex (all coordinates relative to Bregma: anterior-posterior (AP): +2.5 mm; medial-lateral (ML): +1.2 mm), in either the superficial (n=10, dorso-ventral (DV): -0.23 ± 0.01 mm) or deep (n=6, DV -1.73 ± 0.07 mm) cortical layers. For comparisons across subjects, superficial recordings were reversed so that negative polarity represented an UP-state and positive polarity represented a DOWN-state for all subjects. A 16-channel linear multi-site electrode with 100 μm contact separation (silicon probes from Neuronexus, Ann Arbor, Michigan, or multi-site platinum-iridium electrodes from Plexon, Dallas, Texas) was implanted in the dorsal hippocampus, spanning an axis from the stratum oriens (SOr) of CA1 to the stratum moleculare (SMol) of the dentate gyrus (DG) at the deepest contact (AP -3.31 ± 0.03 mm; ML -2.27 ± 0.06 mm; DV -3.51 ± 0.07 mm). In some cases additional recordings were made at more superficial or deeper positions; however, grand averages were computed on the depth span as reported above. In a subset of experiments, bipolar stimulating electrodes (twisted Teflon-coated wires, bare diameter 200 μm, A-M Systems, Carlsborg, WA) were implanted in the contralateral CA3 (n=2, AP -3.8 mm; ML -3.75 mm; DV -2.68 ± 0.38 mm) and/or in the ipsilateral angular bundle (n=6, AP -7.05 ± 0.12 mm; ML -4.08 ± 0.42 mm; DV -3.12 ± 0.33 mm). All non-moving electrodes were fixed in place to the skull using dental acrylic.

3.3.2 Data Collection

All recordings were referenced to stereotaxic ground. Monopolar electrode signals were amplified at a gain of 1000 and filtered between 0.1 Hz and 10 kHz using a differential AC amplifier (Model 1700, A-M Systems) while linear multiprobe signals were first passed through a headstage with unity gain (Plexon, Dallas, Texas) and then amplified at a gain of 1000 and filtered between 0.07 Hz and 8 kHz (PBX-2 amplifier, Plexon). All signals were then digitized at a sampling rate of 1000 Hz with anti-alias filtering at 500 Hz using a 1322 Digidata A/D board (Molecular Devices, Union City, CA) connected to a PC computer for data acquisition in Axoscope 9.0 (Molecular Devices, Union City, CA). Evoked potentials were elicited in CA1 through delivery of biphasic stimulating pulses through bipolar stimulating electrodes connected to an isolated constant current pulse generator (Model 2100, A-M Systems). Parameters for stimulation of the angular bundle were 100-250 μA for 0.2-0.5 ms; parameters for stimulation of the contralateral CA3 were 100-150 μA for 0.2-0.5 ms.

Following the acquisition of electrophysiological recordings, animals were transcardially perfused with physiological saline, followed by 4% paraformaldehyde, and brains were extracted and stored in a solution of 4% paraformaldehyde and 30% sucrose for subsequent histological processing. After a minimum of 24 hours, tissue was frozen with compressed CO_2 and sliced at a thickness of 48 μm using a rotary microtome (Model 1320, Leica, Vienna, Austria). Slices were then mounted on gel-coated slides, allowed to dry, stained with thionin and cover-slipped. For each experiment, the position of the multiprobe within the dorsal hippocampus was verified. Only track profiles spanning the CA1-dentate axis were included in the subsequent analysis.

3.3.3 Data Analysis

Unless otherwise stated, all reported “n” refer to number of animals. Analysis was performed using a combination of built-in and custom-written code in Matlab version 7.14 (The Mathworks, Natick, MA).

The **B**etter **Osc**illation detection (BOSC) method was used to identify oscillatory events. The details of this method have been described previously (Chapter 2; Caplan et al., 2001; Whitten et al., 2011; Hughes et al., 2012). Briefly, a continuous wavelet transform was performed using a Morlet wavelet of width 6 with 37 $\log_2$-spaced scales with pseudo-frequencies from 0.5 Hz to 256 Hz (or 20 $\log_2$-spaced scales from 8 - 215 Hz for band-pass filtered signals). The background spectrum was calculated as the average spectrum in a 36-second sliding window centered on the time point of interest. The background spectra were fit with a 2nd degree polynomial in log-log space. We found that this modification to the original BOSC method (which used a linear fit of the background spectrum) improved the fit to more accurately represent data, especially at lower and higher frequency bandwidths (see Chapter 2). To reduce the computational load of fitting the background spectrum at each time point, a sliding window was used with 6 second steps and intermediate values for the fit were calculated by interpolation. A power threshold was set as the 99th percentile of the theoretical $\chi^2(2)$ distribution of power values at each frequency (the 99.99th percentile was used for detection of ripples). A duration threshold was set as 3 cycles (5 cycles for detection of ripples which are 5-15 cycles in duration (Chrobak and Buzsaki, 1996)). Oscillations were detected only when both the power and duration thresholds were exceeded. The duration threshold of 3 cycles was selected based on previous work (Caplan et al., 2001; cf. Figure 6), but the robustness of our findings to longer duration thresholds of 4 and 5 cycles was also assessed. While fewer oscillations were detected with longer thresholds, the results with respect to phase modulation of gamma activity were not significantly different, and in some cases too few oscillations were detected with a 5-cycle threshold to assess phase modulation. Therefore 3 cycles was determined to be the optimal duration threshold. Finally, a measure termed P-episode was defined as the proportion of time during which oscillations at a given frequency or within a frequency band were detected (Caplan et al., 2001).

For each experiment, data were separated into activated (SO) and deactivated (theta) states based on the BOSC detection of theta (3-5 Hz) oscillations in the local field potential (LFP) at stratum lacunosum moleculare (SLM). Using a sliding 10 second window, epochs with a theta P-episode of greater than 0.9 were classified as activated (theta) states, while epochs with a theta P-episode of less than 0.1 were classified as deactivated (SO) states. On average 4.7 ± 0.6 minutes were classified as SO, 4.5 ± 1.2 minutes were classified as theta, and 4.2 ± 0.6 minutes were classified as transition states and were not analyzed (n=16). Power spectra as well as power, phase and coherence profiles of within-state SO and theta activity were constructed using Welch's averaged periodogram method with a 6-second Hanning window and 2 second overlap with SLM as the reference channel. Profiles for gamma activity were also constructed using a 200 ms Hanning window with a 67 ms overlap, using channels in SOr, stratum radiatum (SRad), SLM or SMol as references. Filtering of signals was performed using a zero-phase-lag (forward and backward) 3rd order Butterworth filter. Current source density (CSD) was computed on multiprobe signals by estimating the 2nd spatial derivative (units mV/mm^2) of the voltage traces, using a 3-point difference ($CSD = -[f(p_{i-1}) - 2f(p_i) + f(p_{i+1})]/d^2$, where $f(p_i)$ is the field signal from probe channel i (i=2,3,. . .,15), and d is the distance between adjacent channels (Freeman and Nicholson, 1975; Mitzdorf, 1985; Rodriguez and Haberly, 1989; Ketchum and Haberly, 1993). For channels at the end of each probe, the derivative was estimated using only the adjacent channel (forward or backward differential). We have previously confirmed that this method produces equivalent results (Wolansky et al., 2006; Nazer and Dickson, 2009). While the end-channel CSD estimates calculated in this way are less reliable, these end-channels were only used for graphical representations and not for any analyses.

Frequency co-modulograms were computed using a modified version of the modulation index (MI; Canolty et al., 2006; Kramer et al., 2008; Tort et al., 2010). For each pair of frequencies, the phase of the lower frequency and the amplitude of the higher frequency were computed using the angle (phase) and absolute value (amplitude) of the respective wavelet transforms. The amplitude values were then assigned to 72 evenly spaced phase bins, and the deviation of this distribution from a uniform distribution (no modulation) was calculated using a modification of the Kullback-Leibler distance as described in Tort et al. (2010).

Independent Component Analysis (ICA) was computed on both raw and filtered (30 Hz low pass or 6-250 Hz band pass) continuous signals including both theta and the SO (range 5.66 – 29.76 minutes, mean 14.04 ± 1.48 minutes, n=16) using the runica algorithm (Makeig et al., 1996; Delorme and Makeig, 2004). Comparisons were made to ICA results from multiple algorithms, including FastICA (Hyvarinen and Oja, 2000; http://www.cis.hut.fi/projects/ica/fastica/) and JadeR (Cardoso, 1999) and results were comparable across all ICA implementations (see Chapter 2). Pre-processing steps included dimension reduction to 6 components using Principal Components Analysis (PCA) to reduce noise and to improve the convergence of the ICA algorithm (Hyvarinen and Oja, 2000; Martin-Vazquez et al., 2013; Schomburg et al., 2014). In cases where one or more of the 6 components were clearly artifacts (based on a highly irregular spatial weights or time series), the PCA dimension reduction was adjusted by the number of artefactual components to allow for the extraction of relevant components with physiologically meaningful time series and spatial profiles (raw and low-pass filtered: n=3/16, mean 2 ± 1 artifact components; band-pass filtered: n=1/16, 1 artifact component). The number of components retained was based on the number of components with consistent spatial loadings across subjects (see Chapter 2), and accounted for 99.5 ± 0.1% of the total variance of the signals. The details of the ICA algorithm have been described elsewhere (Bell and Sejnowski, 1995; Makeig et al., 1996; Hyvarinen and Oja, 2000; Delorme and Makeig, 2004). Briefly, the multi-channel LFP signal ($\mathbf{x}$) was assumed to be a linear mixture of underlying neural sources ($\mathbf{s}$), so that $\mathbf{x} = A\mathbf{s}$ (with A as the mixing matrix). The approach is to estimate both A and $\mathbf{s}$ knowing only $\mathbf{x}$ by using the assumption that the sources ($\mathbf{s}$) are statistically independent (Hyvarinen and Oja, 2000). In the context of decomposing the LFP from a linear multiprobe array, the mixing matrix A provides the spatial profile of the weighting of each component at each electrode. The inverse of the mixing matrix, A^{-1}, allows the transformation from the mixed signal to the underlying sources ($A^{-1}\mathbf{x} = \mathbf{s}$). Both A and $\mathbf{s}$ are unitless but units of millivolts are recovered when they are multiplied to obtain the contribution of each underlying source to the LFP at each electrode. ICA is an example of blind source separation, and the runica algorithm finds maximally independent sources using an unsupervised learning rule that maximizes the joint entropy of the output (which is theoretically similar to minimizing the mutual information). ICA is distinct from PCA in that it maximizes the statistical independence instead of maximizing the described variance, and it does not require that components be orthogonal. Whereas PCA is optimally applied when the distribution of underlying sources is Gaussian, ICA is optimal when sources are non-Gaussian, as is the case for neural data (Buzsaki and Mizuseki, 2014). The ICA approach has previously been applied with excellent success on hippocampal LFP signals to extract multiple underlying sources or generators corresponding to known physiological pathways (Makarov et al., 2010; Makarova et al., 2011; Fernandez-Ruiz et al., 2012b; Fernandez-Ruiz et al., 2012a; Fernandez-Ruiz and Herreras, 2013; Fernandez-Ruiz et al., 2013; Martin-Vazquez et al., 2013; Schomburg et al., 2014). It should be noted that while ICA algorithms provide results that are not deterministic, the empirically determined variability in components extracted across repeated implementations of ICA on the same dataset was extremely low (see Chapter 2).

In order to compare the ICA components across experiments, a method was developed to normalize the spatial profiles based on known physiological landmarks. Depth measurements were shifted relative to the phase-reversal of theta activity (arbitrarily denoted as 0 μm; see Figure 3.1), and the entire profile was scaled so that the peak of the theta power profile (~ SLM/hippocampal fissure; see Figure 3.1) occurred at -400 μm, which was the modal depth prior to scaling. To construct average profiles, cubic spline-interpolation was performed to obtain weight values at 100 μm intervals relative to the theta reversal. In addition, the component weightings were scaled by the maximum weighting value for each subject. The components were found to be highly consistent across subjects, with spatial profiles that corresponded to expected profiles for known physiological pathways (Figure 3.1A). Components were classified based on several criteria, including the depth of maximal activation and the depth of any polarity reversals in the component weights as well as spectral characteristics of each component during SO and theta samples. The identities of the ICA components were further evaluated by stimulation of known pathways to CA1/DG including the contralateral CA3 to activate the commissural Schaffer collateral (SchC) pathway and/or the angular bundle to activate the medial (MPP), lateral (LPP) perforant pathways as well as the temporoammonic (TA) pathways. The inverse of the mixing matrix obtained from the ICA of the spontaneous LFP signals was multiplied by the average evoked potential signal ($A_{spont}^{-1}\mathbf{x}_{\mathbf{stim}} = \mathbf{s}_{\mathbf{stim}}$). In all cases the evoked potential was primarily captured in the time course of one or two independent components, and this was taken as an additional piece of evidence supporting the identity of that component.

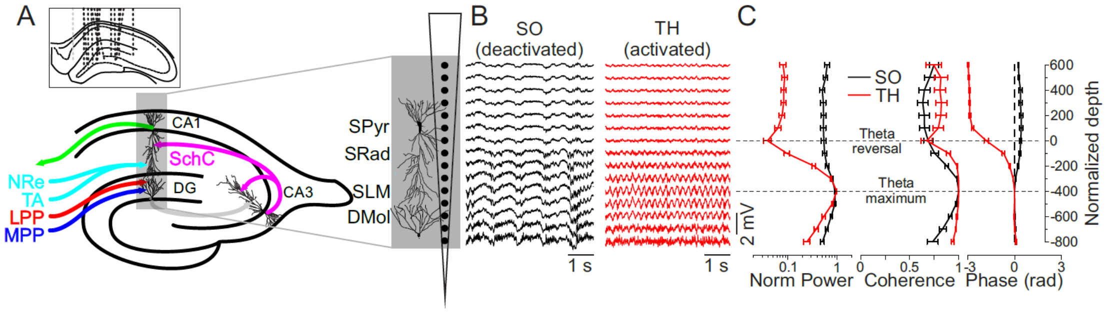

Figure 3.1 Depth profiles provide laminar landmarks within the dorsal hippocampus.

(A) Left panel shows a representation of the dorsal hippocampus, including the major afferent pathways from the EC including the medial (MPP, blue) and lateral (LPP, red) perforant pathways as well as the temporoammonic (TA, cyan) pathway, in addition to the ipsilateral afferent from CA3, the Schaffer collateral (SchC, magenta) pathway. Inset shows multiprobe position for individual subjects. Data from subject shown in grey was not used due to medial position. Right panel shows an expansion of the CA1/DG axis and the locations of the multiprobe contact sites for a representative subject. (B) Representative LFP recordings of the slow oscillation (SO) during the deactivated state (black, left panel) and theta oscillations during the activated state (red, right panel) under urethane anaesthesia. (C) Average normalized power (left), coherence (middle), and phase (right) profiles of SO and theta activity as a function of depth, with the channel of maximal theta power taken to be SLM and used as the reference channel. Data represent mean ± SEM for all subjects (n=16), with depth normalized based on the reversal of theta activity (normalized depth = 0) and the maximal theta power (normalized depth = -400 μm). More details on depth normalization are available in the Methods section.

Once the putative identities of the ICA components were determined, the relationship of activity within each component with respect to either the neocortical SO or the hippocampal (SLM) theta signals was assessed. Because activity in the pyramidal cell layer was not well separated by ICA, the raw LFP at Stratum Pyramidale (SPyr) was used to assess activity at this layer. For each component and each frequency band (spindles: 8-16 Hz; gamma: 20-100 Hz; ripples: 100-200 Hz), the distribution of detected oscillations relative to the neocortical SO or relative to the SLM theta phase were calculated with bin widths that scaled with the oscillation period length. The reported peak frequency within each band was the frequency with the maximum P-episode (proportion of time with detected oscillations) that occurred during that epoch. The mean angle and mean resultant length for the phase amplitude relationships were calculated using the CircStat Matlab toolbox for circular statistics (Berens, 2009) for each frequency band. Second-order circular statistics were then used to calculate the mean angle and resultant length across experiments within each frequency band for both SO and theta. Due to the saw-toothed shape of the theta oscillation and the resulting non-uniform phase distribution, spurious co-modulation can be detected in the absence of true cross-frequency coupling (Siapas et al., 2005). We therefore used a randomization procedure to confirm the phase-modulation findings for theta. We performed 200 random permutations of the oscillation detection time series for each subject. Results reported are based on the critical F-value from the F-distribution, but in all cases significant co-modulations reported also exceeded the 95th percentile of F-statistics computed from the randomized oscillation detection time series. Other groups have also found no difference in phase-modulation results using Hilbert phase compared to waveform-based phase estimation methods (Schomburg et al., 2014). The Hotelling test for paired angles (Zar, 2010) was used for determining the significance of differences between mean angles.

Based on the continuous BOSC detections in each frequency band, the discrete time points and counts of oscillatory events were defined by finding the start and end points of each detection, and merging detections that were separated by less than 30 ms. These event times were then used for calculating triggered averages and for evaluating the number of SO or theta cycles on which events in each component and frequency band were detected. Relationships between the occurrences of different events were evaluated by creating 2x2 contingency tables and evaluating the χ^2 statistic.

3.4 Results

In all cases, urethane-anaesthetized animals cycled rhythmically between an activated state during which hippocampal theta oscillations were prominent, and a deactivated state characterized by the neocortical and hippocampal SO (n=16, Figure 3.1; Figure 3.2A-C). The data from one subject were removed following histological assessment of electrode placement that was too medial and did not span the CA1/dentate axis (Figure 3.1A, inset). Within the hippocampus, the power of both theta and the SO are maximal at SLM (Figure 3.1C). We separated hippocampal recordings into activated and deactivated states to assess the relationship between high frequency (> 8 Hz) oscillations within the hippocampus to the ongoing slower (SO and theta) rhythms. For comparisons across subjects, values were normalized based on the depth of the theta reversal and the depth of the theta maximum (Figure 3.1C).

3.4.1 Cross-frequency coupling varies with state and depth

CSD analysis of hippocampal activity during the SO and during theta revealed sinks at both SLM and SRad, which likely correspond to the inputs from the EC and

CA3 respectively (Figure 3.2D). These sinks both showed rhythmic bursts of high-frequency activity (Figure 3.2E). Interestingly, the relative strength of the sinks at both layers changed dynamically across the evolution of the deactivated state (compare left and middle panels in Figure 3.2C-E).

The relationship and phase-modulation of high-frequency synaptic inputs to the theta oscillation has been well studied (Bragin et al., 1995; Colgin et al., 2009; Schomburg et al., 2014). In order to better characterize the relationship between these high-frequency bursts and the neocortical SO, cross-frequency coupling of hippocampal activity during the SO was compared to cross-frequency coupling during theta. In addition, we compared these phase patterns with neocortical cross-frequency coupling during the SO (Figure 3.3). To systematically examine all possible cross-frequency relationships, amplitude-phase frequency co-modulograms were constructed (Figure 3.3B, E and H). Consistent with previous findings (Greenberg and Dickson, 2013), there was a strong modulation of both slow (15-30 Hz) and fast (50-100 Hz) gamma to ~1 Hz SO frequency in the neocortex during the SO, as seen in the raw and filtered traces (Figure 3.3A), in the phase-amplitude comodulograms (Figure 3.3B) and distributions for single frequencies (Figure 3.3C) . Note that in recordings from the deep layers of the cortex, negative polarity in the LFP corresponds to the active (ON/UP) phase, while positive polarity corresponds to the silent (OFF/DOWN) phase of the SO (Steriade et al., 1993b; Amzica and Steriade, 1995a). In the hippocampus, the CSD of the raw signals was used to examine local cross-frequency coupling. During theta, there was a strong modulation of the slow gamma (25-50 Hz) amplitude to the SLM theta phase (Figure 3.3D-F). A similar relationship was also observed during the SO, where there was also a strong modulation of slow gamma (25-50 Hz) amplitude to the SLM SO phase, in addition to an SO-modulation of spindle (8-16 Hz) amplitude (Figure 3.3G-H).

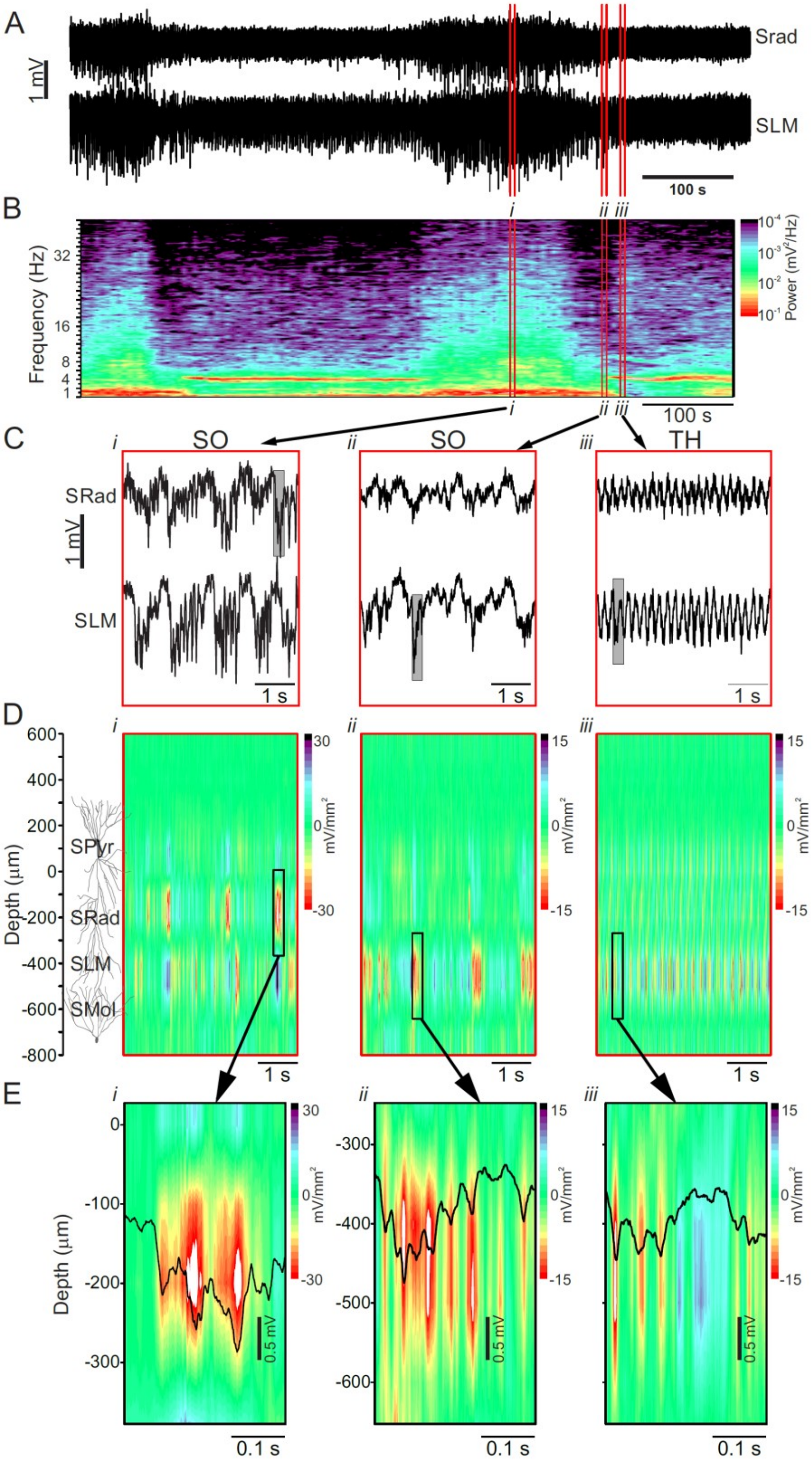

Figure 3.2 CSD analysis reveals bursts of high frequency activity at different depths that are modulated across spontaneous changes in state.

Figure 3.2 CSD analysis reveals bursts of high frequency activity at different depths that are modulated across spontaneous changes in state.

(A) Representative LFP traces from SRad and SLM showing regular alternations between deactivated (large amplitude) and activated (lower amplitude) states. (B) Spectrogram of the SLM trace showing high power at ~1 Hz during the deactivated (slow oscillation) state and high power at ~4 Hz during the activated (theta) state. (C) Expansions of highlighted segments (red bars) from (A), showing the changes in large-amplitude rhythmic activity patterns as a function of state (SO – *i* and *ii*; theta – *iii*). (D) CSD of time segments from C (SO – *i* and *ii*; theta – *iii*). Depth measures refer to normalized distances as described in the Methods section and in Figure 3.1. (E) Expansions of boxed areas from C (raw trace) and D (CSD), highlighting that SO- and theta- related sinks are comprised of bursts of higher-frequency activity (SO – *i* and *ii*; theta – *iii*).

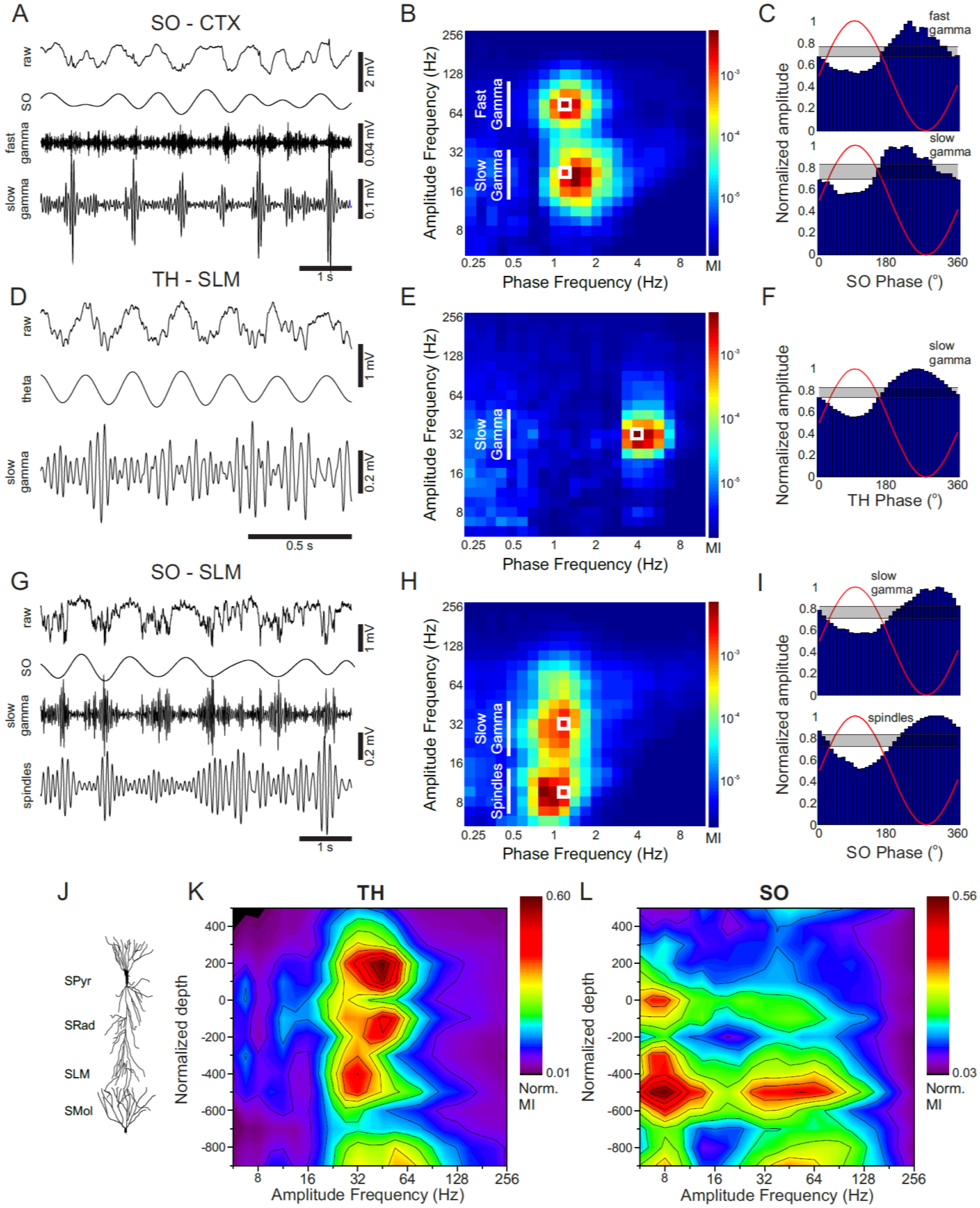

Figure 3.3 Cross-frequency (phase-amplitude) coupling varies with state and depth.

Figure 3.3 Cross-frequency (phase-amplitude) coupling varies with state and depth.

(A) Raw and filtered traces for a representative subject highlighting the modulation of the amplitude of fast (50-100 Hz) and slow (15-30 Hz) gamma oscillations by the phase of the neocortical SO. (B) Phase-amplitude co-modulation in the neocortex during the SO for a representative subject, using the modulation index (MI; see methods section). Both slow- and fast- gamma amplitudes are related to the phase of the ~1 Hz SO. (C) Distribution of gamma amplitude as a function of SO phase for both slow and fast gamma using the phase and amplitude frequencies from white boxes shown in (B). Shaded areas indicate the 95th percent confidence intervals for expected gamma amplitude given no phase modulation based on a randomization procedure using 200 surrogate amplitude time series. (D-F) Analysis of phase-amplitude coupling during theta oscillations recorded at SLM in the hippocampus for the same subject using CSD signals. Note the strong modulation of gamma frequency activity in the slow range (25-50 Hz) by the ~4 Hz theta oscillation. (G-I) Analysis of phase-amplitude coupling during the SO recorded at SLM for the same subject using CSD signals. Note the strong modulation of both spindle (8-16 Hz) and slow gamma (25-50 Hz) activities by the phase of the ~1 Hz SO. (J) Schematic representation of the layers within the dorsal hippocampus corresponding to the normalized depths in panels K and L. (K) Amplitude modulation of the CSD signals by the theta phase as a function of depth across subjects (n=16; in contrast to panels B, E and H, the amplitude frequency is now on the x-axis, with a single phase frequency and depth represented on the y-axis). For each subject, MI values were normalized to range from 0 to 1. MI values were then interpolated based on the depth normalization procedure in order to create a grand average. Note the three peaks in gamma modulation by theta phase: one spanning SLM and the hippocampal fissure, one near SRad and one near SPyr. (L) Modulation of CSD amplitude by the SO phase as a function of depth. Note the strong modulation of spindle and gamma frequencies near SLM and the hippocampal fissure, and an additional spindle peak and weak gamma peak just below SPyr.

The above relationships were assessed at a single depth corresponding to SLM. In order to characterize changes in modulation across depth, the modulation index for a single phase frequency (corresponding to the peak SO or theta frequency) was plotted as a function of depth and normalized across subjects (Figure 3.3J-L). In order to provide a common reference signal for phase for this and all subsequent analyses, the neocortical signal was selected as the reference SO signal due to its highly coherent nature across neocortical sites (Amzica and Steriade, 1995a, b; Greenberg and Dickson, 2013) while SLM, where theta power is maximal, was used as the reference theta signal. This revealed multiple sites at which cross-frequency coupling took place. Slow (20-60 Hz) gamma was modulated by theta at SLM/ hippocampal fissure, at SRad and at SPyr, while gamma spanning the slow and fast ranges (20-100 Hz) as well as spindle activity were modulated by the SO at input layers corresponding to the termination zones of the TA and perforant pathways (SLM and SMol of the DG). This suggests layer-specific modulation of fast activity during both theta and the SO, which could reflect how information is processed within the hippocampal circuit during both activity states.

3.4.2 ICA separates individual hippocampal pathways

In the CSD analyses of raw traces (Figure 3.2D-E) and in the frequency co-modulograms as a function of depth (Figure 3.3J-L), it was difficult to differentiate between active and passive sinks and sources in order to correlate activity at a given depth with a particular synaptic input. To overcome this ambiguity, we used ICA to separate the underlying inputs from the mixed LFP signal (see Methods section; Makarov et al., 2010; Makarova et al., 2011; Fernandez-Ruiz and Herreras, 2013; Schomburg et al., 2014). This approach is summarized in Figures 4 and 5. The spatial profiles of the component weightings were examined, including the depth of maximal activation and the depth where any polarity reversal occurred, and these were compared to the known anatomy and expected profiles of the circumscribed hippocampal pathways (representative example: Figure 3.4A-B; group summary: Figure 3.5A-B). Based on this, six components were putatively identified. The volume conducted component (VC*ic*) was the only one to show a lack of polarity reversal across depth, and tended to show a monotonically decreasing spatial weight as would be expected from a signal that was not generated locally but instead volume-conducted from the overlying cortex (Figure 3.4B and 5B, black). The SchC component (SchC*ic*) was characterized by a peak near -200 µm in normalized depth (corresponding to SRad) and a reversal within CA1 (Figure 3.4B and 5B, magenta). A third component was characterized by a peak near -400 µm in normalized depth (corresponding to SLM) and a reversal within CA1 (dorsal to SLM; Figure 3.4B and 5B, cyan), and could potentially reflect a mixture of TA inputs from both medial and lateral EC layer III, with relative contributions varying depending on electrode position in the proximo-distal axis (Steward, 1976). In addition, there could be a contribution of inputs to this lamina from the nucleus reuniens of the thalamus (Wouterlood et al., 1990; Dolleman-Van der Weel et al., 1997; Vertes, 2015). Despite these ambiguities, this activity was separated by the ICA as a single component and was labelled the SLM*ic*. In contrast to the SchC*ic* and SLM*ic* that both reversed polarity within CA1, the MPP and LPP components (MPP*ic* and LPP*ic*; Figure 3.4B and 5B blue and red) had reversals at or below the hippocampal fissure. The MPP*ic* polarity reversal was more ventral than that of the LPP*ic*. Due to recordings that centered on the CA1 subfield and the limited span of 16 electrodes with 100 µm spacing, the MPP*ic* was only apparent in 13/16 subjects. Finally, in some cases the ICA extracted a component with a depth profile that peaked in the CA1 pyramidal cell layer (Figure 3.4B, green). However, this component was not reliably separated by the ICA across animals, possibly due to the small amount of

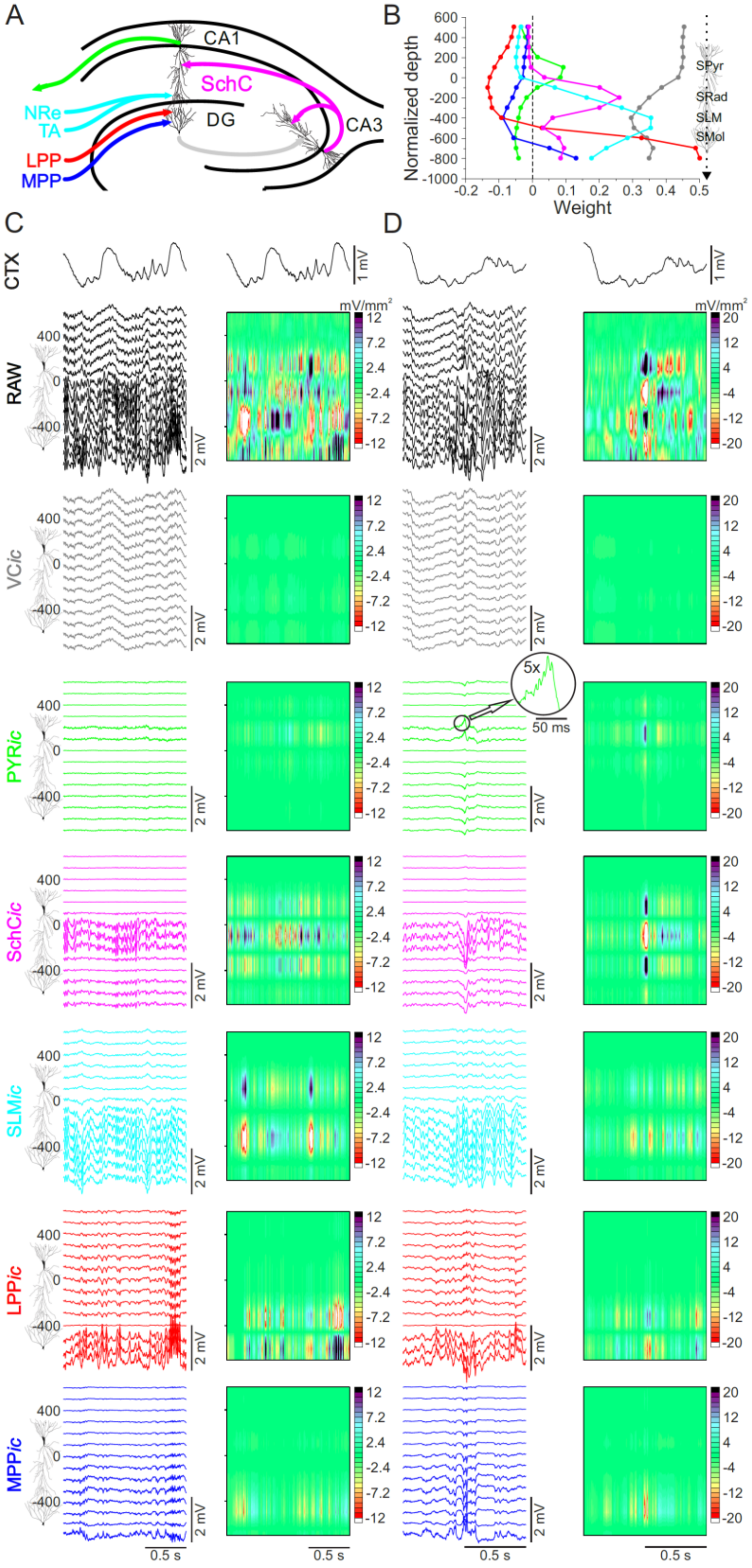

Figure 3.4 Separation of pathway-specific activity patterns in the dorsal hippocampus by ICA.

Figure 3.4 Separation of pathway-specific activity patterns in the dorsal hippocampus by ICA.

(A) Schematic diagram of the dorsal hippocampus including the major afferent pathways to CA1 and the DG. (B) ICA weights for a single representative subject. (C) LFP (left) and CSD (right) representing ~ 2 seconds of spontaneous activity during the SO showing raw (black) and ICA-separated component time courses. Neocortical signal is shown at the top for reference. Note the similarity in shape of the VC*ic* traces to the neocortical signal and the lack of sinks and sources. Also note the spatially localized activity attributed to each individual component. (D) As in panel C for a time segment that includes a SPW-R. Note the strong sink in the CSD of the SchC*ic* with a corresponding ripple-frequency source in the PYR*ic*.

the total variance in the signal contributed by activity at SPyr. We therefore used the CSD signal at SPyr (PYR_{CSD}) instead of the PYR*ic* to assess activity at this layer.

The time courses of individual components for a representative animal are shown during ~ 2 seconds of ongoing activity during the SO (Figure 3.4C) and ~ 1 second of activity during a SPW-R (Figure 3.4D) with the raw LFP and CSD as a reference. It is clear from both the extracted LFP traces (left panels) and the resultant CSD analysis (right panels) that the ICA is successfully extracting activity from individual sources that would be otherwise mixed in the raw signals. Further analysis of activity patterns in the time series of separated components supported their established putative identities. For example, the VC*ic* was highly similar to the frontal neocortical signal (Figure 3.4C-D, CTX (top panel) vs VC*ic* (grey)), and contributed substantially to the LFP recorded at superficial, but not deeper layers in the hippocampus (Figure 3.4: VC*ic* (grey) is similar to the RAW (black) signal at superficial but not deep channels). Furthermore, the VC*ic* showed minimal activity in the CSD plots (Figure 3.4), suggesting, as expected, that this activity is not generated locally in the hippocampus (see Chapter 2). Inspection of the time course and CSD of the SLM*ic* showed a strong relationship between activity in the SLM*ic* and UP-states (negative polarity) in the cortex (Figure 3.4C, cyan)). During identified SPW-Rs, the SchC*ic* time series showed clear evidence of sharp wave events (Figure 3.4D, magenta), while the PYR*ic* time series (when it was successfully separated) captured the corresponding ripple oscillation (Figure 3.4D, green; see inset).

One assumption necessary for the interpretation of the ICA results is the temporal, spectral and spatial stability of the separated components. In order to test this, the ICA results from the wide-band full time series were compared to those obtained from SO- or theta-specific epochs (Figure 3.5C and E) and to those obtained from filtered signals (< 30 Hz or 6 - 250 Hz; Figure 3.5D and F). Both the component weightings and the component time series were highly similar in all cases. In addition, the similarity of component weightings was assessed for recordings taken at different depths, separated in time (i.e. recordings taken sequentially), and the overlap was striking (Figure 3.5G). Nevertheless, we found less inter-subject variability in phase-modulation results when pre-filtering (6-250 Hz) was performed (as in Figure 3.5, right panel), so all subsequent analyses of high-frequency (>8 Hz) activity are based on ICA results from band-pass filtered signals (see Chapter 2).

Another piece of evidence used for component identification was based on the stimulation of known afferent pathways in a subset of animals to obtain average evoked potential profiles. The inverse of the ICA mixing matrix from spontaneous (i.e. stimulation-free) recordings was projected onto this evoked potential to see how well the putative pathway component captured the profile data (Figure 3.5H-I). This approach successfully separated the activation of the SchC*ic* following CA3 stimulation (Figure 3.5H; latency 11.3 ± 2.1 ms; n=2) from the activation of the rhinal inputs following stimulation of the angular bundle (Figure 3.4I, n=6: SLM*ic* latency 7.7 ms, n=1; LPP*ic* latency 7.1 ± 0.6 ms, n=3; MPP latency 6.5 ± 1.6 ms, n=3). In one subject, both the MPP*ic* and LPP*ic* were activated, with the LPP*ic* sink following the MPP*ic* sink by 0.9 ms (Figure 3.5I, right panel). In addition, stimulation of the angular bundle to activate the rhinal inputs led to a delayed sink in the SchC*ic* in 3/5 subjects at an average latency of 14.7 ± 0.5 ms, suggesting the activation of the trisynaptic loop (data not shown). The activity in the SchC*ic* following CA3 stimulation had a nearly identical profile to the raw and SchC*ic*- separated activity during a SPW-R (CSD plots, Figure 3.5H). There was occasionally some activation of the VC*ic* following stimulation of either CA3 or the angular bundle (Figure 3.5H-I, black traces). This could either reflect true volume conduction of an evoked potential

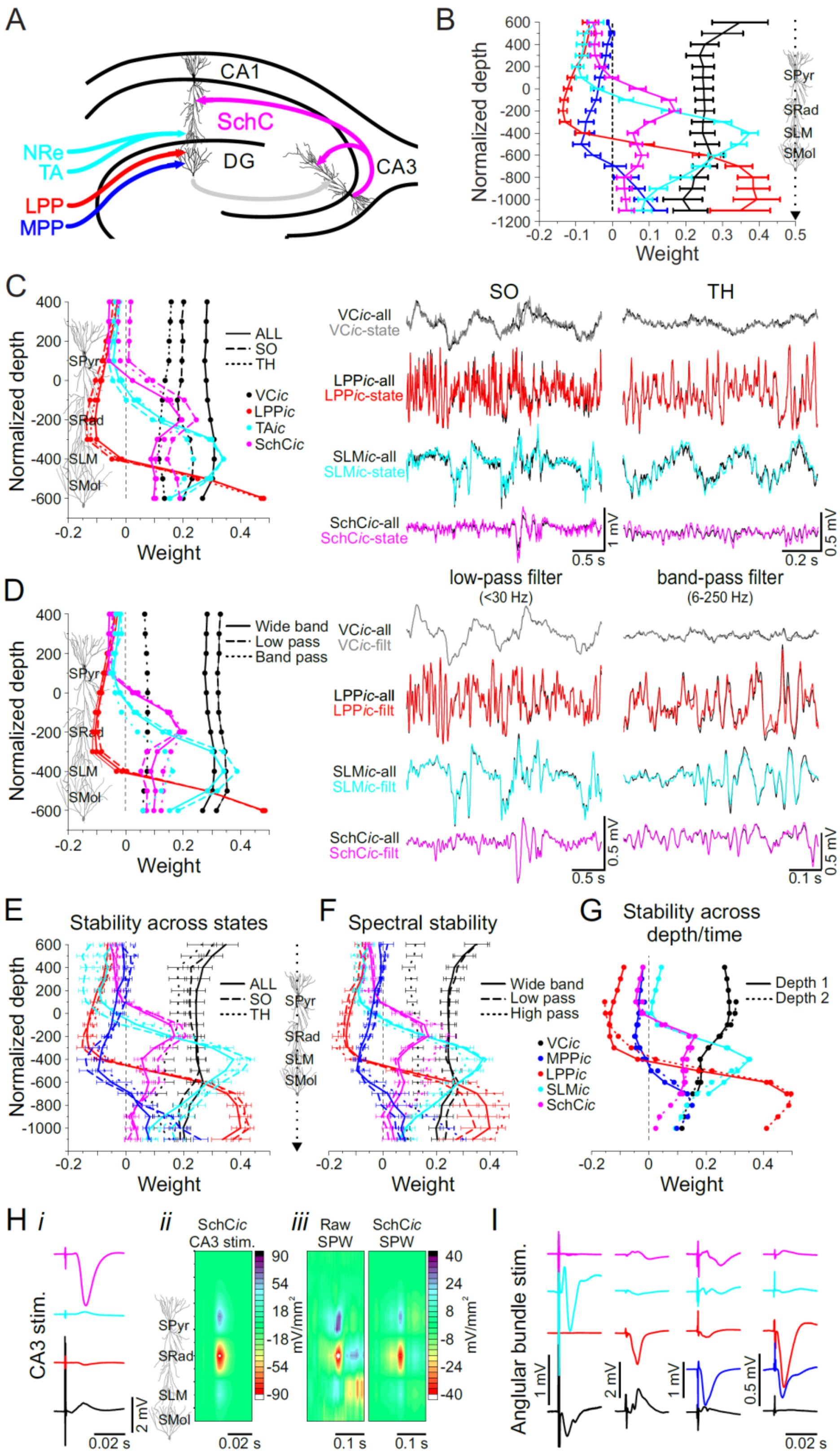

Figure 3.5 Assessment of ICA component specificity and stability

Figure 3.5 Assessment of ICA component specificity and stability.

(A) Schematic diagram of the dorsal hippocampus including the major afferent pathways to CA1 and the DG. (B) Mean weights for ICA components across experiments. Colour coding corresponds to colours used in panel A and is consistent throughout this and all subsequent figures: blue – MPP*ic* (n=11); red – LPP*ic* (n=16); cyan – SLM*ic* (n=16); magenta – SchC*ic* (n=16); black – VC*ic* (n=16). (C) Comparison of spatial loadings (left) and component time series (right) for ICA using different epochs (ALL data vs SO- or theta- only) for a single animal. (D) Comparison of spatial loadings (left) and component time series (right) for ICA using different pre-filtering parameters (wide-band vs 30 Hz low pass vs 6-250 Hz band pass) for the same subject as in (C). (E) Group data for analysis shown in (C). (F) Group data for analysis shown in (D). (G) Comparison of spatial loadings for ICA decomposition of recordings taken at different depths in the same animal, with recordings separated by ~30 minutes. (H) Stimulation of CA3 activates the SchC*ic*. (*i)* Time course of activation of each component during the evoked potential, obtained by using the inverse of the mixing matrix from the spontaneous data ($A_{spont}^{-1}\mathbf{x}_{\mathbf{stim}} = \mathbf{s}_{\mathbf{stim}}$; see Methods section for more detail). Amplitude expressed in mV at the depth of maximal negativity of the raw evoked potential. The evoked potential is clearly captured in the time course of the SchC*ic* (magenta) with minimal activation of the other components, as expected if the SchC*ic* represents the activity of the SchC pathway. (*ii*) Stimulation-evoked CSD for the SchC*ic*, showing a large sink at SRad. (*iii*) CSD of raw signal (left) and SchC*ic* (right) during an identified SPW-R. Note similarity to the SchC*ic* CA3 stimulation CSD. (I) Stimulation of the angular bundle activates primarily the SLM*ic* (cyan), the LPP*ic* (red) and/or the MPP*ic* (blue).

outside the recording area or alternatively it could reflect the imperfect separation of sources by the ICA.

3.4.3 Pathway-specific components show distinct spectral and cross-frequency coupling properties

Spectral and phase-amplitude cross-frequency coupling analysis of individual components revealed consistent characteristics across subjects (Figure 3.6). A first observation is that the P-episode for the VC*ic* contained a sharp peak at 76 Hz in several animals (Figure 3.6A*i*) suggesting a potential artifact in those recordings, although the source of this artifact is unclear as it is above the frequency for line noise. It was reassuring to note that when this artifact was present, it was only seen in the VC*ic* and did not contaminate other components. This highlights another advantage of the ICA method for removing artifacts (Jung et al., 2000). The P-episode for the remaining components included strong peaks at gamma frequency during both SO (Figure 3.6A *ii*-*vi*, colour) and theta (Figure 3.6A *ii*-*vi*, black). The peak gamma frequency in the SLM*ic* was 27.5 ± 1.1 Hz during the SO and 30.3 ± 1.2 Hz during theta, while the peak gamma frequency in the SchC*ic* was 36.2 ± 1.2 Hz during the SO and 30.8 ± 0.8 Hz during theta. Gamma activity was detected in both the MPP*ic* (SO and theta: 38 ± 4 Hz) and the LPP*ic* (SO: 39 ± 5 Hz; 43 ± 3 Hz) although the gamma peaks in both of these components were more broad, potentially reflecting some smearing across the slow and fast gamma ranges. Indeed some animals had two distinct gamma P-episode peaks (data not shown). However, phase analysis did not show any differences between slow and fast gamma, and therefore all results reported here group gamma into a single band. Finally, all components except the LPP*ic* had significant detections in the spindle (8-16 Hz) range during the SO. This was also evident in the cross-frequency coupling analysis

(Figure 3.6B), with the VC*ic*, PYR$_{CSD}$, SLM*ic* and MPP*ic* all showing visible modulation of spindle amplitude by SO (~1 Hz) phase. In addition, modulation of gamma amplitude by the SO phase was clear in several components, and strongest in the SLM*ic*. During theta, each of the components showed varying degrees of modulation of gamma amplitude by the phase of theta (Figure 3.6C *i-vi*), with the strongest coupling in the SLM*ic* and SchC*ic*. We did also note gamma modulation in the SLM*ic* for slower (~0.5 Hz) frequencies (Figure 3.6C*iv*). This will investigated in Chapter 4. Taken altogether, these findings highlight the existence of pathway-specific phase-amplitude co-modulation patterns during both theta and the SO.

3.4.4 Pathway-specific gamma frequency inputs separated by SO and theta phase

Phase-modulation of gamma activity was clearly apparent in both the raw and ICA-separated components (Figures 3.3 and 3.6). To clarify the spatial dynamics of gamma in the hippocampus, gamma (40 Hz) power, coherence and phase profiles were constructed as a function of normalized depth (Figure 3.7C). The power profile revealed a large peak spanning both SRad and SLM and a larger peak in SMol during both SO and theta. Based on the multiple power peaks for gamma activity, coherence and phase profiles were calculated using three different reference points: SOr (green), SRad (magenta), SLM (cyan) and SMol (blue). Gamma activity referenced to SMol reversed phase near the hippocampal fissure, suggesting that it could be related to the perforant path inputs from the EC. Gamma activity referenced to SLM and SRad reversed phase at both deep (fissure) and superficial (pyramidal) layers. Gamma activity referenced to SOr reversed phase near the pyramidal layer. These results show highly localized regions of gamma-related inputs to both CA1 and the DG.

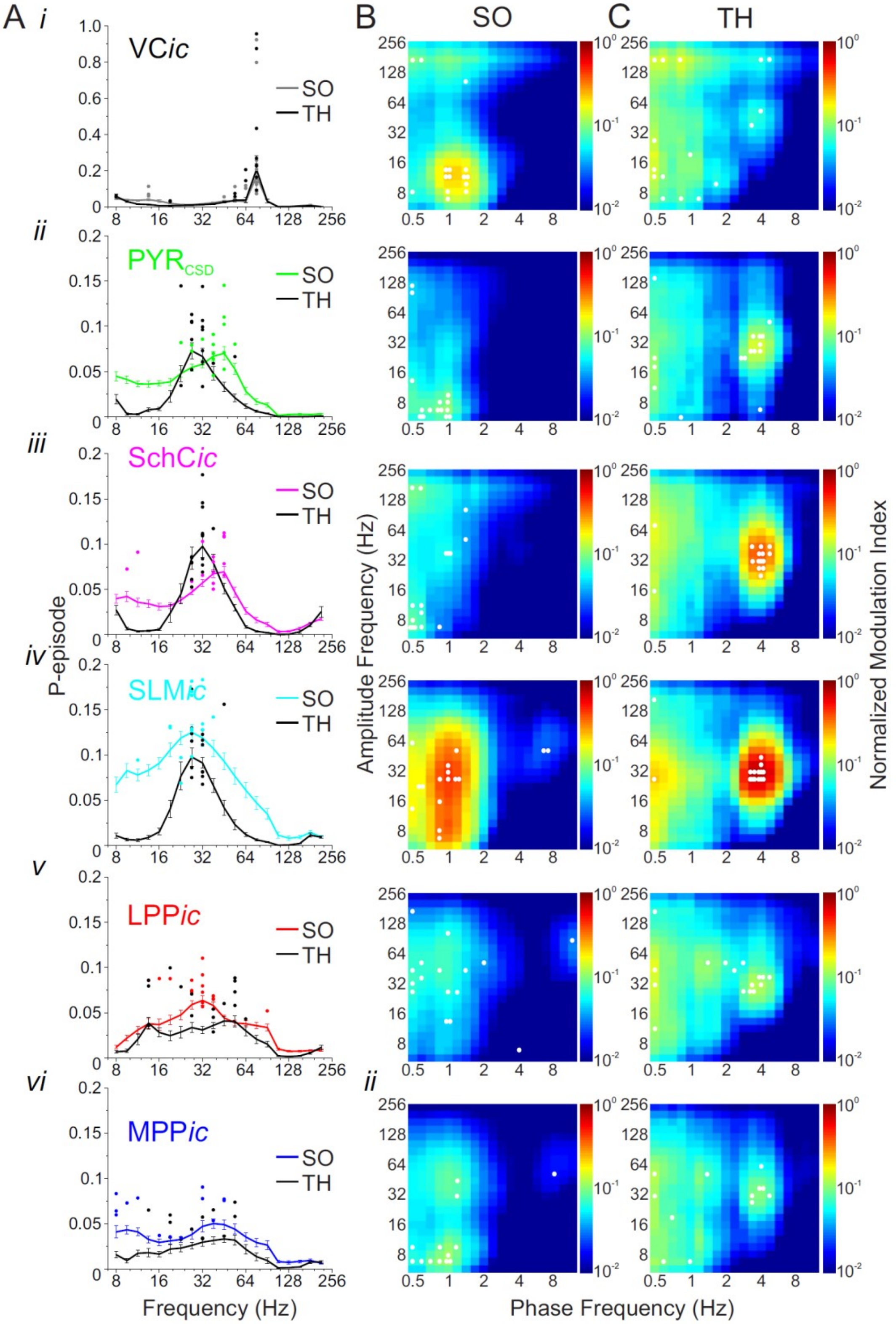

Figure 3.6 Independent components have characteristic frequency and cross-frequency (phase-amplitude) coupling signatures

Figure 3.6. Independent components have characteristic frequency and cross-frequency (phase-amplitude) coupling signatures.

(A) P-episode summary of BOSC oscillation detections (mean ± SEM) across frequencies as a function of state (colour – SO; black – theta) and component (*i* – VC*ic* (n = 16); *ii* – PYR_{CSD} (n=16), *iii* – SchC*ic* (n=16); *iv* – SLM*ic* (n=16); *v* – LPP*ic* (n=16); *vi* – MPP*ic* (n=13)). (B) Normalized component amplitude vs. CTX_{LFP} phase co-modulation plots for each component (*i*-*vi*) during SO (modulation index (MI) normalized based on the maximum and minimum MI values across all components and both states (SO and theta) for each subject). Co-modulation plots were smoothed with a window size of 4 frequency steps prior to averaging. MI peaks for each subject after smoothing are represented by white circles. (C) Normalized component amplitude – SLM_{LFP} theta phase co-modulation plots for each component (*i*-*vi*). MI values were normalized as in (C). In the SLM*ic* (*iv*), note a tendency for ultra-slow (>0.5 Hz) cross-frequency coupling of similar theta-couple bandwidths during theta epochs.

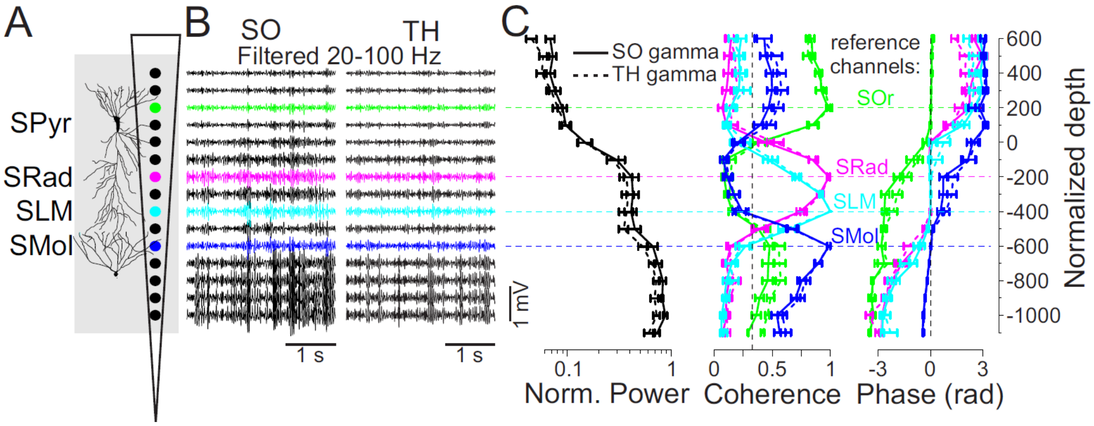

Figure 3.7 Depth profiles of gamma LFP activity show localized gamma modules with consistent properties across SO and theta states.

(A) Schematic representation of recording sites within the dorsal hippocampus. (B) Representative raw SO and theta signals filtered for gamma frequencies (20-100 Hz). (C) Power (left), coherence (middle) and phase (right) profiles of gamma frequency activity (40 Hz) as a function of depth during SO and theta states. Data represent mean ± SEM for all subjects (n=16), with depth normalized based on the reversal of theta activity (normalized depth = 0) and the maximal theta power (normalized depth = -400 μm). Coherence and phase profiles were constructed using SOr (+200 μm, green), SRad (-200 μm, magenta), SLM (-400μm, cyan) or SMol (-600 μm, blue) as reference sites. The significance level for coherence (0.33, black dotted line) was based on the mean 99% confidence limit of coherence values for a series of time-shifted, shuffled versions of the original dataset (see Viczko et al., 2014 for more details). Note the rapid drop in coherence as a function of distance from the reference site but the relatively strong coherence between SMol and SOr sites.

In order to better characterize the sources of gamma-frequency activity, we looked at the expression of gamma oscillations in the ICA-separated components as a function of SO and theta phase. Oscillatory activity was detected in each component using the BOSC method with a 99th percentile power threshold and 3-cycle duration threshold (see Methods section) and detections were collapsed across frequencies within the gamma band (20-100 Hz). The peak gamma frequency was determined within each state as the P-episode maximum (cf. Figure 3.6A). Representative distributions of gamma detections as a function of phase and summaries across subjects are shown for SO (Figure 3.8A-B) and for theta (Figure 3.8C-D). Only subjects with a significant mean angle for their distribution (Rayleigh test for circular uniformity, $p < 0.05$) were included in the phase summaries (Figure 3.8B and D).

The CA1 subfield receives gamma-frequency synaptic drive from the EC through the TA pathway to SLM and from the CA3 subfield through the SchC pathway to SRad (Bragin et al., 1995; Colgin et al., 2009). Gamma oscillations in both pathways were strongly modulated by the phase of both SO and theta oscillations (Figure 3.8A-D *i-ii*; note that the SLM*ic* might also reflect input from the nucleus reuniens). Consistent with the finding that gamma power at SLM is in phase while gamma power at SRad is out of phase with the neocortical SO (Isomura et al., 2006), SLM*ic* gamma activity during the SO occurred at a mean angle of 233° with respect to the neocortical SO (corresponding to the ascending phase or UP-DOWN transition; $r = 0.20$, $F_{(2,14)} = 44.79$, $p<0.05$), whereas SchC*ic* gamma activity during the SO occurred at a mean angle of 112° (the descending phase or DOWN-UP transition; $r = 0.07$, $F_{(2,13)} = 6.30$, $p<0.05$). These mean angles were significantly different from each other (Hotelling test for paired angles: $F_{(2,13)} = 20.15$, $p<0.05$). During theta, in agreement with recent findings (Schomburg et al., 2014), SLM*ic*

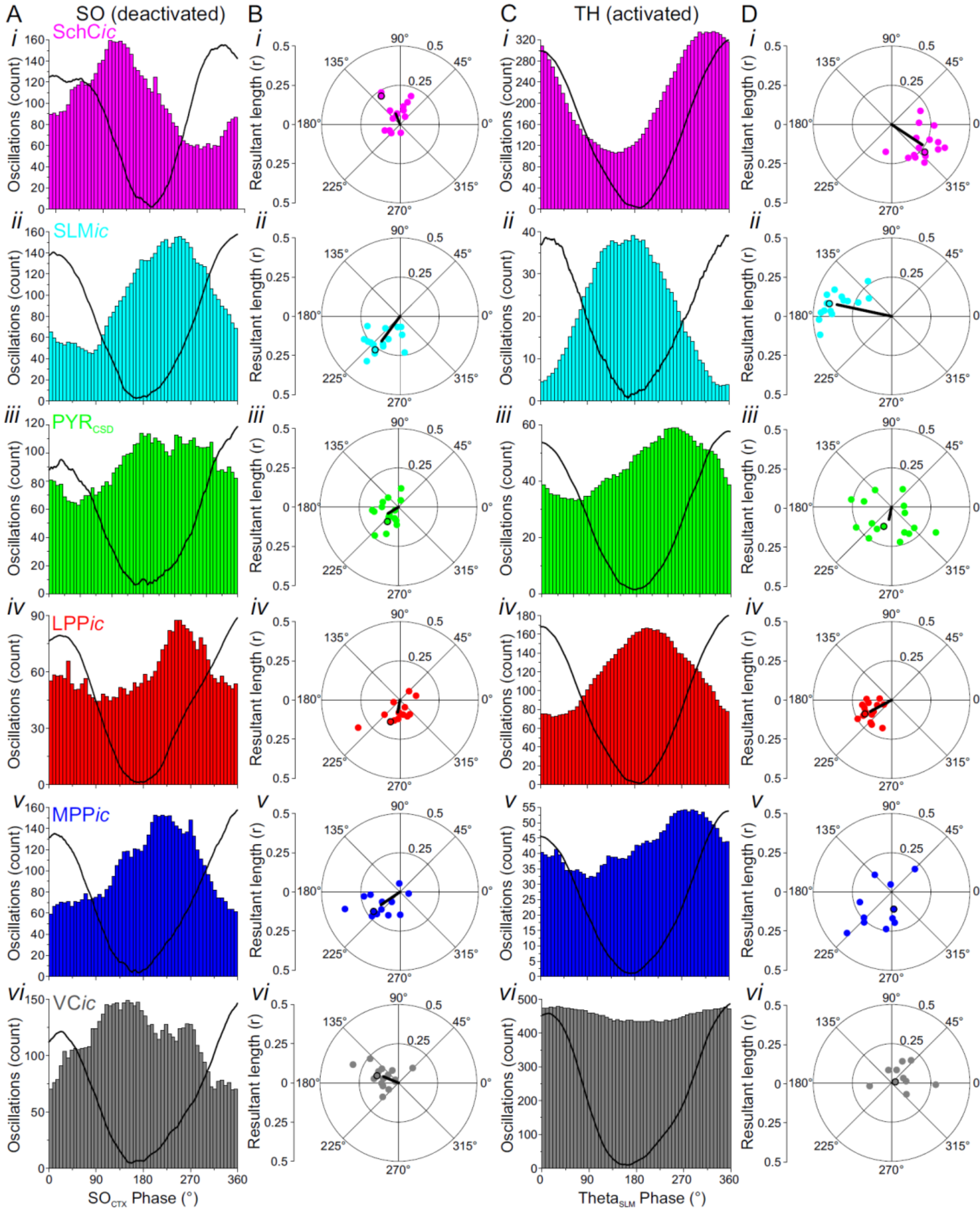

Figure 3.8 Gamma oscillations in ICA components show distinct phase-modulation by the SO and theta rhythms

Figure 3.8. Gamma oscillations in ICA components show distinct phase-modulation by the SO and theta rhythms.

(A) Representative distributions of detected gamma oscillations in SLM*ic*each component (*i*: SchC*ic*; *ii*: SLM*ic*; *iii*: PYR_{CSD}; *iv*: LPP*ic*; *v*: MPP*ic*; *vi*: VC*ic*) as a function of SO_{CTX} phase. Black traces represent average SO_{CTX} waveforms. (B) Group data for relationship of gamma detections to SO_{CTX} phase. Black line indicates significant mean of mean angles assessed using second order circular statistics (Zar, 2010). Black circle indicates representative examples used in (A). Only animals with significant mean angles (Rayleigh test for circular uniformity, $p<0.05$) are shown (*i*: SchC*ic* n = 15/16; *ii*: SLM*ic* n = 16/16; *iii*: PYR_{CSD} n = 10/16; *iv*: LPP*ic* n = 14/16; *v*: MPP*ic* n = 13/13; *vi*: VC*ic* n = 16/16). (C) Representative distributions of detected gamma oscillations in each component as a function of SLM_{LFP} phase. Black traces represent average SLM_{LFP} waveforms. (D) Group data for relationship of gamma detections to SLM_{LFP} phase. Black line indicates significant mean of mean angles. Black circle indicates representative examples used in (C). Only animals with significant mean angles are shown (*i*: SchC*ic* n = 16/16; *ii*: SLM*ic* n = 16/16; *iii*: PYR_{CSD} n = 14/16; *iv*: LPP*ic* n = 16/16; *v*: MPP*ic* n = 11/13; *vi*: VC*ic* n = 10/16).SLM*ic*SLM*ic* gamma activity occurred at a mean angle of 168° (near the trough of theta recorded at SLM; r = 0.36, $F_{(2,14)} = 207.44$, $p<0.05$) while SchC*ic* gamma activity during theta occurred at 327° (just before the peak of theta recorded at SLM; r = 0.24, $F_{(2,14)} = 61.10$, $p<0.05$). These mean angles were also significantly different from each other ($F_{(2,14)} = 665.83$, $p<0.05$). In summary, during both SO and theta states, gamma in the SLM*ic* and the SchC*ic* occur at opposite phases of the respective slower oscillation.

An important question is whether the ICA provides information above what could be obtained from analysis of the CSD alone. During theta, the CSD gamma phase at SLM (190°, r = 0.19, $F_{(2,13)} = 50.03$, $p<0.05$) and SRad (307°, r = 0.14, $F_{(2,13)} = 17.09$, $p<0.05$) were both significantly different from the SLM*ic* and SchC*ic* gamma phases, respectively (SLM_{CSD} vs SLM*ic*: $F_{(2,13)} = 10.46$, $p<0.05$; $SRad_{CSD}$ vs SchC*ic*: $F_{(2,13)} = 4.77$, $p<0.05$). Furthermore, the gamma phases for the CSD signals were shifted towards each other in comparison to the ICA-separated signals, suggesting that the CSD signal at a given lamina may be contaminated by activity at other laminae. During SO, while the phases of gamma CSD at SLM (232°, r = 0.14, $F_{(2,13)} = 27.40$, $p<0.05$) and at SRad (165°, r = 0.07, $F_{(2,13)} = 11.39$, $p<0.05$) were not significantly different from the phases of SLM*ic* and SchC*ic* gamma respectively (SLM_{CSD} vs SLM*ic*: $F_{(2,13)} = 1.55$, n.s.; $SRad_{CSD}$ vs SchC*ic*: $F_{(2,13)} = 3.03$, n.s.), the phase of CSD gamma at SRad was nevertheless shifted closer to that of the SLM*ic* gamma, again suggesting some mixing of the gamma signals in the CSD that is unmixed in the ICA components.

The first output of the hippocampal circuit originates from the CA1 pyramidal cell layer. Because the PYR*ic* was not consistently extracted across subjects, the CSD signal at SPyr was used to assess activity in this layer. We found that PYR_{CSD} gamma (peak frequency 38 ± 2 Hz during the SO and 31 ± 2 Hz during theta) showed a significant phase modulation to both the SO and theta (Figure 3.8A-D *iii*). $\mathrm{PYR_{CSD}}$ gamma occurred on the ascending phase of both the neocortical SO (mean angle 212°, r = 0.08, $F_{(2,14)} = 9.74$, $p<0.05$) and the SLM theta oscillation (mean angle 258°, r = 0.08, $F_{(2,14)} = 4.65$, $p<0.05$; Figure 3.8B *iii*). Interestingly, this suggests that $\mathrm{PYR_{CSD}}$ gamma occurs at the same phase as SLM*ic* gamma during the SO but occurs mid-way between the SchC*ic* and SLM*ic* gamma during theta (SO: $\mathrm{PYR_{CSD}}$ vs SchC*ic*: $F_{(2,13)} = 8.22$, $p<0.05$; $\mathrm{PYR_{CSD}}$ vs SLM*ic*: $F_{(2,14)} = 3.13$, n.s.; theta: $\mathrm{PYR_{CSD}}$ vs SchC*ic*: $F_{(2,14)} = 8.18$, $p<0.05$; $\mathrm{PYR_{CSD}}$ vs SLM*ic*: $F_{(2,14)} = 16.94$, $p<0.05$). These differences in coordination between the input and output layers of the hippocampus could underlie different modes of information processing during SO and theta states.

The entorhinal projection to the DG is separated into the MPP, arising from the medial EC, and the LPP, arising from the lateral EC. During the SO, both MPP*ic* and LPP*ic* gamma occurred on the rising phase of the neocortical SO (Figure 3.8A-B *iv*-*v*; MPP*ic*: 214°, r = 0.15, $F_{(2,11)} = 13.15$, $p<0.05$; LPP*ic*: 259°, r = 0.08, $F_{(2,12)} = 13.52$, $p<0.05$). These phases were significantly different from each other, with the LPP*ic* following the MPP*ic* ($F_{(2,9)} = 5.86$, $p<0.05$). During theta, only the LPP*ic* was significantly modulated by the SLM theta phase (Figure 3.8C-D*iv;* 208°, r = 0.15, $F_{(2,14)} = 70.00$, $p<0.05$). While the gamma activity in the MPP*ic* was significantly modulated by theta phase in 11/13 subjects and tended to occur on the rising phase of the SLM theta oscillation (Figure 3.8C-D*v*), the preferred phase was not significant across subjects. Due to the position of our recordings centered on the CA1 subfield, it could be that the MPP component, which is expected to have the most ventral activity profile, was not always well represented in our signal.

In addition to the components with sources located within the hippocampus, gamma frequency activity was also feature of the VC*ic* (Figure 3.8*vi*). Whether this represents imperfect separation of the VC*ic* or true volume-conducted gamma is unclear. In support of the latter, the phase of the VC*ic* gamma during the SO (157°, r = 0.10, $F_{(2,14)} = 10.82$, $p<0.05$) was significantly different from the gamma phase of all other hippocampal components (VC*ic* vs SLM*ic*: $F_{(2,14)} = 35.36$; VC*ic* vs SchC*ic*: $F_{(2,13)} = 5.26$; VC*ic* vs PYR_{CSD}: $F_{(2,14)} = 10.70$; VC*ic* vs LPP*ic*: $F_{(2,12)} = 33.95$; VC*ic* vs MPP*ic*: $F_{(2,11)} = 6.21$; all $p<0.05$), but not significantly different from the phase of gamma in the neocortex (CTX_{LFP} gamma: 157°, $F_{(2,14)} = 47.01$, $p<0.05$; VC*ic* vs CTX_{LFP}: $F_{(2,14)} = 1.67$, n.s.). During theta, although some animals did show a significant phase preference for VC*ic* gamma (Figure 3.8D*vi*) there was no significant modulation on average ($F_{(2,8)} = 2.88$, n.s.).

Overall, our analysis of pathway- and state-specific gamma modulation suggests that gamma-frequency inputs are segregated by phase of ongoing slower oscillations during both theta and SO activity states. The precise timing of activity in afferent pathways is likely critical in the correct integration of information arriving from disparate sources, and the parsing of this information can be modulated by brain state.

3.4.5 Cycle skipping in the SLMic

Despite the fact that the SLM*ic* showed a very strong phase-coupled gamma modulation by the neocortical SO, the spectrum of the SLM*ic* during the SO showed a broad peak in the frequencies below 1 Hz instead of a sharp peak at ~1 Hz as in the neocortex (Figure 3.9A). This slowing of SO activity in the SLM*ic* is consistent with a recent report of the slower phasing of SO activity in layer III EC cells that give rise to the TA pathway (Hahn et al., 2012). This slowing was suggested to result from persistent up-states that outlasted the duration of neocortical up-states. We therefore looked for evidence of persistent activity in the population activity apparent in the SLM*ic*. Visual inspection of the time course (Figure 3.9A inset) and

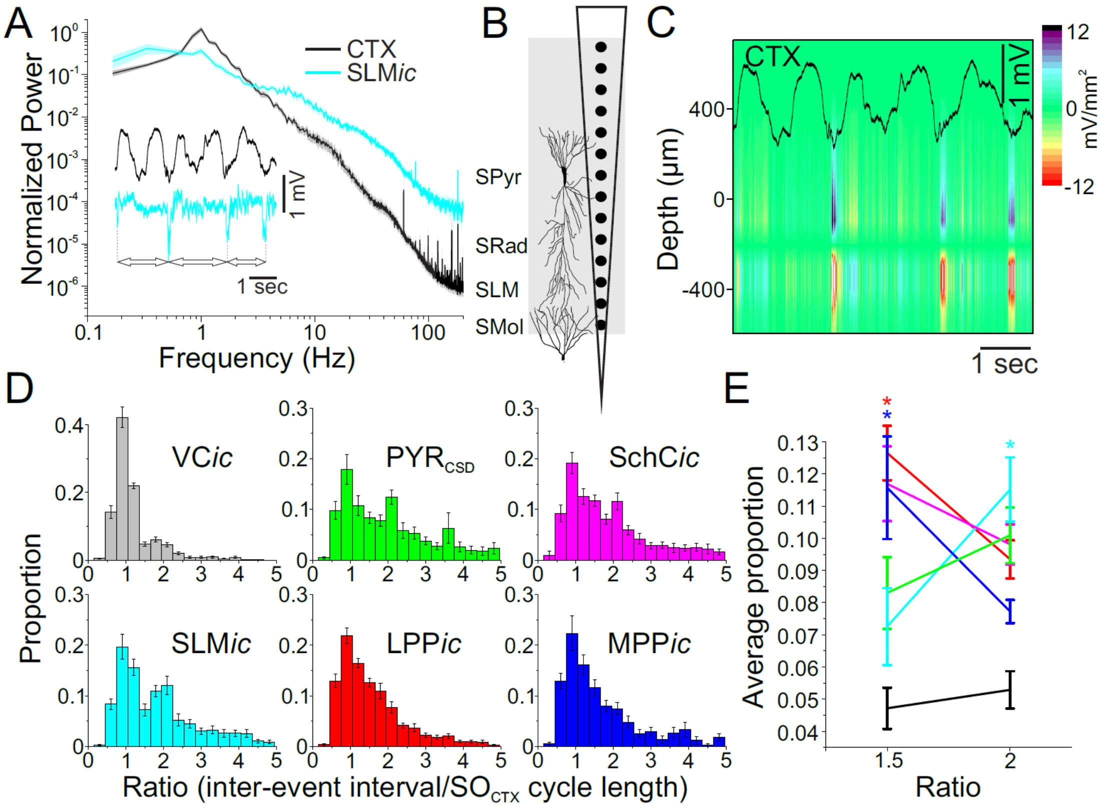

Figure 3.9 Cycle-skipping in the SLM*ic* during the SO.

(A) Mean ± SEM of neocortical signal (black) and SLM*ic* (cyan) during the SO normalized by the maximum power for each subject (n=16), showing a strong ~1 Hz peak in the neocortex and a broader peak extending below 1 Hz in the SLM*ic*. Inset shows representative time course of neocortical and SLM*ic* signals, showing coordinated activity of the SLM*ic* skipping some cycles of the neocortical SO. Bidirectional arrows represent the identification of inter-event intervals for analysis of cycle-skipping. (B) Schematic representation of recording sites within the dorsal hippocampus. (C) CSD of SLM*ic* during the same time segment as the inset in A, with the neocortical signal overlayed (black trace). Again note the distinct pattern of the SLM*ic* skipping cycles of the neocortical SO. (D) The distribution of the ratio of each inter-event interval to the nearest SO_{CTX} cycle length for all components. Note second peak in the SLM*ic* distribution at an integer ratio of 2, and prominent trough at the non-integer ratio of 1.5. (E) Summary of the proportion of events at ratios of 1.5 and 2. Only the SLM*ic* (cyan) had significantly more events with a ratio of 2 ($p<0.05$).

CSD (Figure 3.9C) of the SLM*ic* revealed that the gamma-related sinks could skip cycles of the neocortical SO (Figure 3.9C), however this did not appear to be due to persistent periods of population activity but rather to persistent periods of inactivity. In support of this, the mean duration of gamma events in the SLM*ic* was 269 ± 49 ms, and 90% of all gamma event durations in the SLM*ic* were less than 540 ms (~1/2 of the duration of a single SO cycle). Furthermore, the relative rate of occurrence of all detected oscillations in the SLM*ic* pathway was significantly lower during neocortical DOWN states (SO_{CTX} phase <90° or >270°) than during up-states (SO_{CTX} phase 90°-270°; $p<0.05$). Therefore our results are inconsistent with the idea of persistent activity in the population of cells that give rise to the TA pathway.

To evaluate the consistency of cycle skipping across subjects, events were defined as minima in the component LFP time series and the ratio of each inter-event interval to the nearest neocortical SO cycle length was determined (see inset of Figure 3.9A, bidirectional arrows marking inter-event intervals; group data in Figure 3.9D). In comparison to the VC*ic,* all hippocampal component distributions had lower peaks at a ratio of 1 as well as longer tails. However, the SLM*ic* was unique in showing a peak in the proportion of events with a ratio of 2 (i.e. an integer number of cycles) that was significantly larger than the proportion of events at a ratio of 1.5 (i.e. a non-integer number of cycles; Figure 3.9 SLM*ic*). This suggests that when activity in the SLM-targeting inputs skips SO cycles, they do so at an integer number (usually only a single skipped cycle), therefore maintaining the phase relationship with the neocortical SO.

3.4.6 Spindle oscillations in EC inputs and CA1 output

In addition to gamma oscillations, the phase-amplitude co-modulation plots of both raw (Figure 3.3G-I) and ICA-separated (Figure 3.6B,D,E) signals suggested

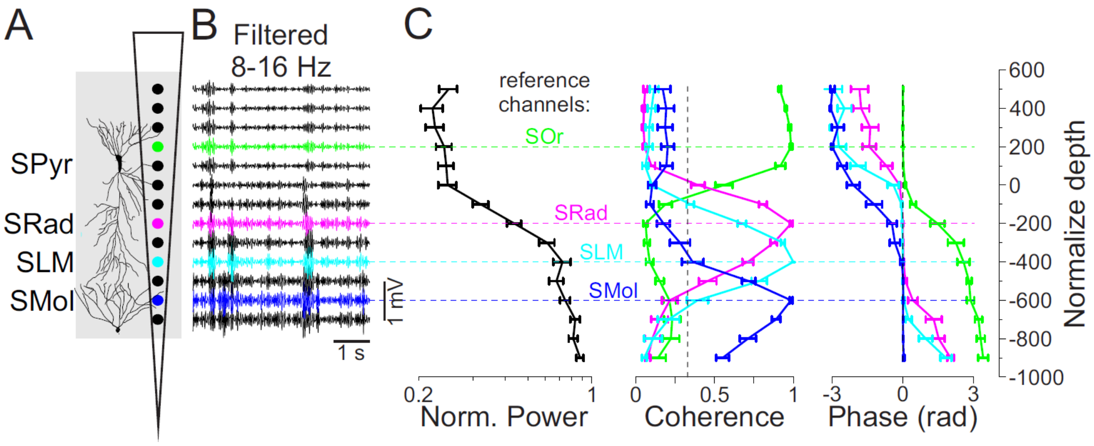

Figure 3.10 Depth profiles of spindle activity show localized modules within the dorsal hippocampus.

(A) Schematic representation of recording sites within the dorsal hippocampus. (B) Representative raw signal during the SO, filtered for spindle frequencies (8-16 Hz). (C) Power (left), coherence (middle) and phase (right) profiles of spindle frequency activity (10 Hz) as a function of depth during the SO state. Data represent mean ± SEM for all subjects (n=16), with depth normalized based on the reversal of theta activity (normalized depth = 0) and the maximal theta power (normalized depth = -400 μm). Coherence and phase profiles were constructed using SOr (+200 μm, green), SRad (-200 μm, magenta), SLM (-400μm, cyan) or SMol (-600 μm, blue) as reference sites. The significance level for coherence (0.33, black dotted line) was based on the mean 99% confidence limit of coherence values for a series of time-shifted, shuffled versions of the original dataset. Note the rapid drop in coherence as a function of distance from the reference site.

that spindle-frequency (8-16 Hz) oscillations are a prominent feature of hippocampal activity during the SO. While spindle oscillations are well-known to co-occur with the neocortical SO, our findings are in agreement with a recent description of spindle oscillations in the hippocampus as well (Sullivan et al., 2014). The power profile of spindle activity showed peaks at SLM and in the DG (Figure 3.10C, left panel). While this power profile was similar to the profile for gamma activity (Figure 3.7C, left panel), a key difference was the lack of a power peak in SRad, suggesting that this activity is primarily mediated through the EC inputs to CA1 and the DG. Coherence and phase profiles (Figure 3.10C, middle and right panels) suggested that this is a highly localized rhythm, with coherence dropping off rapidly with distance from the reference site.

In order to characterize the origin of hippocampal spindle oscillations, we looked at spindles in the ICA-separated components in addition to the frontal neocortical channel. We detected spindle oscillations that were modulated by the neocortical SO in the MPP*ic*, the SLM*ic,* and the $\mathrm{PYR}_{\mathrm{CSD}}$ (Figure 3.11A,C-D; blue, cyan and green respectively). Interestingly, spindles were not a clear feature of the LPP*ic*. Although they were sometimes detected, spindles in the LPP*ic* failed to show a consistent phase relationship with the neocortical SO and therefore were not analyzed further. Frontal neocortical spindles ($\mathrm{CTX}_{\mathrm{LFP}}$) occurred at a rate of 25.3 ± 1.7 events/minute during the SO state, with an average intra-spindle frequency of 14.7 ± 0.4 Hz, at an average phase of 146° with respect to the SO (i.e. near the DOWN-UP transition; Figure 3.11A-B; $r = 0.28$, $F_{(2,13)} = 27.6$, $p<0.05$). Hippocampal spindles in the MPP*ic*, and SLM*ic* (input pathways) occurred with a phase delay compared to $\mathrm{CTX}_{\mathrm{LFP}}$ spindles (Figure 3.11A and C). MPP*ic* spindles occurred at a rate of 19.0 ± 1.1 events/minute, with an average intra-spindle frequency of 10.7 ± 0.8 Hz, and a mean angle of 194° with respect to the neocortical SO ($r = 0.17$, $F_{(2,12)} =$

48.00, $p<0.05$), corresponding to a significant phase delay from frontal neocortical spindles of 143 ± 23 ms ($F_{(2,10)} = 22.94$, $p<0.05$). SLM*ic* spindles occurred at a rate of 28.4 ± 1.2 events/minute with a mean intra-spindle frequency of 12.7 ± 0.8 Hz and a mean angle of 232° with respect to the cortical SO ($r = 0.20$, $F_{(2,14)} = 54.09$, $p<0.05$), corresponding to a significant phase delay from the CTX_{LFP} spindles of 265 ± 18 ms ($F_{(2,13)} = 178.78$, $p<0.05$) and from MPP*ic* spindles of 113 ±24 ms ($F_{(2,11)} = 10.17$, $p<0.05$). In addition, spindles were detected in the VC*ic* at a phase of 156° ($r = 0.24$, $F_{(2,11)} = 37.02$, $p<0.05$), and this phase was not different from the phase of CTX_{LFP} spindles ($F_{(2,11)} = 1.39$, n.s.). Despite the fact that MPP*ic* and SLM*ic* spindles occurred at different phases, they were more likely than chance to co-occur on the same SO cycle (ratio of observed/expected = 1.37 ± 0.06), and this relationship was significant ($\chi^2 > 3.84$; $p<0.05$) in 11/13 animals. There was also a significant relationship between CTX_{LFP} and VC*ic* spindles (observed/expected = 1.43 ± 0.04; $p<0.05$ in 13/16 animals), suggesting that there is synchronization of spindle events across the cortex. There was, however, no significant relationship between hippocampal spindles and neocortical spindles based on the χ^2 analysis. Whether hippocampal spindles are driven by classical thalamocortical spindles reaching the hippocampus via the EC, or whether they represent a separate phenomenon with an overlapping frequency range remains unclear from these data.

In terms of output components, spindle events were also a feature of the PYR_{CSD} (Figure 3.11A), where they occurred with an intra-spindle frequency of 11.1 ± 0.9 Hz at a similar phase to the SLM*ic* spindles (237°, $r = 0.16$, $F_{(2,11)} = 59.22$, $p<0.05$), although the angles were significantly different ($F_{(2,11)} = 7.48$, $p<0.05$). There was no evidence of significant temporal co-occurrence of PYR_{CSD} and CTX_{LFP} spindles, but PYR_{CSD} spindles were more likely to occur on cycles with spindles in the input components (PYR_{CSD} and SLM*ic*: observed/expected = 1.7 ± 0.1, $p<0.05$ in

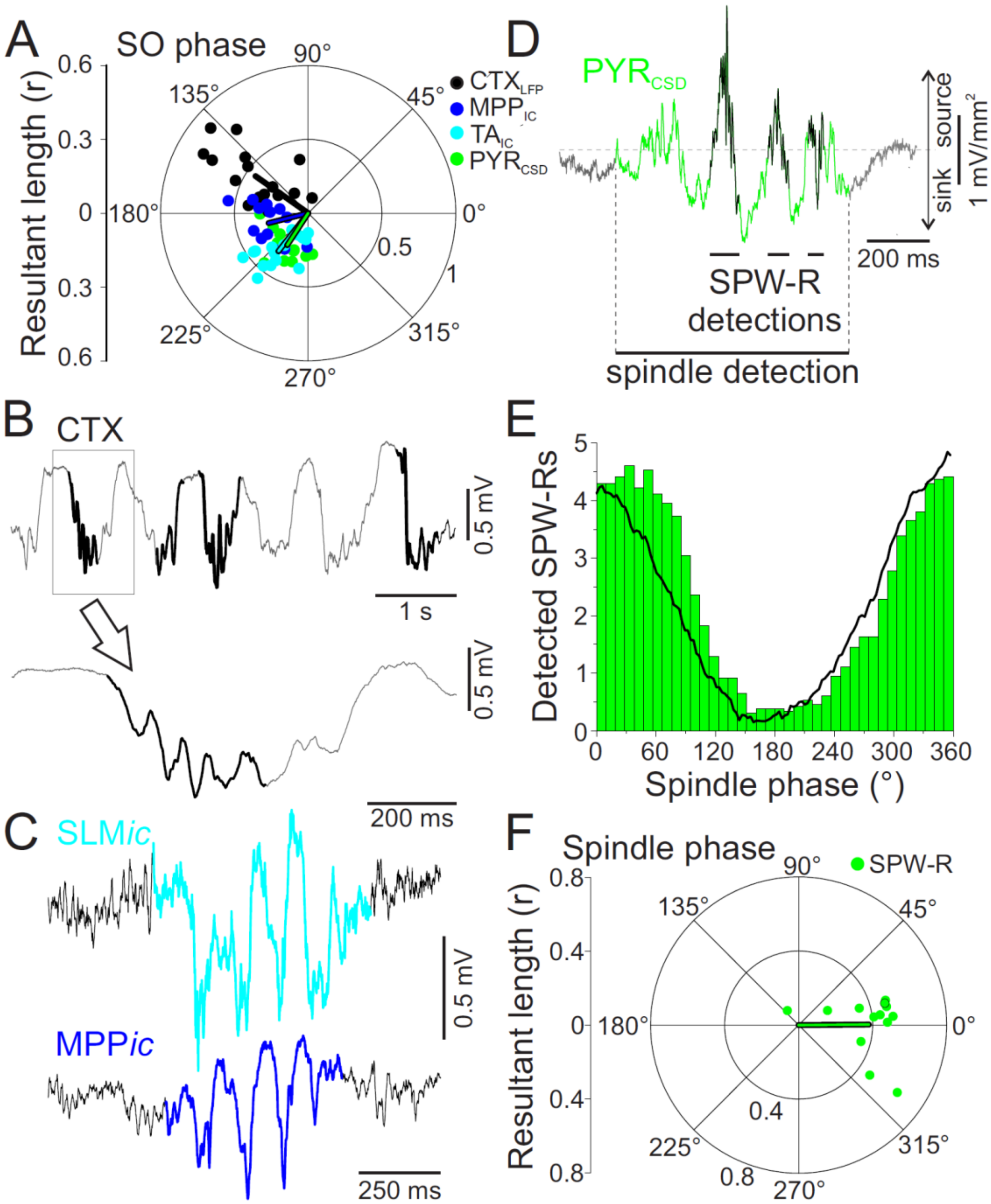

Figure 3.11 Hippocampal spindle oscillations and relationship with SPW-Rs.

Figure 3.11. Hippocampal spindle oscillations and relationship with SPW-Rs.

(A) Group data for mean angles of detected spindle oscillations. Only animals with significant mean angles are shown (CTX_{LFP}: n = 15/16; SLM*ic* n = 16/16; MPP*ic* n = 13/13; PYR_{CSD} n = 11/16). Lines indicate significant mean of mean angles. Note the phase delay between spindles detected from the frontal neocortical site and those detected within the hippocampus. (B) Representative neocortical raw signal with detected spindle oscillations highlighted in black. (C) Representative SLM*ic* and MPP*ic* signals with detected spindle oscillations highlighted in cyan (SLM*ic*) and blue (MPP*ic*). (D) Representative spindle detection in the PYR_{CSD} (green) showing coincidence of ripple detections (black). (E) Distribution of ripple detections as a function of spindle phase for all PYR_{CSD} spindle detections in a representative animal. Mean spindle waveform is shown in black. (F) Group data for experiments showing a consistent phase relationship for ripples detected during PYR_{CSD} spindle oscillations (n = 13/16). Arrow indicates significant group mean angle. Black outline highlights the subject shown in (E).

15/16 animals; $\mathrm{PYR}_{\mathrm{CSD}}$ and MPP*ic*: observed/expected = 1.6 ± 0.1, p<0.05 in 10/13 animals). In addition, spindles in the $\mathrm{PYR}_{\mathrm{CSD}}$ were correlated with $\mathrm{PYR}_{\mathrm{CSD}}$ ripples (100-200 Hz; Figure 3.11D-F), which is in agreement with the findings of Sullivan et al. (2014). Ripples were more likely to occur on an SO cycle in which a $\mathrm{PYR}_{\mathrm{CSD}}$ spindle was detected (observed/expected = 2.6 ± 0.5, p<0.05 in 11/14 animals). Within detected spindle oscillations, there was a clear relationship of ripples to spindle phase, with a preferred angle of 0° (corresponding to the peak of the $\mathrm{PYR}_{\mathrm{CSD}}$-detected spindle; r = 0.38, $F_{(2,11)}$ = 33.00, p<0.05; Figure 3.11E & F). Whether the spindle/ripple phenomenon reported here reflects the influence of neocortical spindles on the hippocampal network is not clear. Alternatively they could be a phenomenon unique to the hippocampus that overlaps with spindle frequency, such as the propensity for SPW-Rs to cluster at a ~10 Hz (Papatheodoropoulos, 2010). In either case, spindle-frequency activity patterns are clearly a feature of both the input and output pathways of the hippocampus, suggesting that they play an important role in coordinating hippocampal-neocortical communication during the SO.

3.4.7 Sharp Waves-Ripples occur at a distinct phase from SchC gamma

While $\mathrm{PYR}_{\mathrm{CSD}}$ ripples were found to occur at an increased rate during $\mathrm{PYR}_{\mathrm{CSD}}$ spindles, this relationship did not account for all events. SPW-Rs are one of the most characteristic activity patterns of the SchC-CA1 axis and are of particular interest because of their relationship to sleep-dependent memory consolidation (Csicsvari et al., 2000; Girardeau et al., 2009; Ego-Stengel and Wilson, 2010; Sullivan et al., 2011). Typically, a large-amplitude sharp wave in the SchC pathway will trigger a ripple event in the CA1 pyramidal cell layer. The detection of $\mathrm{PYR}_{\mathrm{CSD}}$ ripples was quite variable across subjects, with an average of 26.5 ± 7.7 events and an average ripple frequency of 157 ± 7 Hz. As expected, the number of ripples detected during theta was exceedingly low (3.0 ± 1.1), supporting the identity of these events as true SPW-R events. Accordingly, 87± 3% of all detected ripples were associated with a sharp wave in the SchC*ic* that exceeded an amplitude threshold of 4 standard deviations from the mean (Figure 3.12A-B), and these sharp-wave associated ripples (SPW-Rs) were used for subsequent analyses. In addition to the variability in event numbers, the SO phase-preference of detected SPW-Rs was also quite variable both within and across subjects. While 10 animals showed a significant SO phase preference for $\mathrm{PYR_{CSD}}$ SPW-Rs (231°, r = 0.13, $F_{(2,8)} = 5.46$, $p<0.05$), the preferred phases were spread across more than half of the cycle (from 148° to 359°), and inspection of individual events suggested the possibility of a bimodal distribution. However, we failed to find a significant bimodality across animals, possibly due to the low number of detections overall. Nevertheless, we did find an interesting relationship between the phase of SPW-Rs and the power of the neocortical SO. SPW-Rs occurring on the ascending phase of the neocortical SO (>180°, 16 ± 4 SPW-Rs/animal) were associated with significantly higher SO power than SPW-Rs occurring on the descending phase (<180°, 12 ± 3 SPW-Rs/animal; Figure 3.12D; normalized power 0.81 ± 0.11 vs. 0.55 ± 0.09, $p<0.05$). The descending- and ascending- SPW-R-triggered averages of the $\mathrm{CTX_{LFP}}$ show the separation in phase (Figure 3.12C), however the ~1 Hz waveform of the SO is apparent in both cases, confirming that the results are not due to differences in the ability to quantify SO phase when power is low. The average waveforms of ascending phase and descending phase sharp waves in the SchC*ic* and the amplitude envelope of the ripple oscillations in the PYR*ic* were not significantly different (Figure 3.12 E-F). Overall these results suggest that SPW-Rs tend to precede the neocortical UP-state when SO power is low, while they tend to follow the UP-state when SO power is high. This could allow the hippocampus to alternate between sending and receiving

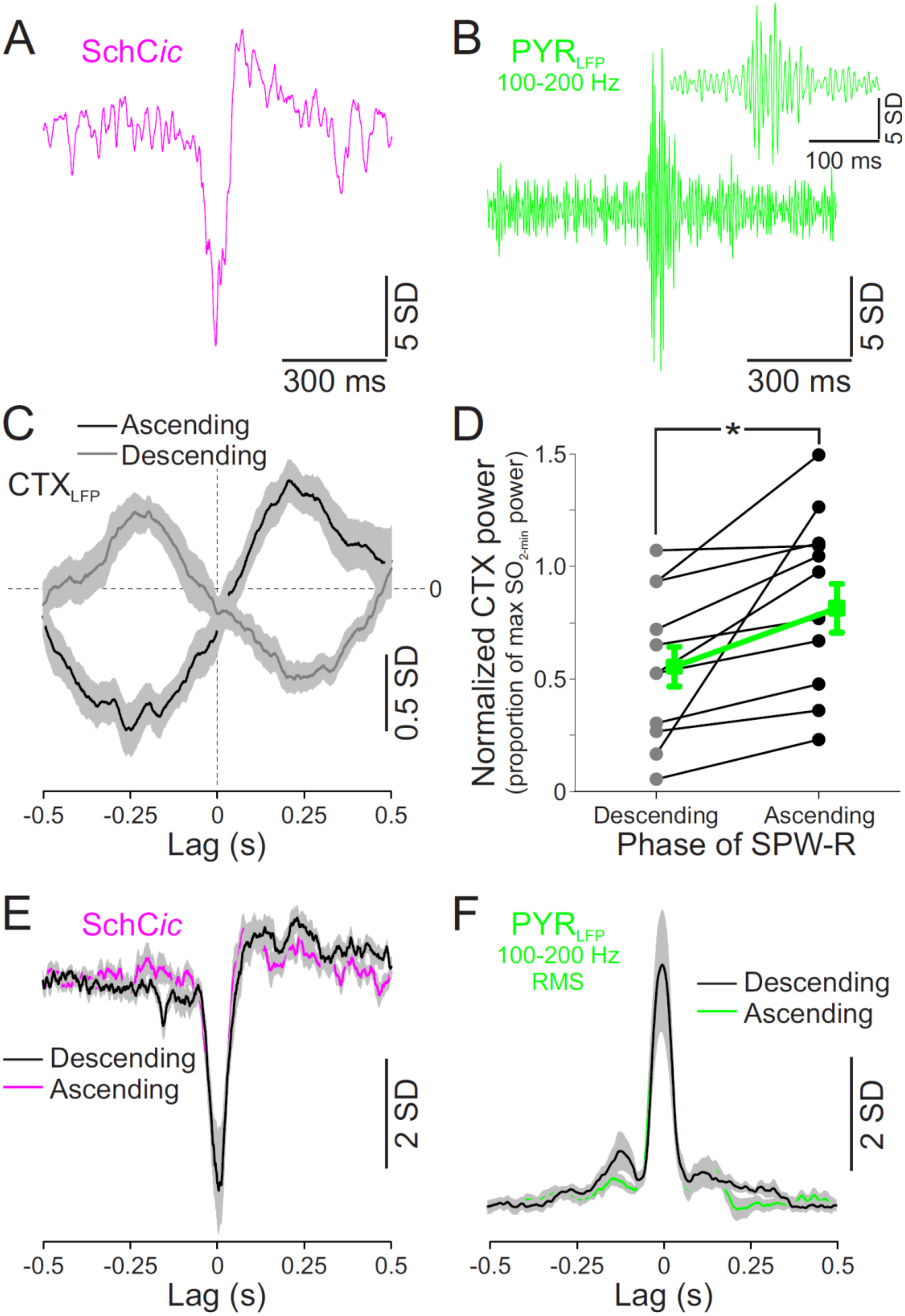

Figure 3.12 Phase of SPW-R events predicts SO$_{CTX}$ power

Figure 3.12. Phase of SPW-R events predicts $\mathrm{SO}_{\mathrm{CTX}}$ power.

(A) Representative sharp wave in the SchC*ic* during a detected SPW-R event. (B) Representative ripple oscillation (filtered from 100-200 Hz) in the $\mathrm{PYR}_{\mathrm{LFP}}$ during the same detected SPW-R event as in (A), magnified in inset to highlight the oscillatory nature of this event. (C) Mean SPW-R-triggered $\mathrm{CTX}_{\mathrm{LFP}}$ when SPW-Rs are separated into those occurring on the descending (<180°) and those occurring on the ascending (>180°) phase of the neocortical SO. (D) $\mathrm{SO}_{\mathrm{CTX}}$ power (normalized by the maximum 2-minute average of $\mathrm{SO}_{\mathrm{CTX}}$ power) during descending- vs. ascending- phase SPW-Rs. Group averages shown in green. These were significantly different based on a paired two-tailed t-test ($p<0.05$). (E) Average SPW-R-triggered SchC*ic* activity for descending- vs. ascending-phase SPW-Rs, showing no difference in the sharp wave waveform for the two groups. (F) Average SPW-R-triggered RMS of 100-200 Hz $\mathrm{PYR}_{\mathrm{LFP}}$ activity for descending- vs. ascending-phase SPW-Rs, showing no difference in the ripple amplitude or duration for the two groups.

information from the neocortex, potentially altering the direction of information flow as a function of strength of the neocortical SO.

3.5 Discussion

In the present study our aim was to understand how hippocampal input and output pathways are organized by the slow oscillation, and to compare this to what has previously been shown for theta dynamics. The ultimate goal was to arrive at a better understanding of how hippocampal networks could support memory consolidation during nonREM sleep. Our approach was to separate the contributions of individual hippocampal pathways from the mixed LFP signal using ICA. A summary of our phase-by-state-by-pathway findings is presented in Figure 3.13, highlighting the separation of activity patterns based on anatomical location, phase preference, pathway specificity, and global brain state.

3.5.1 Phase segregation of pathway-specific gamma oscillations by theta and the SO

During theta oscillations, our results confirm recent work with respect to the phase of gamma frequency inputs from EC and CA3 to CA1 (Lasztoczi and Klausberger, 2014; Schomburg et al., 2014), while with respect to the phase of the EC input they do not match a prior study (Colgin et al., 2009). For comparisons with previous studies, it is important to note that we used SLM as the reference theta signal while others have used SPyr, where the polarity of theta is reversed by 180° (see Figure 3.1C, red trace, right panel). One advantage of SLM theta is its amplitude, which allows for excellent estimates of both phase and state. Another interesting difference in our study concerns the frequency of theta-modulated gamma activity in the SLM*ic*, which we found in the slow (20-60 Hz) gamma band,

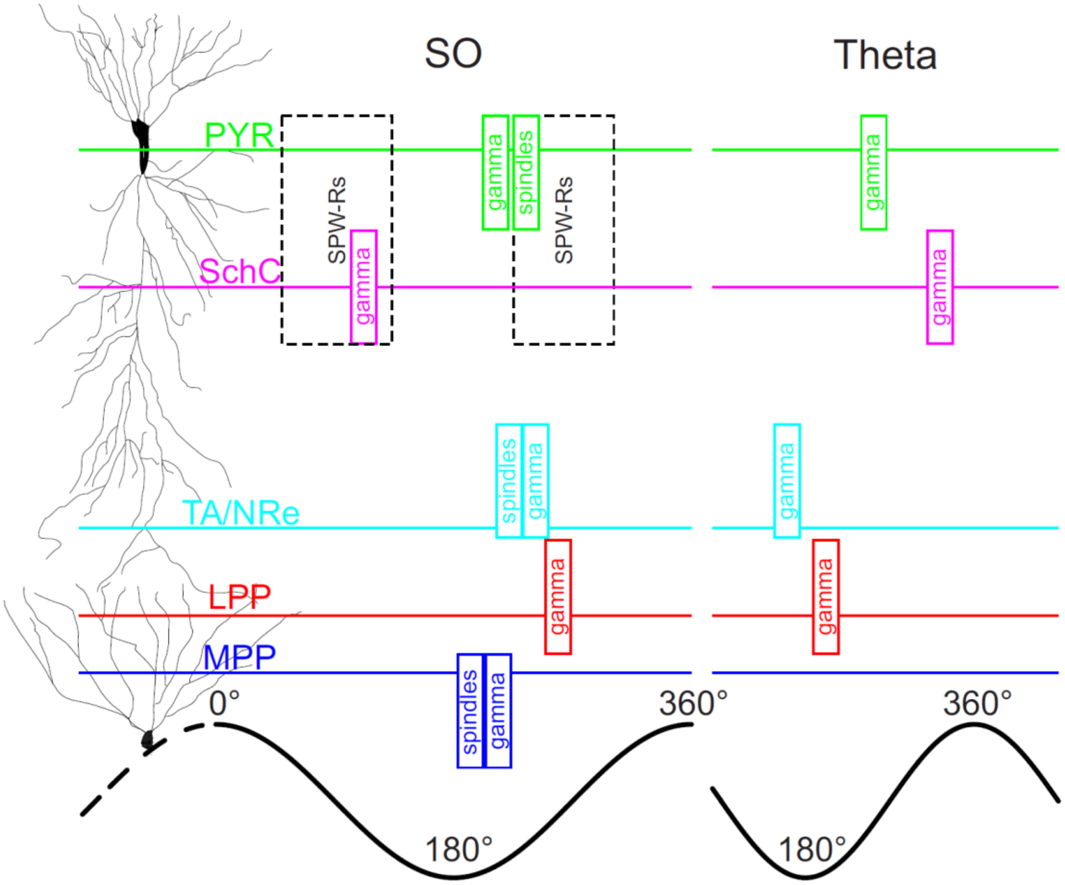

Figure 3.13 Summary diagram.

Schematic representation of the segregation of activity patterns within the dorsal hippocampus as a function of state (SO – left panel; theta – right panel), phase (x-axis), depth (y-axis), pathway (colour) and activity pattern (spindles, gamma, and SPW-Rs). Reference phase for the SO is from the deep layers of the frontal neocortex. Reference phase for theta is from SLM while others have described this input to be in the fast (60-140 Hz) gamma band (Colgin et al., 2009; Schomburg et al., 2014). One possibility is the influence of the anaesthetic urethane used in our study, as others have found the EC input to be in the slow (~30 Hz) gamma range under urethane (Lasztoczi and Klausberger, 2014). Regardless, it should be pointed out that a key advantage of using ICA to separate pathway-specific inputs is that sources that overlap in frequency and spatial extent can be separated into physiologically meaningful independent components instead of relying on differences in frequency alone to separate the influences of putatively distinct pathways.

While our findings with respect to gamma oscillations during the theta rhythm largely confirm previous work and extend it to the pathway-specific inputs separated by ICA, our major goal was to come to a better understanding of the hippocampal coordination of fast network activities associated with the SO. We found that, as for theta, the SO segregates gamma in the TA and SchC pathways based on phase. Importantly, during the SO, the SchC gamma (as well as a subpopulation of SPW-Rs) are the only hippocampal activity to precede the neocortical UP-state within an SO cycle. This is in agreement with previous work finding that the increase in gamma power in SRad is out of phase with the increase in gamma power in SLM (Isomura et al., 2006). This unique phase relationship of SchC gamma to the SO could also be partially explained by the finding that some cells within CA3 are out of phase with neocortical UP-DOWN states (Hahn et al., 2007). While the functional relevance of this phase segregation is unclear, it is tempting to speculate that the neocortical DOWN-state provides a critical window for independent intra-hippocampal processing mediated by network interactions within CA3 that are transmitted to CA1 as gamma frequency activity or sharp waves, while the neocortical UP-state provides a window for neocortical-hippocampal communication mediated by direct entorhinal-CA1 gamma frequency inputs.

3.5.2 SPW-R phase is modulated by global brain state

Another significant finding was that SPW-Rs could precede or follow the neocortical UP-state. This is in agreement with previous findings that these events can occur near the DOWN-UP or the UP-DOWN transitions of the neocortical SO (Peyrache et al., 2011). However, we extended these findings by showing that these two groups of SPW-Rs could be separated based on the power of the neocortical SO. SPW-Rs occurring on the descending phase (DOWN-UP transition), were associated with lower 1 Hz power than SPW-Rs occurring on the ascending phase (UP-DOWN transition). Thus, SPW-Rs tend to lead neocortical activity when the SO power is low, and follow neocortical activity when the SO power is high. This provides the opportunity for two distinct directions of information flow in the hippocampal circuit that are based on depth of the slow wave state: the first in which hippocampal output is poised to influence cortical ensembles and the second when hippocampal ensembles may be directed by neocortical input. SPW-Rs are of critical interest with respect to sleep-dependent memory consolidation based on the reactivation of previously co-active hippocampal ensembles (perhaps constituting episodic memory traces) during ripples (Girardeau and Zugaro, 2011) as well as the disruption of memory following the selective disruption of SPW-Rs (Girardeau et al., 2009; Ego-Stengel and Wilson, 2010). Therefore it is also interesting to note a strong relationship between SPW-Rs and spindle oscillations in the $\mathrm{PYR}_{\mathrm{CSD}}$. While spindles had previously been thought of as purely thalamocortical events, it has recently been demonstrated that spindle oscillations (presumably transmitted via entorhinal input) influence hippocampal activity and that SPW-Rs occur at an increased rate during CA1 pyramidal layer spindles (Sullivan et al., 2014). Our findings support these previous results and extend them to the urethane model of sleep, and together these results suggest a mechanism that could link hippocampal and neocortical activity during nonREM sleep to support sleep-dependent memory consolidation.

3.5.3 Cycle skipping of synaptic inputs at SLM

The strongest modulation of fast activity by SO phase occurred in the SLM*ic*, which fit with our observation that the strongest cross-frequency modulation of the raw signal occurred near SLM. While the SLM*ic* did show a spectral peak near 1 Hz corresponding to the SO, the peak was much broader and extended into the lower frequencies. This slowing of the SLM inputs (including the TA pathway from the EC and potentially the nucleus reuniens afferents) compared to the neocortical SO frequency can be explained by our finding that the SLM*ic* input skips some SO cycles. This produces the characteristic hippocampal field activity during the SO that has distinctly rhythmic features but can also appear arhythmic. One possible explanation for this dissociation of the EC input from the neocortical SO comes from the finding that layer III medial EC cells show persistent UP-states that can span several cycles of the SO, leading to a slowing of the dominant frequency in this population of cells (Hahn et al., 2012). However, our finding that fast activity in the SLM*ic* still tended to occur in short bouts during cycle skipping (cf. Figure 3.9) does not support the idea of sustained UP-states in the population of EC neurons primarily responsible for the input at SLM. Future studies will be critical in elucidating the relationship between population activity in layer III medial EC and the CA1 TA input.

3.5.4 Summary

The networks of the hippocampus are capable of producing markedly different activity patterns based on behavioural- and brain-state. Large amplitude LFP patterns such as the SO and theta represent the synchronous, coordinated activity of large populations of neurons and can therefore provide significant clues in understanding the hippocampal processing that occurs within these respective states. One challenge of LFP analysis is localizing the source of signals that can be volume-conducted from significant distances within the brain. The ICA method provides a powerful tool for overcoming this ambiguity, allowing the separation of signals into physiologically meaningful underlying sources. Our findings reveal a network that can dynamically alter its coordination as a function of brain state. During slow-wave states, the neocortical DOWN-state and DOWN-UP transition may provide a critical window for intrahippocampal processing revealed by gamma oscillations in the SchC pathway and SPW-Rs occurring when cortical SO power is low. This suggests that in transitional slow wave (or non-REM-like) activity, there is a directional bias for hippocampo-cortical communication. In contrast, the hippocampal inputs from the EC occur in phase with the neocortical UP-state, providing a window for cortical influence on hippocampal circuits. This capacity of hippocampal circuits to integrate and segregate rhythmic inputs differentially based on brain state is likely what gives it the power to perform such diverse memory-related functions.

4 IOTA: A novel slower-than-slow rhythm modulates ongoing hippocampal activity across both activated and deactivated brain states

Authors: *Tara A. Whitten[1], *Zahid Padamsey[1], and Clayton T. Dickson[1,2,3]

[1]Neuroscience and Mental Health Institute, University of Alberta, Edmonton, AB, Canada, T6G 2E1
[2] Department of Psychology, University of Alberta, Edmonton, AB, Canada, T6G 2H7
[3] Department of Physiology, University of Alberta, Edmonton, AB, Canada, T6G 2E9
* These authors contributed equally to this work

Acknowledgments: This work was supported by a Natural Science and Engineering Council of Canada (NSERC) grant # 249861 to CTD. TAW was additionally supported by an Izaak Walton Killam Memorial Graduate Scholarship, an Alberta Innovates – Technology Futures Graduate Scholarship and an NSERC Alexander Graham Bell Canada Graduate Scholarship – Doctoral (CGS D). We would like to acknowledge Trish Wolansky for significant contributions to this manuscript including ideas and data collection, in addition to Phillip de Guzman and Jon Kerber for contributing to data collection.

4.1 Abstract

Oscillatory synchronization is a pervasive neural phenomenon and is a likely important processing mode throughout the nervous system. In particular, hippocampal networks express different rhythms in conjunction with distinct behavioural states and hippocampal functions. Specifically, the hippocampus (HPC) demonstrates *theta* oscillations (3-12 Hz) during exploratory behaviour and REM sleep and slow oscillations (SO; ~1 Hz) during non-REM sleep; both have been implicated in different stages of memory. In this work we describe a novel oscillatory activity pattern that co-occurs with both theta and slow oscillations in the HPC and entorhinal cortex (EC). This slow rhythm (0.1-0.5 Hz), which we have called *iota*, while modestly apparent during spontaneous conditions, was prominently unmasked by inactivation of the medial septum (MS). The strongest power of iota occurred at stratum lacunosum moleculare (SLM) which is the site of termination of the direct temporoammonic pathway from EC layer III. Furthermore, HPC and EC iota were strongly coherent and iota-correlated multi-unit activity was most evident in EC layer III, suggesting that iota arises from a direct interaction between entorhinal and hippocampal networks. Interestingly, MS inactivation with lidocaine, but not muscimol, disrupted the hippocampal SO and produced a slow, iota-like but arrhythmic activity pattern that maintained a strong phase relationship with the neocortical SO. This last finding suggests that the hippocampal SO may also be dependent on non-EC inputs arriving at SLM via fibre systems passing in close proximity to the MS region. Overall, these findings suggest that iota is integrated with both theta and SO generating systems to further influence information processing within this circuit both within and across brain states.

4.2 Introduction

Rhythmic synchronization is a pervasive and ubiquitous property of neural activity across species and has been suggested to be fundamental to the operation of the nervous system (Buzsaki et al., 2013). Frequencies of oscillatory activity in neural systems span several orders of magnitude; from slow seasonal and circadian fluctuations (≤0.00001 Hz) to fast ripple oscillations (≥200 Hz). Traditional measurements of cerebral activity patterns, in terms of the range of frequencies recorded, and the frequency bands analyzed, have been strongly influenced by historical tradition and technical capabilities. While slow (<0.5 Hz) rhythms (often referred to as DC or near-DC potentials) have often been filtered out of AC-coupled field recordings, the relevance of these oscillations to neural function has been of increasing interest (Palva and Palva, 2012). For example, infra-slow (0.01-0.1 Hz) EEG fluctuations have been correlated with blood-oxygen levels in resting state networks (Hiltunen et al., 2014), and can predict behavioural performance on a signal detection task (Monto et al., 2008).

Oscillations in the hippocampus have been of particular interest because of the structure’s role in episodic/spatial learning and memory (Scoville and Milner, 1957; O'Keefe and Dostrovsky, 1971; Nadel and Moscovitch, 2001; Eichenbaum and Cohen, 2014; Schiller et al., 2015). Not only have oscillatory activity patterns been suggested to be important for memory encoding in this circuit (Hasselmo et al., 2002; Kunec et al., 2005; Hasselmo and Stern, 2014), but also for consolidating these memories during offline situations like slow-wave sleep (Buzsaki, 1989; Girardeau et al., 2009; Born, 2010; Ego-Stengel and Wilson, 2010). While theta oscillations (3-12 Hz) are prominent during spatial navigation and during REM sleep (Bland et al., 1979; Bland, 1986; Buzsaki, 2002; Vertes et al., 2004; Buzsaki and Moser, 2013), the hippocampal slow oscillation (SO, ~1 Hz) is a prominent pattern expressed during non-REM sleep and is dynamically coordinated with the large amplitude SO in the neocortex (Steriade et al., 1993b; Wolansky et al., 2006). Both of these oscillations show maximal power at stratum lacunosum moleculare (SLM) of the CA1 hippocampal subfield, which is the termination zone for both entorhinal and nucleus reuniens (thalami) projections (Wouterlood et al., 1990; Dolleman-Van der Weel et al., 1997; Vertes et al., 2004).

Slower hippocampal oscillations have also been described, including ultra-slow (<0.025 Hz) alternations of hippocampal network excitability (Penttonen et al., 1999), and a 0.03-0.3 Hz rhythmicity in the co-modulation of hippocampal and neocortical activity during slow wave sleep (Sirota and Buzsaki, 2005). In the present study we describe an infra-slow (0.1-0.5 Hz) hippocampal activity that is present across states but is unmasked during the activated state by temporary inactivation of the medial septum. We show evidence that this rhythm, which we call iota, is coupled to faster activity like SO and theta, and likely represents an interaction between entorhinal and hippocampal circuits.

4.3 Methods

All experimental procedures conformed to the guidelines established by the Canadian Council on Animal Care and were approved by the University of Alberta Biosciences Animal Care and Use Committee.

4.3.1 Animals and surgery

Experiments were performed on 42 male Sprague-Dawley rats weighing 266 ± 11 g (mean ± SEM). Animals were placed in an enclosed chamber with 4% isoflurane in 100% O_2 until the loss of righting reflexes, at which point a surgical plane of anaesthesia was maintained through delivery of 1.5-2.5% isoflurane via a nose cone while a catheter was inserted in the jugular vein. Isoflurane was then discontinued while anaesthesia was maintained by slow administration of urethane (0.67-0.8 g/mL) to a final dose of 1.73 ± 0.04 g/kg. Final urethane dose was based on the lack of withdrawal to toe pad pressure, and lack of reactivity to being placed in a stereotaxic frame (Model 900; David Kopf Instruments, Tujunga, CA). Core body temperature was maintained at 37°C using a servo-controlled heating pad connected to a rectal probe (TR-100; Fine Science Tools, Vancouver, BC, Canada). A subcutaneous injection of atropine methyl nitrate (0.05 mg/kg) was administered to reduce respiratory secretions. A monopolar electrode (Teflon-coated stainless steel wire, bare diameter: 125 µm; A-M Systems, Carlsborg, WA) was implanted in the frontal cortex (all coordinates relative to Bregma: anterior-posterior (AP): +2.5 mm; medial-lateral (ML): +1.0 to +1.2 mm) in either superficial (dorso-ventral (DV): -0.2 to -0.25 mm) or deep (DV -1.5 to -2 mm) cortical layers. This protocol allowed for spontaneous alternations between activated and deactivated forebrain states (Wolansky et al., 2006; Clement et al., 2008).

In a subset of animals (n=24), a 16-channel linear multisite electrode (silicon probes from Neuronexus, Ann Arbor, Michigan, or a multi-site platinum-iridium electrode from Plexon, Dallas, Texas) was implanted in the dorsal hippocampus (AP -3.1 to -3.5 mm, ML 2.1 to 2.6 mm, DV -3.1 to 4.0 mm). The recording depth was adjusted to include at least 2 channels below the maximum theta amplitude and 4 channels above the theta phase reversal. Data from one animal were removed following histological assessment due to a probe position medial to CA1. In a subset of these animals, a 30-gauge stainless steel infusion cannula was also implanted in the medial septum (AP +0.5 mm, ML 0.0 mm, DV 5.0-6.0 mm) for infusion of lidocaine (10 nM, n=4) or muscimol (10 nM, n=3). For infusions, cannulae were connected with PE-50 tubing (Fisher Scientific, Ottawa, Canada) to a 10 µL Hamilton microsyringe loaded on a microinfusion pump (Model KDS100, KD Scientific Inc., Holliston, MA). Following the acquisition of baseline recordings, infusions of 1 μL were made over a period of 1 minute. The location of infusion was evaluated by histological assessment as well as electrophysiological measures, as this infusion should abolish theta oscillations in the hippocampus (Smythe et al., 1991; Lawson and Bland, 1993; Dickson et al., 1994). In one case the infusion hit the lateral instead of the medial septum and these data were removed from subsequent analyses.

In another group of animals (n=18), a monopolar electrode was implanted in the dorsal hippocampus, targeting the hilus (AP -3.1 to -3.5 mm, ML 2.1 to 2.6 mm, DV -3.1 to 3.5 mm). Final electrode position was based on the maximal amplitude of theta oscillations in the local field potential (LFP). A 16-channel linear multisite probe was then implanted in the medial entorhinal cortex (EC) perpendicular to the cell layers. This was achieved by implanting the probe above the contralateral hemisphere (AP -4.0 mm, ML +4.0 mm) with a 40° angle below horizontal, and advancing the probe 8.0 to 9.5 mm from the surface. Proper electrode placement was evaluated by histological assessment as well as by electrophysiological measures (maximal theta amplitude in superficial layers; phase reversal of theta activity at layer II, (Alonso and Garcia-Austt, 1987; Dickson et al., 2000)). Based on these criteria, the data from 7 animals were removed from further analysis.

4.3.2 Data collection and histology

Electrophysiological recordings were referenced to stereotaxic ground. Monopolar electrode signals were amplified at a gain of 1000 and filtered between 0.1 Hz and 10 kHz using a differential AC amplifier (Model 1700, A-M Systems). Linear multiprobe signals were passed through a headstage with unity gain (Plexon, Dallas, Texas), and then amplified at a gain of 1000 and filtered between 0.07 Hz and 8 kHz (PBX-2 amplifier, Plexon). Signals were then digitized at a minimum sampling rate of 1000 Hz with anti-alias filtering at ½ of the sampling rate using a 1322 Digidata A/D board (Molecular Devices, Union City, CA) connected to a personal computer for data acquisition in Axoscope (Molecular Devices, Union City, CA).

Following data collection, animals were perfused transcardially with physiological saline followed by 4% paraformaldehyde. Brains were extracted and stored for histological processing in a 4% paraformaldehyde/30% sucrose solution. After a minimum of 24 hours, tissue was frozen with compressed CO_2 and sliced at a thickness of 48μm using a rotary microtome (Model 1320, Leica, Vienna, Austria). Slices were mounted on gel-coated slides and allowed to dry prior to staining with thionin and assessment of electrode and cannula placements.

4.3.3 Data Analysis

Data were analyzed using a combination of built-in and custom-written code in Matlab version 7.14 (The Mathworks, Natick, MA). Epochs were separated into activated (theta) states and deactivated (SO) states based on the presence or absence of theta oscillations in the hippocampal recordings. For lidocaine infusion experiments, due to the absence of theta oscillations, epochs were separated based on the absence or presence of the slow oscillation (SO) in the neocortical signal.

Power, phase and coherence spectra were computed using Welch's averaged periodogram method with a 6-second Hanning window and 2-second overlap. Spatial profiles of spectral activity were normalized across animals by aligning the theta reversal and theta power maximum. Current source density (CSD) was computed on multiprobe signals as the 2nd spatial derivative of the voltage traces (Freeman and Nicholson, 1975; Rodriguez and Haberly, 1989; Ketchum and Haberly, 1993).

Frequency co-modulograms were computed using a modified version of the modulation index (MI; Canolty et al., 2006; Kramer et al., 2008; Tort et al., 2010). For each pair of frequencies, the phase of the lower frequency and the amplitude of the higher frequency were computed using the angle (phase) and the absolute value (amplitude) of the respective wavelet transforms (Morlet wavelet, width = 6). The amplitude values were then binned as a function of phase (72 bins), and the deviation of this distribution from a uniform distribution (implying no modulation) was calculated using a modification of the Kullback-Leibler distance as described in Tort et al. (2010).

Independent component analysis (ICA) was used to isolate the local hippocampal signal at the layer of stratum lacunosum moleculare (SLM), likely arising from a combination of the temporoammonic (TA) pathway from the entorhinal cortex (EC) and the nucleus reuniens projection to CA1 (Wouterlood et al., 1990; Dolleman-Van der Weel et al., 1997). The runica algorithm was used to perform ICA decomposition (Makeig et al., 1996; Delorme and Makeig, 2004). This approach has been used previously to describe the underlying sources of the hippocampal LFP (Makarov et al., 2010; Makarova et al., 2011; Fernandez-Ruiz et al., 2012b; Fernandez-Ruiz et al., 2012a; Fernandez-Ruiz et al., 2013; Martin-Vazquez et al., 2013; Schomburg et al., 2014). We defined the SLM component (SLM*ic*) based on a maximal weighting at SLM and a reversal of phase at the same layer as the theta reversal. Furthermore, this was also the component with the greatest theta power.

For analysis of the consistency of phase-amplitude modulation across animals, the mean angle and resultant length were calculated using the CircStat Matlab toolbox for circular statistics (Berens, 2009), and second-order circular statistics were then used to assess group means (Zar, 2010).

4.4 Results

4.4.1 Iota rhythm under baseline conditions

Under baseline conditions, urethane-anaesthetized animals (n=16) cycled between an activated state dominated by hippocampal theta oscillations, and a deactivated state with strong forebrain (cortical and hippocampal) slow oscillations (SO) as we have previously described (Wolansky et al., 2006; Clement et al., 2008). However, during both states we could also observe a slower (0.1-0.5 Hz) hippocampal rhythm co-occurring with both SO and theta (Figure 4.1A). The intrahippocampal power profile of this slow rhythm, which we have called iota, was similar to the theta power profile, with a peak at SLM, however the power minimum was, on average, 100 µm ventral to the theta power minimum (Figure 4.1B, left panel). The coherence profile showed that iota was highly localized to SLM, with coherence dropping off markedly in superficial layers (Figure 4.1B, middle panel). Iota showed a near-180° reversal of phase at a similar depth to the theta phase reversal and the SO phase shift (Figure 4.1B, right panel). During both SO and theta states, the iota rhythm modulated the amplitude of faster frequencies in the 3-40 Hz range (Figure 4.1C). A spectral peak at ~0.3 Hz was present during both SO and theta states in some animals (Figure 4.1D), although this peak was not always present.

Interestingly, we have observed this modulation of faster frequencies by 0.1-0.5 Hz phase in our prior work as well (Figure 3.6 B&C; Chapter 3). In addition, we have also observed a slowing of the hippocampal SO with respect to the neocortex

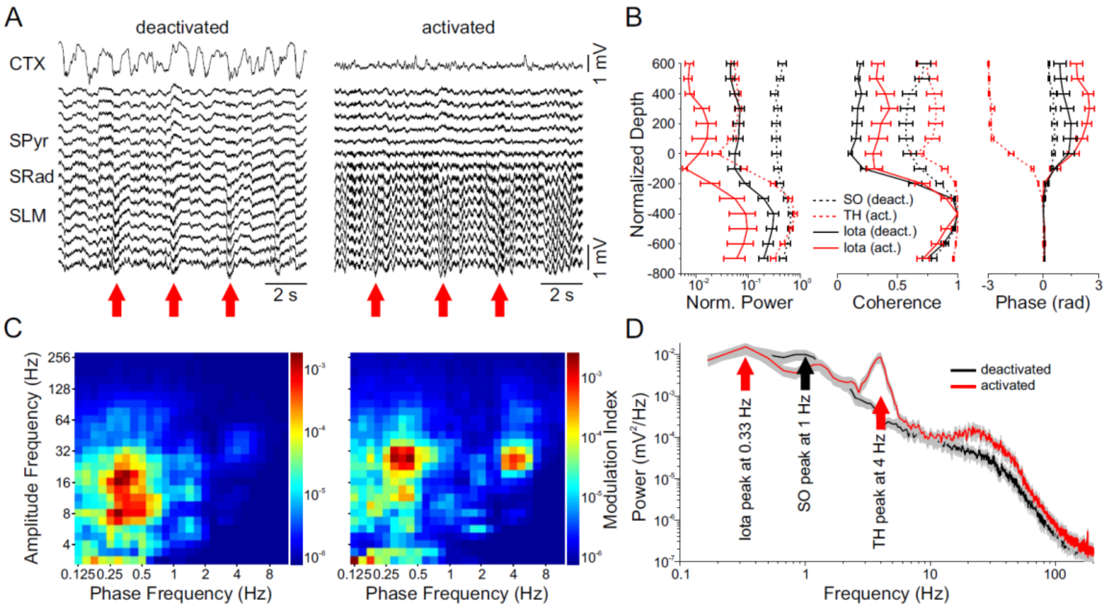

Figure 4.1 Iota (~0.1-0.5 Hz) rhythm co-expressed with SO and theta rhythms in the hippocampus

(A). Representative recordings from the frontal cortex (top trace) and hippocampus during deactivated (left panel) and activated (right panel) states under urethane anaesthesia. Red arrows mark the emergence of the iota rhythm at ~0.3 Hz during both states. (B). Power (left), coherence (middle) and phase (right) profiles of SO, theta and iota activity, with deactivated states shown in black and activated states in red. Averages were computed by aligning the theta reversal (normalized depth = 0) and the maximum theta power (normalized depth = -400). (C). Phase-amplitude comodulograms for a representative animal, demonstrating that the ~0.1-0.5 Hz iota frequency is modulating the amplitude of faster rhythms during both the deactivated (left) and activated (right) states. (D). Power spectrum for the same animal shown in (A), showing peaks at SO (~1 Hz) and iota (~0.3 Hz) during the deactivated state (black), as well as theta (4 Hz) and iota (~0.3 Hz) during the activated state (red). The 95% confidence intervals of the spectral estimates are shown in grey.

due to the periodic skipping of SO cycles (Figure 3.9; Chapter 3). In both cases this slow frequency was observed most prominently by isolating the presumed synaptic inputs to SLM using independent component analysis (ICA; see Chapters 2 and 3; Makarov et al., 2010; Benito et al., 2014). This approach separates a mixed signal such as the LFP into its underlying sources by maximizing their statistical independence (Hyvarinen and Oja, 2000). Across animals (n=16), five components were consistently separated (Figure 4.2A and B), and were putatively identified based on their spatial profiles in comparison to the known synaptic inputs to the dorsal hippocampus, in addition to a volume-conducted signal with a flat spatial profile (Figure 4.2B). The SLM*ic* had a peak activation at SLM and a phase reversal near the theta reversal, matching the spatial profile of iota activity (Figure 4.2B, cyan). This component likely reflects synaptic input terminating at this layer from the entorhinal cortex via the temporammonic pathway in addition to potential input from the nucleus reuniens (Wouterlood et al., 1990; Dolleman-Van der Weel et al., 1997; Vertes et al., 2004). During both deactivated (Figure 4.2C) and activated (Figure 4.2D) states, the SLM*ic* had the strongest iota power.

When observing the time series of the SLM*ic* across transitions from a deactivated to an activated state (Figure 4.3A), we noted several dynamics. During the deactivated state, there were epochs where activity in the SLM*ic* was much slower than the neocortex (Figure 4.3B*i*), and these epochs were associated with a peak at iota frequency in the power spectrum (Figure 4.3C*i*). In contrast, there were also epochs in which the SLM*ic* followed the neocortical SO closely, and these were associated with a strong peak at ~1 Hz in both the SLM*ic* and neocortical power spectra (Figure 4.3B*ii* and C*ii*). Just prior to the transition to the activated state, activity in the SLM*ic* was again much slower than the neocortical SO, and this slow iota activity continued as theta oscillations began to emerge (Figure 4.3B*iii* and C*iii*).

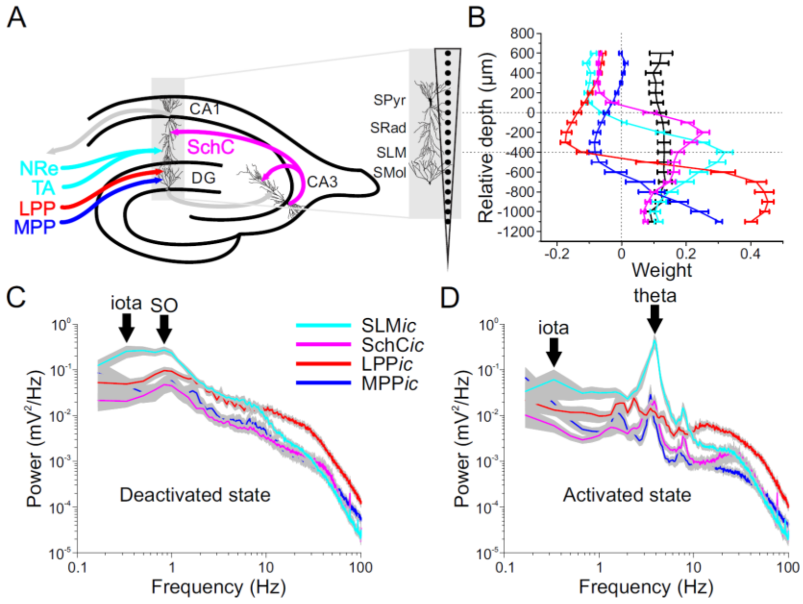

Figure 4.2 Iota is most prominent in SLM-targeting synaptic inputs

(A). Schematic representation of the dorsal hippocampus highlighting the laminar organization of the major afferent pathways. The medial and lateral perforant pathways (MPP and LPP) project to the middle and outer thirds of the dentate molecular layers (DMol). The Schaffer collateral pathway (SchC) projects to stratum radiatum (SRad) of CA1. Both the entorhinal cortex, via the temporoammonic (TA) pathway, and the nucleus reuniens, project to SLM. The target position of the multiprobe with respect to the laminae is enlarged on the right. (B) Spatial profile of ICA weightings at each electrode position, averaged across animals (n=16). Components were identified based on characteristics of their spatial profiles in relation to the known synaptic inputs shown in (A). Blue – MPP*ic*; Red – LPP*ic*; Magenta – SchC*ic*; Cyan – SLM*ic* (named based on termination zone instead of pathway because both TA and nucleus reuniens fibres project to SLM); Black – volume-conducted signal (note the flat profile, unlike the other components). For more details, see Chapters 2 and 3. (C). Average power spectra (n=16 animals) of each component during the deactivated state (2 minute sample). All spectra were normalized by the total power of the raw LFP at SLM during the deactivated state. Note the peak at 0.3 Hz in the SLM*ic* (cyan) in addition to the ~1 Hz SO peak. (D) Average power spectra (n=16) for the activated state (2 minute sample), normalized as in (C). Note the peak at 0.3 Hz in the SLM*ic* (cyan) in addition to the ~4 Hz theta peak.

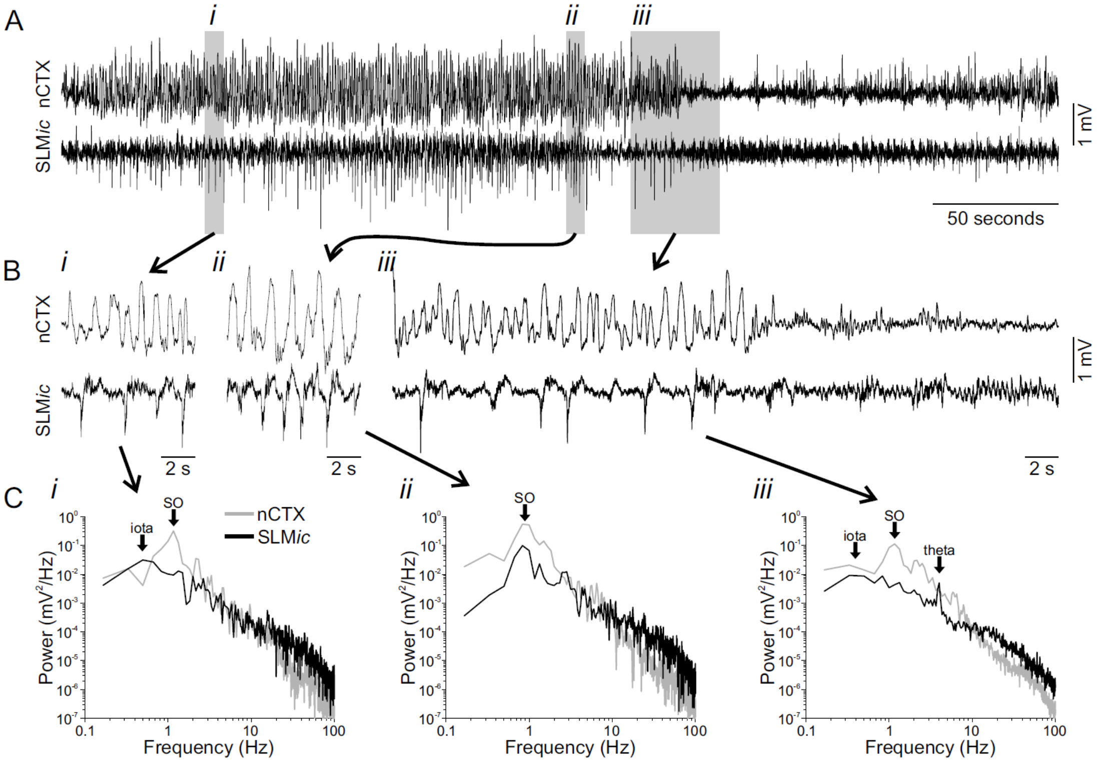

Figure 4.3 Iota activity across brain state transitions

(A). Neocortical (nCTX, top) and SLM*ic* (bottom) signals across the evolution from a deactivated to an activated state. (B). Expansion of signals marked by shaded regions in (A). (*i*). Early deactivated state, the SLM*ic* is slower than the neocortical SO. (*ii*). Late deactivated state, the SLM*ic* and the nCTX both show a strong ~1 Hz SO. (*iii*). At the transition from deactivated to activated, the SLM*ic* slows down and the slow iota rhythm continues as theta oscillations emerge. (C). Power spectra for 30 second windows centered on epochs shown in (B). (*i*) The nCTX has a ~1 Hz peak but the SLM*ic* has a slower iota (~0.5 Hz) peak. (*ii*) Both the nCTX and the SLM*ic* have peaks at ~1 Hz. (*iii*). The nCTX has a peak at ~1 Hz while the SLM*ic* has a peak at iota (~0.3 Hz) and a small theta (~4 Hz) peak.

4.4.2 Iota rhythm unmasked by medial septal inactivation

Iota was visible in the spontaneous LFP traces during activated (theta) states to varying degrees across animals. In some cases iota was only seen at the transition from SO to theta (Figure 4.3 panels *iii*), while in others cases it lasted throughout the entire theta epoch. The average spectral profiles (Figure 4.1B, n=16) suggested that iota was a common feature of hippocampal activity across animals even in cases in which it wasn't necessarily observable in the raw traces. We assumed that the prominent and large-amplitude theta activity tended to mask the slower iota. We therefore sought to uncover iota by abolishing theta oscillations through temporary inactivation of the medial septum using local injections of lidocaine. This manipulation has been shown previously to profoundly diminish hippocampal and entorhinal theta oscillations (Dickson et al., 1994), and has also been shown to reduce the power of the local field during non-theta states (Smythe et al., 1992; Lawson and Bland, 1993), although this latter effect has been less well studied.

Following lidocaine infusions into the medial septum, we found a near-complete elimination of theta rhythmicity at SLM, while neocortical activity remained unaltered (Figure 4A*i*-*ii*). In the place of theta oscillations, a striking activity pattern emerged, characterized by periodic events occurring at about 0.1-0.5 Hz (circled in Figure 4A*ii*). This iota activity was even more prominent in the SLM*ic* (Figure 4A*ii*, bottom panel). During the deactivated state, there was a slight reduction in amplitude of the raw hippocampal LFP (Figure 4A*iii*-*iv*, middle panels), but a dramatic reduction in activity of the SLM*ic* (Figure 4A*iii*-*iv*, lower panels). In place of the typical hippocampal SO, we found periodic waveforms similar to the iota activity seen during post-inactivation theta states (compare Figure 4A*ii* and *iv*, circled events). The average waveforms of iota events in the SLM*ic* following septal inactivation were

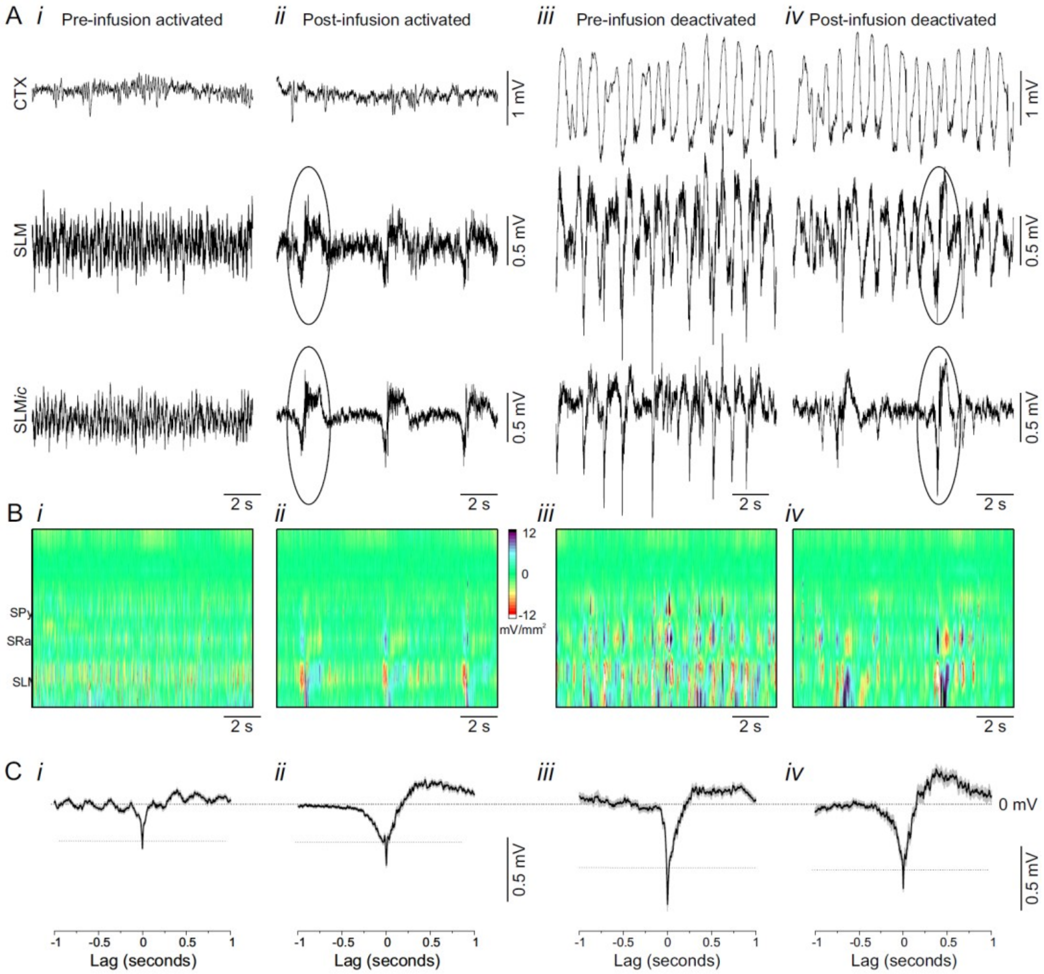

Figure 4.4 Inactivation of the medial septum with lidocaine reveals iota rhythm in the hippocampus

(A). Representative examples of cortical (top), hippocampal SLM (middle) and the ICA-separated SLM*ic* (bottom) traces during the activated state pre- and post- medial septal lidocaine infusion (*i*-*ii*) and during the deactivated state pre- and post- infusion (*iii*-*iv*). Typical waveforms seen in the hippocampus after septal inactivation are circled to highlight the similarity across both states. (B). CSD of hippocampal activity shown in (A) to assess current flow. Note the large decrease in activity during the deactivated state following septal inactivation, as well as the location of current sinks at SLM. (C). Average waveforms of activity patterns seen in (A) over full epochs for each state (~2 minutes). Averages were triggered on negative peaks exceeding the thresholds marked by horizontal lines. Pre-infusion activated: n = 42 events; Pre-infusion deactivated: n = 18 events; Post-infusion activated: n = 25 events; Post-infusion deactivated: n = 14 events.

quite similar during both activated and deactivated states (Figure 4.4C*ii* and *iv*). Average waveforms for spontaneous activity are shown for comparison (Figure 4.4C*i* and *iii*). The averages for the activated state were triggered on the largest amplitude negative deflections (such as those seen in Figure 4.1A, red arrows) and not on every theta cycle.

Analysis of extracellular current flow using CSD confirmed the above findings. First, the depth of the maximal sinks associated with iota during the activated state occurred at SLM (Figure 4.4B*ii* and *iv*). Second, there was a marked absence of SO-related (~1 Hz) sinks at SLM following septal inactivation (Figure 4.4B*ii*). The ~1 Hz activity that is still seen in the hippocampal LFP post-infusion (Figure 4.4A*ii*, middle panel), therefore likely represents the volume-conducted SO signal from the overlying cortex. In line with these findings, the power profiles for SO and theta were both nearly flat following septal inactivation, and the ~180° phase reversal of theta activity was eliminated (Figure 4.5A and C). The profiles of iota during the activated state following septal inactivation showed a global increase in power but no change in the shape of the power profile or in the magnitude or depth of the phase reversal (Figure 4.5B).

The examples shown in Figure 4.4A suggest that the activity patterns of the SLM-targeting inputs are very similar during both activated and deactivated states following lidocaine infusion in the medial septum. However, when we looked at longer epochs pre- and post- infusion it was clear that there were important differences (Figure 4.6A and B; boxes represent epochs shown in Figure 4.4). Notably, while the iota events seen post-infusion during the activated state occurred rhythmically at a frequency of ~0.1-0.5 Hz, the events during the deactivated state were more infrequent and appeared non-rhythmic. We assessed the rhythmicity of iota in the post-infusion activated state by looking at the autocorrelations of the

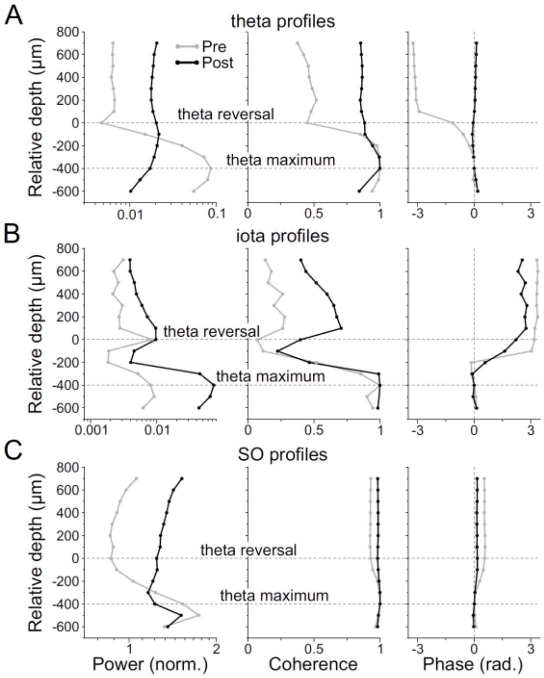

Figure 4.5 Depth profiles of spectral activity pre- and post- septal inactivation

(A). Power (left), coherence (middle) and phase (right) profiles of theta activity in the hippocampus pre- (grey) and post- (black) septal inactivation for the representative example shown in Figure 2. Profiles were calculated on a 60 second sample of the activated state for both pre- and post- infusion conditions. (B). As in (A) for the iota (0.5 Hz) frequency. (C). As in (A) for the SO frequency, calculated on a 60 second sample of the deactivated state for both pre- and post-infusion conditions.

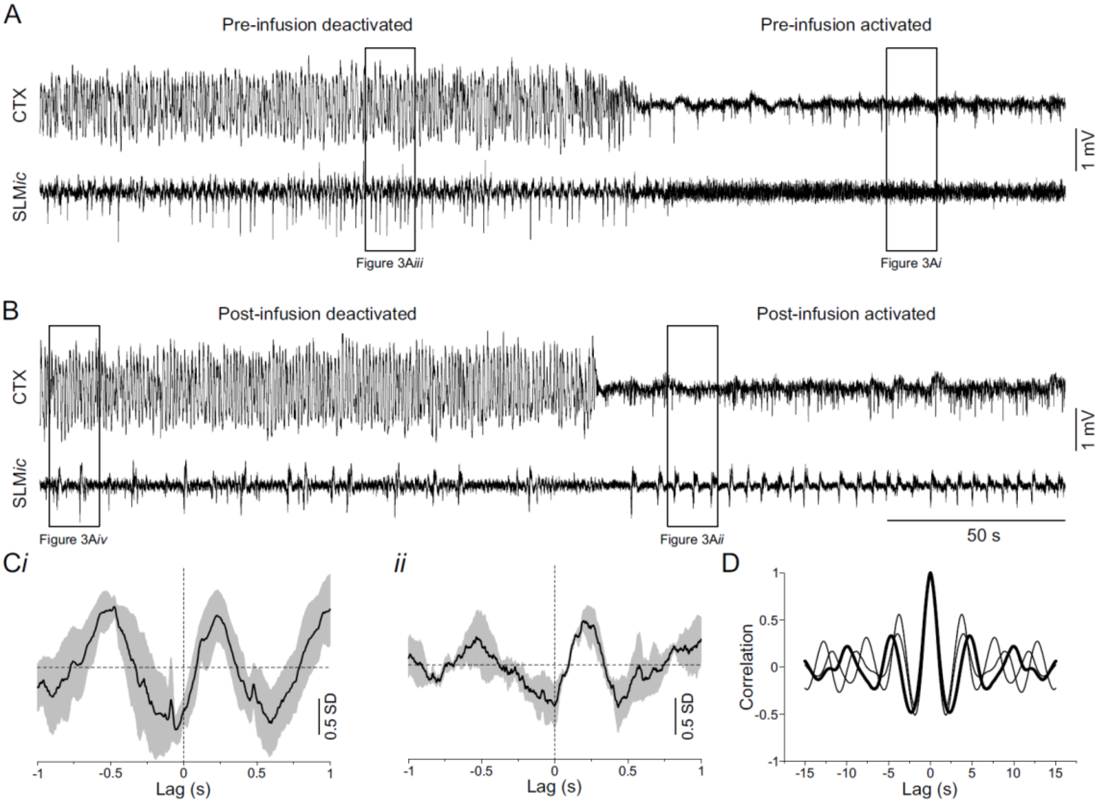

Figure 4.6 Rhythmicity and coordination of post-infusion hippocampal activity

(A). Pre-infusion spontaneous activity in the neocortex (top) and in the SLM*ic* (bottom) during both deactivated (left) and activated (right) states. (B) Post-infusion activity of the neocortex (top) and the SLM*ic* (bottom) to highlight the rhythmicity of iota during the activated state following septal inactivation but the lack of rhythmicity during the deactivated state. Boxes highlight the epochs shown in Figure 3A and B. (C). Iota-triggered cortical signal during the deactivated state for the representative example (*i*) and the group average (*ii*, n=3). Events were triggered at the trough of the waveform in the hippocampus. (D). Autocorrelation of the 1-second smoothed RMS of the hippocampal signal during the activated state following septal inactivation. Representative example from Figure 3 is shown in bold.

smoothed RMS of the SLM*ic* signals (Figure 4.6D). In all three animals there was a strong peak at a lag of 3-5 seconds, corresponding to an iota frequency of 0.2-0.3 Hz. Interestingly, while the activity during the post-infusion deactivated state did not show the same rhythmicity, we found a strong phase-relationship with the very rhythmic SO in the neocortex. Iota events occurred near the trough of the neocortical SO, corresponding to the peak of the UP/ON-state (SLM*ic*-event-triggered averages of the neocortical signal: Figure 4.6C*i* (representative animal), and Figure 4.6C*ii* (group average)).

Across animals, theta power decreased and iota power increased during the activated state following septal inactivation (Figure 4.7A, n=3). This was true for both the raw LFP and the SLM*ic*, while the power of the neocortical signals were unchanged. In all three animals, the decrease in theta power and the increase in iota power in both the raw LFP and the SLM*ic* were significant (based on no overlap of the 95% confidence intervals of the spectral estimates). During the deactivated state, there was a large decrease in SO power in the SLM*ic* (Figure 4.7B), while both the neocortical and the raw LFP spectra were unchanged. In all three animals, the decrease in SO power in the SLM*ic* following septal inactivation was significant.

Interestingly, we found a striking dissociation between the effects of lidocaine and muscimol infusions into the medial septum. While both lidocaine (n = 3) and muscimol infusions (n=3) significantly decreased theta power during the activated state (Figure 4.8A), muscimol infusions had no observable effect on SO power in the SLM*ic* during the deactivated state (Figure 4.8B). We did note that in the average spectra, the increase in iota power during the activated state following muscimol infusions was less pronounced than the increase following lidocaine infusions (compare Figures 7A and 8A). However, in 2/3 animals there was a significant increase in iota power following muscimol infusion. In the third animal, iota power

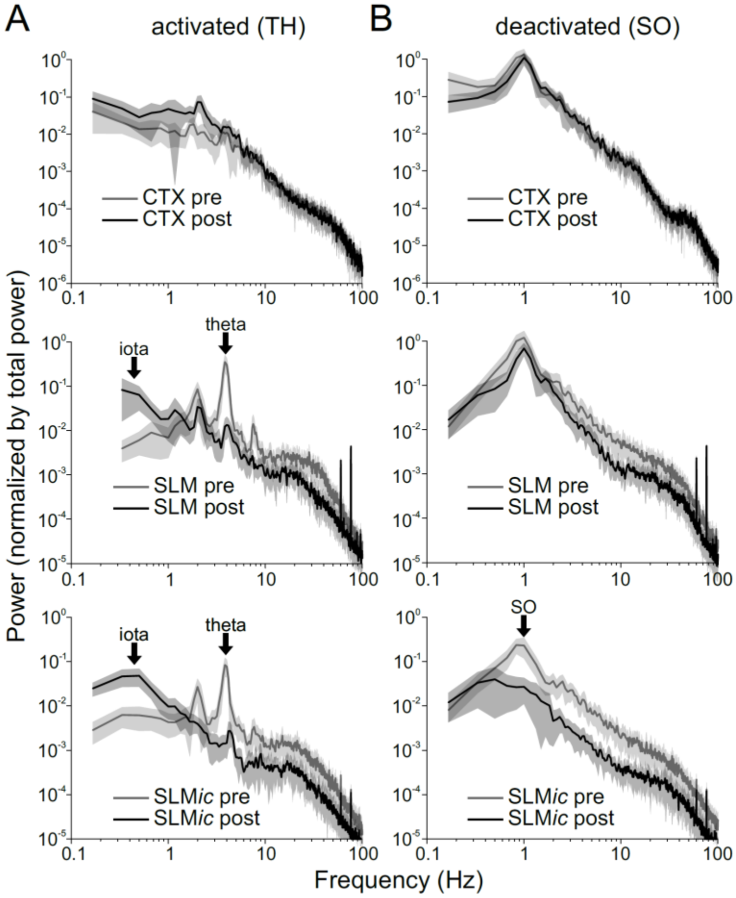

Figure 4.7 Group mean power spectra pre- and post- septal lidocaine infusions

(A). Mean ± 95% confidence intervals for cortical (top), hippocampal SLM (middle) and ICA-separated SLM*ic* (bottom) spectra during the activated state both pre- (grey) and post- (black) infusion of lidocaine in the medial septum. The confidence intervals for the post-infusion SLM spectrum overlapped with 0 at 0.167 Hz and therefore this frequency could not be shown on the logarithmic scale. Spectra were calculated on 60-second samples from the activated state. (B). As in (A) for the deactivated state pre- and post- infusion. All spectra were normalized based on the total power during the deactivated state pre-infusion.

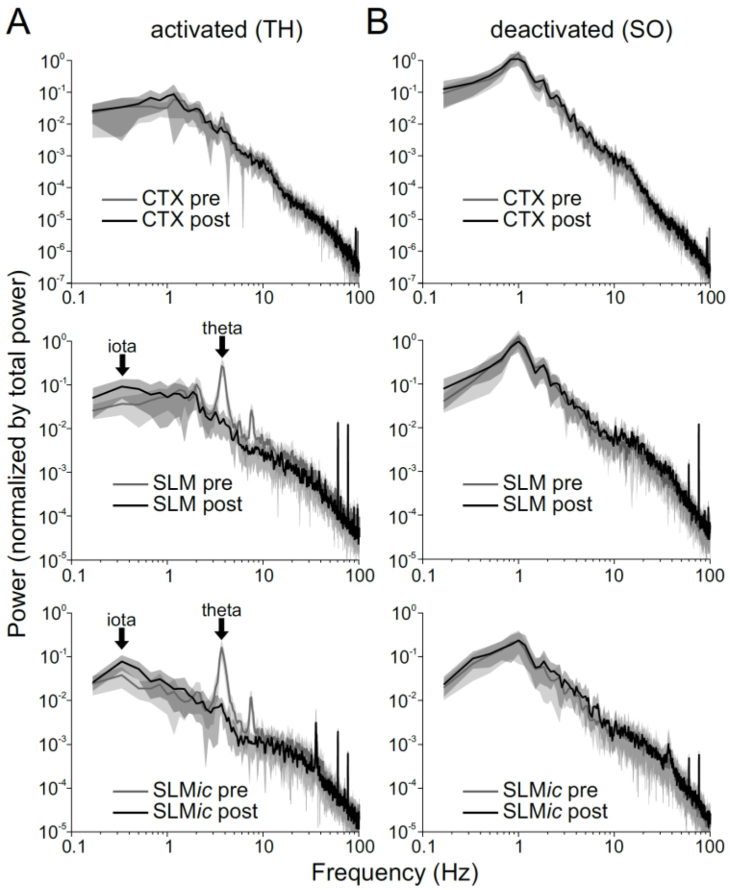

Figure 4.8 Group mean power spectra pre- and post- septal muscimol infusions

(A). Mean ± 95% confidence intervals for cortical (top), hippocampal SLM (middle) and ICA-separated SLM*ic* (bottom) spectra during the activated state both pre- (grey) and post- (black) infusion of muscimol in the medial septum. Spectra were calculated on 60-second samples from the activated state. (B). As in (A) for the deactivated state pre- and post- muscimol infusion. Note the differences between the effects of lidocaine (Figure 4) and muscimol during the deactivated state. All spectra were normalized based on the total power during the deactivated state pre-infusion.

was already high prior to infusion, and did not increase further. Indeed, we observed that the power of iota during spontaneous activity was quite variable between animals and sometimes even within the same animal across different epochs.

4.4.3 Iota is coordinated across entorhinal and hippocampal networks

The findings that both the local maximum power and CSD sinks related to iota were located at SLM, and the strong iota activity in the SLM*ic*, suggested that this rhythm may involve the entorhinal cortex, which projects directly to SLM through the temporoammonic pathway. We therefore recorded activity across multiple layers of the medial entorhinal cortex while recording simultaneously from the hippocampus. We found that periods of spontaneous iota in the hippocampus were associated with large fluctuations in the power of theta within the entorhinal cortex (Figure 4.9A*i*-*iv*). This relationship was assessed through hippocampal phase-entorhinal amplitude comodulation (Figure 4.9B). The phase relationship is shown for a representative animal (Figure 4.9C), and for the group (Figure 4.9E, n=11; mean angle 258°, r = 0.029, $F_{(2,9)} = 4.74$, $p<0.05$). The mean iota-phase-triggered average of SLM theta power (Figure 4.9D, n=11) also showed a significant relationship between iota phase and theta amplitude.

We had noted in the spontaneous hippocampal data that the influence of iota was most clear during transitions between states (Figure 4.3). When we looked at activity in the superficial entorhinal layers just before a transition from the deactivated to the activated state, we saw clear evidence for a slow iota rhythm with a frequency of ~0.3 Hz (Figure 4.10A). The iota activity in the entorhinal cortex (middle trace) was clearly related to hippocampal activity (bottom trace). In fact, when we overlaid the two signals (Figure 4.10B), the EC activity also appeared to precede the hippocampal activity. When we triggered on the negative peaks of iota

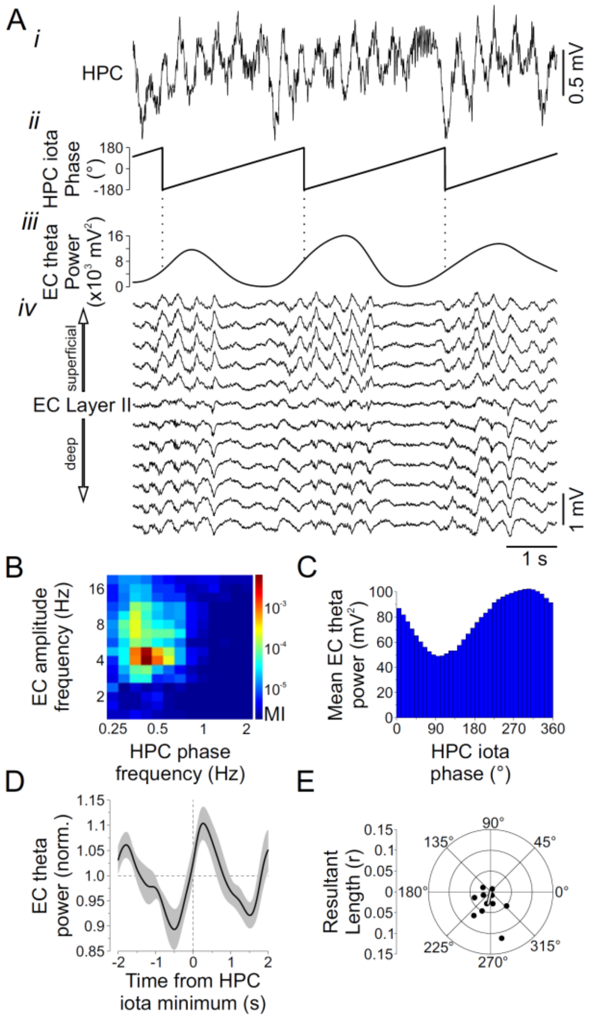

Figure 4.9 Fluctuations of EC theta power as a function of hippocampal iota phase

(A). Representative example of simultaneously recorded signals in the hippocampus at SLM (*i*) and the EC across superficial and deep layers (*iv*) during iota recorded during the activated state, showing a relationship between hippocampal iota phase (*ii*) and EC iota power (*iii*). (B). Comodulogram of hippocampal phase and entorhinal amplitude for the representative example shown in (A), showing a modulation of EC theta (~4 Hz) power by hippocampal iota (~0.5 Hz) phase. (C). Distribution of EC theta power as function of hippocampal theta phase for the same representative example, showing a mean angle of 283°. (D). Hippocampal iota-triggered EC theta power group average (n=11). (E). Group data for mean angles evaluated as in (C), with a significant group mean angle of 258° (r = 0.029, $F_{(2,9)}$ = 4.74, p<0.05).

waves in the superficial EC, the average hippocampal signal showed a lag of 9 ms (Figure 4.10C). The cross-correlation of EC and hippocampal activity also suggested that EC iota was leading hippocampal iota (Figure 4.10D, inset, lag -12 ms). Across animals, when there was a clear iota rhythm in the EC (n=4), the hippocampus always followed the EC and the average lag was 13.5 ± 1.9 ms (based on the EC-iota triggered hippocampal signal).

The hippocampal spectrum during this transition state showed a modest peak in the iota range (Figure 4.10E), but the EC spectrum did not show a strong peak. However, when we looked at the coherence between the two signals there was strong coherence at 0.3 Hz (Figure 4.10F). This HPC-EC coherence was high (above 0.9) and was maximal in the superficial layers of the EC, with a dip in coherence 100 µm below the theta reversal/theta coherence dip (Figure 4.10G). CSD analysis revealed strong iota-related sink/source pairs, with the sinks in the superficial layers of the EC and the sources occurring below the theta reversal (Figure 4.10H). Multi-unit activity (>500 Hz) was also iota-modulated. The maximum iota power of the smoothed RMS of the multiunit activity occurred 100 µm below the theta reversal, corresponding to layer III (Figure 4.10I). Finally, the average iota-triggered CSD and multiunit RMS envelope are shown in Figure 4.10J, below the average EC iota waveform. The mean amplitude of the multiunit RMS envelope at zero-lag from the iota trough was largest at layer III, with a smaller peak in layer II (Figure 4.10J*iii*).

4.5 Discussion

We have described for the first time a slow (0.1-0.5 Hz) hippocampal rhythm – iota – that co-occurs with both theta and the SO across activated and deactivated forebrain states, respectively, but that is most prominent during transition states and is unmasked when theta oscillations are abolished by temporary inactivation of

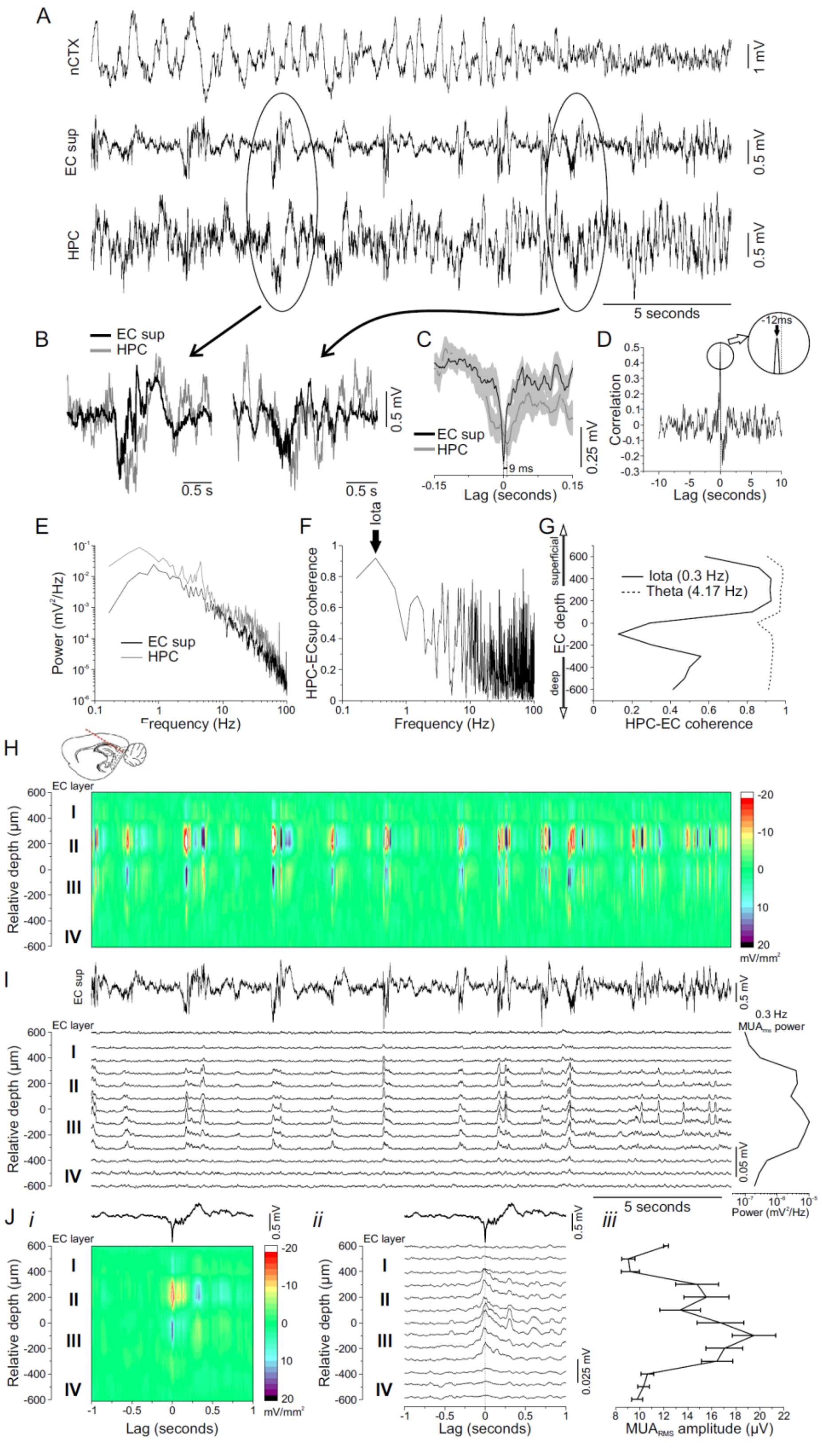

Figure 4.10 Coordination of iota in entorhinal and hippocampal circuits

Figure 4.10 Coordination of iota in entorhinal circuits.

(A) Simultaneous signals from the neocortex, superficial EC and hippocampus during the transition from a deactivated to an activated. Note the occurrence of a slow iota-frequency activity pattern in the EC signal prior to the transition to theta activity. (B) Overlay of EC and HPC signals during iota events circled in A. (C) Average iota waveforms triggered on the negative peak of iota in the superficial EC. The HPC iota followed the EC by 9 ms in this subject. (D). Cross-correlation of EC and HPC signals shown in A, showing maximal correlation at -12 ms, suggesting that the EC is leading the HPC during iota. (E). Power spectrum of the HPC and EC signals shown in A. (F). Coherence spectrum of HPC and EC signals, showing a strong (>0.9) coherence peak at iota frequency (0.3 Hz). (G). HPC-EC iota coherence as a function of depth in the EC. Depth is relative to the phase reversal of theta activity, which occurs at layer II (Alonso and Garcia-Austt, 1987; Dickson et al., 2000). The coherence profile for theta is shown as a reference, with a dip in coherence occurring at 0μm (i.e. corresponding to the theta phase reversal). The iota coherence dip is 100 μm deeper. (H). CSD of EC activity shown in A. Note strong sink/source pairs related to the iota rhythm. Inset shows angled approach to reach the entorhinal cortex (see Methods section). Approximate layers within the EC are based on the theta reversal as well as the magnitude of multi-unit activity. (I) RMS of the >500 Hz multi-unit activity smoothed with a 50 ms window. Raw signal from the superficial EC is reproduced from panel A as a reference. Note the strong multi-unit activity localized mainly to layers II and III. Right panel shows depth profile of iota power of the smoothed MUA_{RMS} signals, showing maximal iota-modulation of multi-unit activity in layer III. (J). Average iota-triggered (*i*) CSD and (*ii*) multiunit activity (smoothed RMS), with the average iota waveform shown above for reference. (*iii*) Mean amplitude of the iota-triggered MUA at zero-lag from the negative iota peak. Note the largest amplitude in layer III.

the medial septal region. Iota, theta, and the SO are all maximal at stratum lacunosum moleculare (SLM) in CA1, which receives inputs from both the EC via the temporoammonic pathway and from the nucleus reuniens. Accordingly, prominent iota activity was also found in the EC during transitions from the deactivated to the activated state. This iota activity was coherent with iota in the HPC, and was associated with iota-frequency CSD sinks in the superficial EC layers, and multiunit activity that was maximal at EC layer III. Following the transition to the activated state, the amplitude of theta in the EC was modulated by the phase of iota in the HPC.

Our second major finding was a profound effect of septal inactivation with lidocaine on the hippocampal SO. While others have found reductions in LFP power during deactivated states following septal inactivation (Smythe et al., 1992; Lawson and Bland, 1993), to our knowledge we are the first to describe that inactivation of the medial septum significantly interferes with the hippocampal SO. This effect was seen most prominently in the ICA component that is maximal at SLM, presumably representing the synaptic inputs to this layer from either EC layer III or the nucleus reuniens. The effect was characterized by a dramatic slowing of spontaneous activity with periodic iota events that were phase-related to the neocortical SO.

Interestingly, muscimol infusions into the septum had no effect on the SO, despite still depressing theta activity during the activated state. Since muscimol presumably acts to suppress activity on cell bodies while lidocaine suppresses activity in both cell bodies and fibres, this suggests that fibre bundles coursing through or adjacent to the septal region may mediate the additional effects observed with the sodium channel blocker. Given that the nucleus reuniens projects to both SLM and layers I and III of the EC (Wouterlood et al., 1990; Vertes, 2015) and forms excitatory synapses on dendrites of CA1 pyramids (Wouterlood et al., 1990;

Bokor et al., 2002), disruption of this projection is one attractive possibility for mediating the effects described here. Both hippocampal and nucleus reuniens single units are phase-modulated by slow wave activity induced by systemic ketamine injections, and LFPs in the two structures show strong coherence at slow frequencies (Zhang et al., 2012). Furthermore, optogenetic stimulation of SLM-targeting nucleus reuniens fibers at slow frequencies during awake behaviour alters online hippocampal function (Duan et al., 2015). Although the nucleus reuniens does target both the medial septum and the hippocampus (Bokor et al., 2002), the reuniens fibers targeting the HPC are thought to travel primarily in the cingulate bundle (Wouterlood et al., 1990). However, there is a suggestion that at least some fibers may travel in the fimbria/fornix (Saunders and Aggleton, 2007). Future experiments involving selective inactivation of the nucleus reuniens, or perhaps selective inhibition of SLM-targeting cells using optogenetic methods, will be critical for determining if this projection is mediating the effects described here.

We have previously found that periodic skipping of SO cycles in the hippocampus results in the slowing of the hippocampal SO with respect to the neocortex (see Figure 4.2 and Chapter 3 Figure 3.9). Given our present findings, one possibility is that this cycle skipping is due to an interaction between the cortical input at ~1 Hz and the intrinsic slower iota rhythm. However, unlike the effect seen during the activated state, lidocaine infusions in the medial septum disrupted rather than enhanced this intrinsic slow rhythm, and the remaining hippocampal activity lacked any clear rhythmicity. Nevertheless, this activity was still phase-modulated by the neocortical SO, suggesting that coordination between hippocampal and neocortical circuits was still present. In effect, the lidocaine infusions in the medial septum dramatically increased the rate of 'skipping' of cycles. This could be due to the disruption of the nucleus reuniens projection to the hippocampus, although the bulk of this pathway does not pass through the septal region, but through the cingulum and internal capsule which are both located more laterally (Wouterlood et al., 1990). Another possibility is that axons from brainstem nuclei such as the serotonergic neurons of the median raphé nucleus, were affected by the lidocaine infusion in the medial septum. These fibers ascend in the medial forebrain bundle and pass through the septum and on to the fornix (Moore and Halaris, 1975; McKenna and Vertes, 2001). It is possible that without this neuromodulatory input, the normal transmission of activity from the neocortex to the hippocampus is disrupted. It might also be the case that the median raphé provides a direct SO-pulsed input. Finally, another possibility is that the hippocampal SO may be mediated by some integration of the neocortex-EC-SLM pathway with the neocortex-nucleus reuniens-SLM pathway (Vertes et al., 2007; Varela et al., 2014), with both inputs necessary for coordination of the hippocampal SO with the neocortex. Indeed, it has been suggested that the rhinal cortices may serve an inhibitory 'gating' function between the neocortex and the hippocampus (de Curtis and Pare, 2004). In this formulation, perhaps the combination of inputs arriving directly from the neocortex and indirectly through the thalamus is necessary to overcome this inhibition and activate hippocampal circuits.

We observed that the waveform of hippocampal activity following septal inactivation was similar during both activated and deactivated states (Figure 4.4A, circled events and Figure 4.4C), as well as in the entorhinal cortex during spontaneous iota (Figure 4.10A, circled events). This waveform consisted of a short negative-going wave followed by a longer positive-going wave. A similar waveform was previously described in the hippocampus following the combination of carbachol and bicuculline infusions with intravenous atropine administration (cf. Figure 6, bottom right panel from Smythe et al., 1992). There is also a similarity to slow periodic events that were described in the entorhinal cortex of the isolated whole brain (cf. Figures 5A and 6B; Dickson et al., 2003). In the latter example, carbachol perfusion increased the frequency of the slow periodic events and decreased their amplitude until they disappeared and were replaced by gamma activity. Interestingly, the slow periodic events were reinstated by atropine. This parallels our findings in that the removal of cholinergic inputs from the medial septum unmasked ‘slow periodic events’ that we have called iota. Furthermore, in Dickson et al. (2003), these events were initially arrhythmic, resembling the activity we observed during the deactivated state, and their rhythmicity increased as their frequency increased, resembling the activity we observed during the activated state. It is therefore possible that iota represents a default activity pattern in entorhinal-hippocampal circuits that is present across all brain states but that is modulated to some degree by neuromodulatory inputs from the medial septum and other subcortical afferents.

In summary, we have described a novel hippocampal and entorhinal cortical activity pattern with a frequency of 0.1-0.5 Hz that we have termed iota. This rhythm appears to be present across both activated (theta) and deactivated (SO) brain states, and is coherent between superficial layers of the EC and SLM of CA1 in the hippocampus. Inactivation of the medial septum with lidocaine revealed large amplitude slow periodic events at iota frequency during the activated state, and similar, aperiodic events during the deactivated state. Notably, medial septal muscimol infusions mimicked lidocaine effects during activated but not deactivated states. This implicates fibers of passage through the medial septum in mediating the coordination of hippocampal and neocortical circuits during the SO. Taken together, our findings suggest that iota may represent a default activity pattern in the entorhinal-hippocampal circuit that influences the processing of information across both SO and theta states.

5 **Discussion**

Discussion

In this work I have focussed on patterns of oscillatory activity in the hippocampus during sleep-like states. Oscillatory synchronization in neuronal networks in general likely allows for the coordination of input and output pathways with high temporal precision, and this is a potential mechanism for the linking of distributed cell assemblies that may be important for such fundamental processes as perception, attention and memory (Gray et al., 1989; Mainen and Sejnowski, 1995; Stopfer et al., 1997; Engel et al., 1999; Buzsaki, 2006; Fries, 2015). During nonREM sleep, the ~1 Hz neocortical slow oscillation arises from coordinated alternations between activity and silence in neocortical neurons (Steriade et al., 1993a; Steriade et al., 1993d; Steriade et al., 1993b). Activity during this sleep state has been linked directly and indirectly to the consolidation of hippocampal-dependent memories (Meier-Koll et al., 1999; Eschenko et al., 2006; Molle et al., 2009; Born, 2010; Inostroza et al., 2013). Therefore, the motivating question for this thesis was how neocortical and hippocampal networks are coordinated during the SO.

Previous work in our lab and others' has shown that hippocampal networks are indeed coordinated with the neocortical SO, but that the hippocampal SO has properties that are unique from its neocortical counterpart (Sirota et al., 2003; Sirota and Buzsaki, 2005; Isomura et al., 2006; Wolansky et al., 2006). The coordination between the two structures appears to involve synaptic inputs arriving from the entorhinal cortex and potentially other regions, such as the nucleus reuniens of the thalamus. In the CA1 subfield, the precise timing of the entorhinal and reuniens inputs to the distal dendrites (SLM) relative to the inputs arriving from CA3 at stratum radiatum (SRad) is likely critical for information processing in this circuit. Indeed, during hippocampal theta activity, synaptic inputs to SLM and SRad have been shown to arrive at different phases of the theta oscillation (Colgin et al., 2009; Lasztoczi and Klausberger, 2014; Schomburg et al., 2014).

A potential mechanism for the strengthening of memories during sleep involves the reactivation of sequences of neuronal firing from awake behaviour during a specific hippocampal activity pattern occurring during nonREM sleep called the sharp wave-ripple (SPW-R; Skaggs and McNaughton, 1996; Lee and Wilson, 2002; O'Neill et al., 2006; O'Neill et al., 2008). SPW-Rs are comprised of a large depolarizing sharp wave in the Schaffer collateral projection from CA3 to SRad of CA1. This sharp wave triggers a ripple oscillation in the pyramidal cell layer, which is poised to shape the output of the hippocampal circuit (Buzsaki et al., 1983; Ylinen et al., 1995b; Csicsvari et al., 2000). It is during these ripple oscillations that the reactivation of pyramidal cell firing sequences has been observed. Online disruption of ripple oscillations during sleep has been shown to disrupt memory (Girardeau et al., 2009; Ego-Stengel and Wilson, 2010). Furthermore, the occurrence of SPW-Rs has been correlated with thalamocortical spindle oscillations in the neocortex, which have also been implicated in sleep-dependent memory processes (Siapas and Wilson, 1998; Sirota et al., 2003; Eschenko et al., 2006; Molle et al., 2009; Clemens et al., 2011).

Based on the above findings, the goal of my thesis was to understand the coordination of input and output pathways of the hippocampus with the neocortical SO. In addition, I wanted to compare the coordination of hippocampal networks during the SO to that seen during hippocampal theta oscillations, which occur during REM sleep and awake exploratory behaviour, in order to validate our methods and to directly compare the two states. To approach these questions, I used the urethane model for sleep. Animals anaesthetized with urethane display rhythmic alternations between an activated REM-like state characterized by hippocampal theta oscillations, and a deactivated nonREM-like state characterized by the neocortical and hippocampal SO (Wolansky et al., 2006; Clement et al., 2008), and this model therefore allows for the examination of both SO and theta oscillations in a highly controlled environment.

5.1 Separation of hippocampal input pathways using ICA

In Chapter 2, I described the methodological approach I used to examine hippocampal network activity patterns. Using independent component analysis (ICA) to decompose the local field potential recorded from a 16-channel linear probe in the dorsal hippocampus of urethane-anaesthetized rats into its underlying sources, I was able to consistently separate activity likely representing both local synaptic inputs and the volume-conducted signal from the overlying cortex. Based on the spatial profile of the separated components, as well as the stimulation of known afferent pathways, I putatively identified the components as representing activity in the medial perforant pathway (MPP*ic*), the lateral perforant pathway (LPP*ic*), the SLM-targeting entorhinal and nucleus reuniens inputs (SLM*ic*), and the Schaffer collateral pathway (SchC*ic*), as well as the volume conducted signal (VC*ic*). This approach has been described by other groups (Makarov et al., 2010; Schomburg et al., 2014), however my goal here was to demonstrate the reliability of ICA for analysis of hippocampal data across different algorithms, epochs and animals, and to discuss some practical considerations for ICA implementation including the improvements seen following pre-filtering to remove low frequencies from the signal. I then described how this approach can be used to remove the volume conducted artefact from the LFP, as well as to identify oscillatory activity patterns in separate pathways using a modification of the **B**etter **Osc**illation detection (BOSC) method (Caplan et al., 2001; Whitten et al., 2011; Hughes et al., 2012). These methods formed the basis for the remainder of my thesis.

5.2 Phase relationship of gamma frequency inputs to the neocortical SO

In Chapter 3, I employed the above methods to dissect the activity patterns in the hippocampal circuit and their coordination with the neocortical SO. We also assessed activity patterns during theta as a further validation of the ICA method, since the theta oscillation has been studied extensively in hippocampal networks, allowing us to compare our results using ICA to the previous literature (Colgin et al., 2009; Lasztoczi and Klausberger, 2014; Schomburg et al., 2014). We found first that gamma-frequency activity in the SLM*ic* and the SchC*ic* occurred at distinct phases relative to the neocortical slow oscillation. In particular, the SLM*ic* gamma activity *followed* the peak of the neocortical ON-state, while the SchC*ic* gamma activity *preceded* the peak of the neocortical ON-state. In the context of memory processing during SO states, this finding could relate to the idea that the membrane hyperpolarization during the periods of inactivity that define the OFF-states in neocortical neurons are critical for the potentiation of evoked potentials by SO-like firing patterns (Chauvette et al., 2012). If the OFF-state is critical for isolated neocortical effects on plasticity, perhaps it also provides a window for processing in the CA3 hippocampal subfield, where many cells are out of phase with the neocortical SO (Hahn et al., 2007). The Schaffer collateral output to CA1 following the OFF-state and preceding the next ON-state could then represent the output from this intrahippocampal processing.

5.3 Slow dynamics of hippocampal activity during both SO and theta

In Chapter 3 I also described that the major synaptic inputs arriving at SLM periodically skip cycles with respect to the neocortical SO. This pattern of cycle-skipping, though not entirely rhythmic, results in a slowing of the hippocampal LFP with respect to the neocortical SO. This could explain why hippocampal activity during deactivated states sometimes appears non-rhythmic, and was therefore called large-amplitude irregular activity (LIA; Whishaw and Vanderwolf, 1973), while at other times it follows the neocortical SO faithfully, producing the hippocampal SO (Wolansky et al., 2006). The phase relationship of synaptic inputs at SLM with the neocortical SO remains consistent, however the frequency of skipped cycles influences the rhythmicity of activity recorded in the hippocampus. With respect to memory processes in the hippocampus, it is possible that the entorhinal and parahippocampal cortices serve a gating function between the neocortex and the hippocampus, as has been suggested based on findings in the isolated whole brain (de Curtis and Pare, 2004), allowing only the strongest inputs to continue on to the hippocampal circuit.

Cycle skipping is also relevant for our finding in Chapter 4 that lidocaine infusions in the medial septum produced a very slow, periodic but arrhythmic activity pattern in the hippocampus during the deactivated state that remained phase-modulated by the neocortical SO. The finding that this effect was seen for lidocaine but not muscimol infusions suggested that it was mediated by fibers of passage through the medial septum, and not local cell bodies. The origin of these fibers cannot be unequivocally identified based on our data. Since the maximal effect was seen in the SLM*ic*, we speculated that we could be disrupting the thalamic input from the nucleus reuniens, which projects to SLM and has been suggested to provide a link between the medial prefrontal cortex and the hippocampus (Vertes et al., 2007; Varela et al., 2014). Thus, hippocampal coordination with the neocortex during the SO might require the combination of a direct input through the EC and an indirect input through the thalamus. However, since we cannot confirm that nucleus reuniens fibers were inactivated, this remains speculative until further studies are performed. Another possibility is that brainstem serotonergic fibers from the median raphé nucleus, which are known to travel through the medial septum, might be critical for the coordination of hippocampal and neocortical circuits during the SO (Vertes et al., 1999; McKenna and Vertes, 2001). Indeed, inhibition of the median raphé nucleus produces theta oscillations in the hippocampus (Kinney et al., 1994; Vertes et al., 1994; Kinney et al., 1995). Since we were also inhibiting theta oscillations by inactivating the medial septum, the slow periodic activity pattern that we observed might represent a default activity pattern of entorhinal-hippocampal circuits.

It is interesting to note that the slow 0.1-0.5 Hz peak frequency of the SLM*ic* that results from cycle skipping overlaps with the frequency of the iota rhythm described in Chapter 4. In spontaneous data, this rhythm was seen most prominently during transition states, however the power, coherence and phase profiles of the iota frequency activity were identical during both activated and deactivated states, suggesting that this slow modulation of spontaneous activity represents the same phenomenon across both states. During activated states, when the theta oscillation was disrupted following lidocaine or muscimol infusions in the medial septum, the iota rhythm was enhanced but maintained the same frequency and spatial profile as before inactivation. This profile included a reversal of phase 100 μm below the depth of the theta phase reversal. Interestingly, this spatial profile is identical to the spatial profile of SO-frequency activity in the hippocampus after removal of the volume-conducted component, as described in Chapter 2, suggesting that both SO- and iota- frequency hippocampal activity patterns are mediated by the same circuits.

Iota frequency activity was seen prominently during transition states in the EC, and was highly coherent with iota recorded in the HPC, especially at superficial layers. This corresponded well with the coherence profile of theta activity in the EC, although as in the hippocampus, the dip in coherence was 100 μm below the coherence dip/theta reversal. Multi-unit activity in the EC showed the strongest iota-modulation at layer III, representing the origin of the direct input to SLM, and iota activity in the EC tended to precede iota in the HPC. Therefore a picture emerged that iota activity results from direct interactions between entorhinal and hippocampal circuits.

Ultra-slow modulation of the interactions between hippocampal and neocortical networks were described previously (Sirota et al., 2003). Specifically, it was found that there was a 0.03-0.3 Hz modulation of both ripple oscillations in the hippocampus and spindle and delta (1-4 Hz) activity in the neocortex in naturally sleeping rats. Whether this was a manifestation of the iota-frequency modulation of hippocampal circuits that we have described is unclear. We found iota modulation of the synaptic inputs at SLM, whereas Sirota et al. (2003) were describing ultra-slow modulation of ripple occurrence in the pyramidal cell layers, corresponding to the output of the circuit. However, it is possible that the iota rhythm modulates the output of CA1 as well, which could link these two findings.

5.4 Relationship of SPW-Rs to the neocortical SO

Ripple oscillations occurring as a part of SPW-Rs modulate the firing of CA1 pyramidal cells and therefore represent the output of hippocampal circuits back to the neocortex. In the context of memory processes, this is therefore a critical step in the bidirectional flow of information between neocortical and hippocampal networks. In the work described in chapter 3, we found that the SO phase at which ripple oscillations occurred in the pyramidal cell layer of CA1 was modulated by the power of the SO in the neocortex. Specifically, ripples preceding the peak of the neocortical ON-state were associated with lower neocortical SO power, while ripples that followed the peak of the neocortical ON-state were associated with higher neocortical

SO power. Using different analysis methods, others have also found that hippocampal ripples could either lead or follow neocortical delta waves (Peyrache et al., 2011). This difference in phase (preceding or following the ON-state peak) is likely critical in determining how ripple-associated outputs will influence downstream neocortical networks. For example, neocortical spindle oscillations occur at the beginning of the ON-state, and Peyrache et al. (2011) found that SPW-Rs had a greater influence on gamma activity in the medial prefrontal cortex when they did not co-occur with spindle oscillations. They also postulated that neocortical cells might be more responsive to inputs arriving at the end of the ON-phase, due to an increase in input resistance. Thus, ripples occurring at the end of the ON-phase, which we found to be associated with higher power of the neocortical SO, might play a different role in hippocampal-neocortical communication than ripples occurring at the beginning of the ON-phase.

We also found in Chapter 4 that SPW-Rs sometimes occurred in clusters, and that these clusters occurred at spindle frequency, leading to a strong relationship between spindle phase and SPW-R occurrence in the pyramidal cell layer. Furthermore, these pyramidal layer ‘spindles’ were more likely than chance to co-occur with spindles in the hippocampal input layers. While we failed to find a relationship between spindles in the neocortex and SPW-Rs in the hippocampus as others have shown (Siapas and Wilson, 1998; Sirota et al., 2003), this could be due to the position of our electrode in the frontal cortex and the more local nature of spindle oscillations (Nir et al., 2011). Nevertheless, our finding of spindle oscillations in the input layers of the hippocampus under urethane anaesthesia mirrors recent findings in natural sleep (Sullivan et al., 2014), and likely represents yet another component of the interaction between neocortical and hippocampal circuits during slow oscillations.

5.5 Future directions

Although some questions have been answered here with respect to the coordination of hippocampal activity with the neocortical SO, some questions remain, and some of the findings described here have generated new questions that will be answered by future research. One important question that remains involves the role of the nucleus reuniens in mediating the coordination of the hippocampal SO. While anatomical studies clearly show a direct excitatory projection from the nucleus reuniens to SLM (Wouterlood et al., 1990; Bokor et al., 2002), and three groups have found evidence for evoked potentials at SLM following nucleus reuniens stimulation (Dolleman-Van der Weel et al., 1997; Bertram and Zhang, 1999; Viana Di Prisco et al., 2002), a direct link has not been shown between nucleus reuniens activity and the spontaneous hippocampal activity during deactivated states. Zhang et al. (2012) did show that single units in both structures are phase-modulated by slow wave activity following systemic ketamine administration and that the associated LFPs are highly coherent at slow frequencies. However, their results cannot differentiate between a direct influence of the nucleus reuniens on hippocampal activity versus the alternate possibility that both structures are being driven by neocortical inputs. Optogenetic techniques might provide an ideal method to directly answer this question. Although Duan et al. (2015) showed that optogenetic stimulation of SLM-targeting nucleus reuniens fibres at slow frequencies during awake behaviour disrupted online hippocampal function, they did not directly show the effect of this stimulation on hippocampal activity patterns. In future studies, the specific nucleus reuniens cells targeting SLM could be selectively suppressed or activated optogenetically during deactivated states, allowing the precise role of the nucleus reuniens in generating the hippocampal SO to be elucidated.

A second question that was not addressed here is the effect of septal inactivation with lidocaine on entorhinal cortex activity. While we found that iota activity can occur in the entorhinal cortex, that it is coordinated with iota in the hippocampus, and that it modulates the amplitude of spontaneous theta oscillations in the entorhinal cortex, we could not address whether iota is enhanced in the entorhinal cortex following septal inactivation as it is in the hippocampus. Given the strong coherence of iota activity between the hippocampus and the EC that we found, I would speculate that a strong iota activity pattern would also be seen in the EC circuits.

Another interesting finding that I described is the relationship between the phase of SPW-Rs and the power of the neocortical SO. An important future direction would be to replicate this finding in natural sleep, and then to determine if SPW-Rs occurring at different phases are differentially involved in sleep-dependent memory consolidation. The disruption of SPW-Rs using online detection and electrical stimulation has been shown to impair memory processes (Girardeau et al., 2009; Ego-Stengel and Wilson, 2010). One approach could be to selectively disrupt only SPW-Rs preceding the ON-state or only those following the ON-state during sleep following learning of a hippocampal-dependent task, and to determine if there are differential effects on memory.

5.6 Concluding statement

In the work described in this thesis I have used ICA to isolate activity patterns in the main hippocampal afferent pathways and to evaluate their relationship to the neocortical SO in order to understand how coordination between these networks might underlie critical memory processes occurring during nonREM sleep. While many aspects of this circuit have become clear, many important questions remain.

In the 140 years since Richard Caton suggested that ‘*the electric currents of the grey matter appear to have a relation to its function’* (Caton, 1875), we have made significant progress in understanding what that relationship is. However, the brain still retains its mystery, and many important facets of its electric currents still remain to be discovered.

REFERENCES

Alonso A, Garcia-Austt E (1987) Neuronal sources of theta rhythm in the entorhinal cortex of the rat. I. Laminar distribution of theta field potentials. Experimental brain research 67:493-501.

Amaral DG, Witter MP (1989) The three-dimensional organization of the hippocampal formation: a review of anatomical data. Neuroscience 31:571-591.

Amzica F, Steriade M (1995a) Short- and long-range neuronal synchronization of the slow (< 1 Hz) cortical oscillation. Journal of neurophysiology 73:20-38.

Amzica F, Steriade M (1995b) Disconnection of intracortical synaptic linkages disrupts synchronization of a slow oscillation. The Journal of neuroscience : the official journal of the Society for Neuroscience 15:4658-4677.

Amzica F, Steriade M (1997) The K-complex: its slow (<1-Hz) rhythmicity and relation to delta waves. Neurology 49:952-959.

Andersen P, Bliss TV, Skrede KK (1971) Lamellar organization of hippocampal pathways. Experimental brain research 13:222-238.

Andersen P, Morris R, Amaral D, Bliss T, O'Keefe J (2007) The hippocampus book. Oxford ; New York: Oxford University Press.

Aoki Y, Ishii R, Pascual-Marqui RD, Canuet L, Ikeda S, Hata M, Imajo K, Matsuzaki H, Musha T, Asada T, Iwase M, Takeda M (2015) Detection of EEG-resting state independent networks by eLORETA-ICA method. Frontiers in human neuroscience 9:31.

Arantius G (1587) De humano foetu. Ejusdem anatomicorum observationum liber, etc:44-45.

Aserinsky E, Kleitman N (1953) Regularly occurring periods of eye motility, and concomitant phenomena, during sleep. Science 118:273-274.

Axmacher N, Henseler MM, Jensen O, Weinreich I, Elger CE, Fell J (2010) Cross-frequency coupling supports multi-item working memory in the human hippocampus. Proceedings of the National Academy of Sciences of the United States of America 107:3228-3233.

Bell AJ, Sejnowski TJ (1995) An information-maximization approach to blind separation and blind deconvolution. Neural computation 7:1129-1159.

Benito N, Fernandez-Ruiz A, Makarov VA, Makarova J, Korovaichuk A, Herreras O (2014) Spatial modules of coherent activity in pathway-specific LFPs in the hippocampus reflect topology and different modes of presynaptic synchronization. Cerebral cortex 24:1738-1752.

Benson K, Feinberg I (1977) The beneficaial effect of sleep in an extended Jenkins and Dallenbach paradigm. Psychophysiology 14:375-384.

Berens P (2009) CircStat: A Matlab Toolbox for Circular Statistics. Journal of Statistical Software 31.

Berger H (1929) Uber das elektrenkephalogram des menschen. Arch Psychiatr Nervenkr 87:527-570.

Bertram EH, Zhang DX (1999) Thalamic excitation of hippocampal CA1 neurons: a comparison with the effects of CA3 stimulation. Neuroscience 92:15-26.

Binder S, Rawohl J, Born J, Marshall L (2014a) Transcranial slow oscillation stimulation during NREM sleep enhances acquisition of the radial maze task and modulates cortical network activity in rats. Frontiers in behavioral neuroscience 7:220.

Binder S, Berg K, Gasca F, Lafon B, Parra LC, Born J, Marshall L (2014b) Transcranial slow oscillation stimulation during sleep enhances memory consolidation in rats. Brain stimulation 7:508-515.

Bland BH (1986) The physiology and pharmacology of hippocampal formation theta rhythms. Progress in neurobiology 26:1-54.

Bland BH, Sainsbury RS, Creery BL (1979) Anatomical correlates of rhythmical slow wave activity (theta) in the hippocampal formation of the cat. Brain research 161:199-209.

Bland BH, Trepel C, Oddie SD, Kirk IJ (1996) Intraseptal microinfusion of muscimol: effects on hippocampal formation theta field activity and phasic theta-ON cell discharges. Experimental neurology 138:286-297.

Bokor H, Csaki A, Kocsis K, Kiss J (2002) Cellular architecture of the nucleus reuniens thalami and its putative aspartatergic/glutamatergic projection to the hippocampus and medial septum in the rat. The European journal of neuroscience 16:1227-1239.

Born J (2010) Slow-wave sleep and the consolidation of long-term memory. The world journal of biological psychiatry : the official journal of the World Federation of Societies of Biological Psychiatry 11 Suppl 1:16-21.

Bowers A, Saltuklaroglu T, Harkrider A, Cuellar M (2013) Suppression of the micro rhythm during speech and non-speech discrimination revealed by independent component analysis: implications for sensorimotor integration in speech processing. PloS one 8:e72024.

Bragin A, Jando G, Nadasdy Z, Hetke J, Wise K, Buzsaki G (1995) Gamma (40-100 Hz) oscillation in the hippocampus of the behaving rat. The Journal of neuroscience : the official journal of the Society for Neuroscience 15:47-60.

Buhry L, Azizi AH, Cheng S (2011) Reactivation, replay, and preplay: how it might all fit together. Neural plasticity 2011:203462.

Buzsaki G (1989) Two-stage model of memory trace formation: a role for "noisy" brain states. Neuroscience 31:551-570.

Buzsaki G (2002) Theta oscillations in the hippocampus. Neuron 33:325-340.

Buzsaki G (2006) Rhythms of the brain. Oxford ; New York: Oxford University Press.

Buzsaki G, Draguhn A (2004) Neuronal oscillations in cortical networks. Science 304:1926-1929.

Buzsaki G, Wang XJ (2012) Mechanisms of gamma oscillations. Annual review of neuroscience 35:203-225.

Buzsaki G, Moser EI (2013) Memory, navigation and theta rhythm in the hippocampal-entorhinal system. Nature neuroscience 16:130-138.

Buzsaki G, Mizuseki K (2014) The log-dynamic brain: how skewed distributions affect network operations. Nature reviews Neuroscience 15:264-278.

Buzsaki G, Leung LW, Vanderwolf CH (1983) Cellular bases of hippocampal EEG in the behaving rat. Brain research 287:139-171.

Buzsaki G, Anastassiou CA, Koch C (2012) The origin of extracellular fields and currents--EEG, ECoG, LFP and spikes. Nature reviews Neuroscience 13:407-420.

Buzsaki G, Logothetis N, Singer W (2013) Scaling brain size, keeping timing: evolutionary preservation of brain rhythms. Neuron 80:751-764.

Cajal SR (1899) Textura del sistema nervioso del hombre y de los vertebrados. Madrid.

Canolty RT, Knight RT (2010) The functional role of cross-frequency coupling. Trends in cognitive sciences 14:506-515.

Canolty RT, Edwards E, Dalal SS, Soltani M, Nagarajan SS, Kirsch HE, Berger MS, Barbaro NM, Knight RT (2006) High gamma power is phase-locked to theta oscillations in human neocortex. Science 313:1626-1628.

Caplan JB, Madsen JR, Raghavachari S, Kahana MJ (2001) Distinct patterns of brain oscillations underlie two basic parameters of human maze learning. Journal of neurophysiology 86:368-380.

Cardin JA, Carlen M, Meletis K, Knoblich U, Zhang F, Deisseroth K, Tsai LH, Moore CI (2009) Driving fast-spiking cells induces gamma rhythm and controls sensory responses. Nature 459:663-667.

Cardoso JF (1999) High-order contrasts for independent component analysis. Neural computation 11:157-192.

Carr MF, Frank LM (2012) A single microcircuit with multiple functions: state dependent information processing in the hippocampus. Current opinion in neurobiology 22:704-708.

Castellanos NP, Makarov VA (2006) Recovering EEG brain signals: artifact suppression with wavelet enhanced independent component analysis. Journal of neuroscience methods 158:300-312.

Caton R (1875) The electric currents of the brain. Br Med J Suppl I:62-65.

Chaumon M, Bishop DV, Busch NA (2015) A practical guide to the selection of independent components of the electroencephalogram for artifact correction. Journal of neuroscience methods 250:47-63.

Chauvette S, Seigneur J, Timofeev I (2012) Sleep oscillations in the thalamocortical system induce long-term neuronal plasticity. Neuron 75:1105-1113.

Chrobak JJ, Buzsaki G (1996) High-frequency oscillations in the output networks of the hippocampal-entorhinal axis of the freely behaving rat. The Journal of neuroscience : the official journal of the Society for Neuroscience 16:3056-3066.

Clemens Z, Fabo D, Halasz P (2005) Overnight verbal memory retention correlates with the number of sleep spindles. Neuroscience 132:529-535.

Clemens Z, Molle M, Eross L, Jakus R, Rasonyi G, Halasz P, Born J (2011) Fine-tuned coupling between human parahippocampal ripples and sleep spindles. The European journal of neuroscience 33:511-520.

Clement EA, Richard A, Thwaites M, Ailon J, Peters S, Dickson CT (2008) Cyclic and sleep-like spontaneous alternations of brain state under urethane anaesthesia. PloS one 3:e2004.

Colgin LL, Denninger T, Fyhn M, Hafting T, Bonnevie T, Jensen O, Moser MB, Moser EI (2009) Frequency of gamma oscillations routes flow of information in the hippocampus. Nature 462:353-357.

Corkin S (1968) Acquisition of motor skill after bilateral medial temporal-lobe excision. Neuropsychologia 6:255-265.

Croissant de Garengeot RJ (1742) Splanchnologie ou 1' anatomie de visceres, 2 Edition. Paris: Osmont.

Csicsvari J, Hirase H, Mamiya A, Buzsaki G (2000) Ensemble patterns of hippocampal CA3-CA1 neurons during sharp wave-associated population events. Neuron 28:585-594.

de Curtis M, Pare D (2004) The rhinal cortices: a wall of inhibition between the neocortex and the hippocampus. Progress in neurobiology 74:101-110.

Delorme A, Makeig S (2004) EEGLAB: an open source toolbox for analysis of single-trial EEG dynamics including independent component analysis. Journal of neuroscience methods 134:9-21.

Delorme A, Sejnowski T, Makeig S (2007) Enhanced detection of artifacts in EEG data using higher-order statistics and independent component analysis. NeuroImage 34:1443-1449.

Delorme A, Palmer J, Onton J, Oostenveld R, Makeig S (2012) Independent EEG sources are dipolar. PloS one 7:e30135.

Dement W (1958) The occurrence of low voltage, fast, electroencephalogram patterns during behavioral sleep in the cat. Electroencephalography and clinical neurophysiology 10:291-296.

Dement W, Kleitman N (1957) Cyclic variations in EEG during sleep and their relation to eye movements, body motility, and dreaming. Electroencephalography and clinical neurophysiology 9:673-690.

Dement WC (1990) A personal history of sleep disorders medicine. Journal of clinical neurophysiology : official publication of the American Electroencephalographic Society 7:17-47.

Dickson CT, Trepel C, Bland BH (1994) Extrinsic modulation of theta field activity in the entorhinal cortex of the anesthetized rat. Hippocampus 4:37-51.

Dickson CT, Biella G, de Curtis M (2000) Evidence for spatial modules mediated by temporal synchronization of carbachol-induced gamma rhythm in medial entorhinal cortex. The Journal of neuroscience : the official journal of the Society for Neuroscience 20:7846-7854.

Dickson CT, Biella G, de Curtis M (2003) Slow periodic events and their transition to gamma oscillations in the entorhinal cortex of the isolated Guinea pig brain. Journal of neurophysiology 90:39-46.

Dolleman-Van der Weel MJ, Witter MP (2000) Nucleus reuniens thalami innervates gamma aminobutyric acid positive cells in hippocampal field CA1 of the rat. Neuroscience letters 278:145-148.

Dolleman-Van der Weel MJ, Lopes da Silva FH, Witter MP (1997) Nucleus reuniens thalami modulates activity in hippocampal field CA1 through excitatory and inhibitory mechanisms. The Journal of neuroscience : the official journal of the Society for Neuroscience 17:5640-5650.

Dragoi G, Buzsaki G (2006) Temporal encoding of place sequences by hippocampal cell assemblies. Neuron 50:145-157.

Duan AR, Varela C, Zhang Y, Shen Y, Xiong L, Wilson MA, Lisman J (2015) Delta frequency optogenetic stimulation of the thalamic nucleus reuniens is sufficient to produce working memory deficits: relevance to schizophrenia. Biological psychiatry 77:1098-1107.

Ebbinghaus H (1885) Über das Gedächtnis. Untersuchungen zur experimentellen Psychologie. Leipzig,: Duncker & Humblot.

Ego-Stengel V, Wilson MA (2010) Disruption of ripple-associated hippocampal activity during rest impairs spatial learning in the rat. Hippocampus 20:1-10.

Eichenbaum H (2013) What H.M. taught us. Journal of cognitive neuroscience 25:14-21.

Eichenbaum H, Cohen NJ (2014) Can we reconcile the declarative memory and spatial navigation views on hippocampal function? Neuron 83:764-770.

Engel AK, Fries P, Konig P, Brecht M, Singer W (1999) Temporal binding, binocular rivalry, and consciousness. Consciousness and cognition 8:128-151.

Eschenko O, Molle M, Born J, Sara SJ (2006) Elevated sleep spindle density after learning or after retrieval in rats. The Journal of neuroscience : the official journal of the Society for Neuroscience 26:12914-12920.

Fernandez-Ruiz A, Herreras O (2013) Identifying the synaptic origin of ongoing neuronal oscillations through spatial discrimination of electric fields. Frontiers in computational neuroscience 7:5.

Fernandez-Ruiz A, Makarov VA, Herreras O (2012a) Sustained increase of spontaneous input and spike transfer in the CA3-CA1 pathway following long-term potentiation in vivo. Frontiers in neural circuits 6:71.

Fernandez-Ruiz A, Makarov VA, Benito N, Herreras O (2012b) Schaffer-specific local field potentials reflect discrete excitatory events at gamma frequency that may fire postsynaptic hippocampal CA1 units. The Journal of neuroscience : the official journal of the Society for Neuroscience 32:5165-5176.

Fernandez-Ruiz A, Munoz S, Sancho M, Makarova J, Makarov VA, Herreras O (2013) Cytoarchitectonic and dynamic origins of giant positive local field potentials in the dentate gyrus. The Journal of neuroscience : the official journal of the Society for Neuroscience 33:15518-15532.

Fowler MJ, Sullivan MJ, Ekstrand BR (1973) Sleep and memory. Science 179:302-304.

Freeman JA, Nicholson C (1975) Experimental optimization of current source-density technique for anuran cerebellum. Journal of neurophysiology 38:369-382.

Freund TF, Buzsaki G (1996) Interneurons of the hippocampus. Hippocampus 6:347-470.

Fries P (2015) Rhythms for Cognition: Communication through Coherence. Neuron 88:220-235.

Fries P, Nikolic D, Singer W (2007) The gamma cycle. Trends in neurosciences 30:309-316.

Girardeau G, Zugaro M (2011) Hippocampal ripples and memory consolidation. Current opinion in neurobiology 21:452-459.

Girardeau G, Benchenane K, Wiener SI, Buzsaki G, Zugaro MB (2009) Selective suppression of hippocampal ripples impairs spatial memory. Nature neuroscience 12:1222-1223.

Glabska H, Potworowski J, Leski S, Wojcik DK (2014) Independent components of neural activity carry information on individual populations. PloS one 9:e105071.

Goutagny R, Jackson J, Williams S (2009) Self-generated theta oscillations in the hippocampus. Nature neuroscience 12:1491-1493.

Gray CM, Singer W (1989) Stimulus-specific neuronal oscillations in orientation columns of cat visual cortex. Proceedings of the National Academy of Sciences of the United States of America 86:1698-1702.

Gray CM, Konig P, Engel AK, Singer W (1989) Oscillatory responses in cat visual cortex exhibit inter-columnar synchronization which reflects global stimulus properties. Nature 338:334-337.

Greenberg A, Dickson CT (2013) Spontaneous and electrically modulated spatiotemporal dynamics of the neocortical slow oscillation and associated local fast activity. NeuroImage 83:782-794.

Hahn TT, Sakmann B, Mehta MR (2007) Differential responses of hippocampal subfields to cortical up-down states. Proceedings of the National Academy of Sciences of the United States of America 104:5169-5174.

Hahn TT, McFarland JM, Berberich S, Sakmann B, Mehta MR (2012) Spontaneous persistent activity in entorhinal cortex modulates cortico-hippocampal interaction in vivo. Nature neuroscience 15:1531-1538.

Hasselmo ME, Stern CE (2014) Theta rhythm and the encoding and retrieval of space and time. NeuroImage 85 Pt 2:656-666.

Hasselmo ME, Bodelon C, Wyble BP (2002) A proposed function for hippocampal theta rhythm: separate phases of encoding and retrieval enhance reversal of prior learning. Neural computation 14:793-817.

Hiltunen T, Kantola J, Abou Elseoud A, Lepola P, Suominen K, Starck T, Nikkinen J, Remes J, Tervonen O, Palva S, Kiviniemi V, Palva JM (2014) Infra-slow EEG fluctuations are correlated with resting-state network dynamics in fMRI. The Journal of neuroscience : the official journal of the Society for Neuroscience 34:356-362.

Hughes AM, Whitten TA, Caplan JB, Dickson CT (2012) BOSC: a better oscillation detection method, extracts both sustained and transient rhythms from rat hippocampal recordings. Hippocampus 22:1417-1428.

Hyafil A, Giraud AL, Fontolan L, Gutkin B (2015) Neural Cross-Frequency Coupling: Connecting Architectures, Mechanisms, and Functions. Trends in neurosciences 38:725-740.

Hyvarinen A (1999a) Fast and robust fixed-point algorithms for independent component analysis. IEEE transactions on neural networks / a publication of the IEEE Neural Networks Council 10:626-634.

Hyvarinen A (1999b) Survey on Independent Component Analysis. Neural Computing Surveys 2:94-128.

Hyvarinen A, Oja E (2000) Independent component analysis: algorithms and applications. Neural networks : the official journal of the International Neural Network Society 13:411-430.

Inostroza M, Binder S, Born J (2013) Sleep-dependency of episodic-like memory consolidation in rats. Behavioural brain research 237:15-22.

Isomura Y, Sirota A, Ozen S, Montgomery S, Mizuseki K, Henze DA, Buzsaki G (2006) Integration and segregation of activity in entorhinal-hippocampal subregions by neocortical slow oscillations. Neuron 52:871-882.

Jacobs J (2014) Hippocampal theta oscillations are slower in humans than in rodents: implications for models of spatial navigation and memory. Philosophical transactions of the Royal Society of London Series B, Biological sciences 369:20130304.

Jenkins JG, Dallenbach KM (1924) Obliviscence during Sleep and Waking. The American Journal of Psychology 35:605-612.

Jung TP, Makeig S, McKeown MJ, Bell AJ, Lee TW, Sejnowski TJ (2001) Imaging Brain Dynamics Using Independent Component Analysis. Proceedings of the IEEE Institute of Electrical and Electronics Engineers 89:1107-1122.

Jung TP, Makeig S, Humphries C, Lee TW, McKeown MJ, Iragui V, Sejnowski TJ (2000) Removing electroencephalographic artifacts by blind source separation. Psychophysiology 37:163-178.

Ketchum KL, Haberly LB (1993) Membrane currents evoked by afferent fiber stimulation in rat piriform cortex. I. Current source-density analysis. Journal of neurophysiology 69:248-260.

Kinney GG, Kocsis B, Vertes RP (1994) Injections of excitatory amino acid antagonists into the median raphe nucleus produce hippocampal theta rhythm in the urethane-anesthetized rat. Brain research 654:96-104.

Kinney GG, Kocsis B, Vertes RP (1995) Injections of muscimol into the median raphe nucleus produce hippocampal theta rhythm in the urethane anesthetized rat. Psychopharmacology 120:244-248.

Klausberger T (2009) GABAergic interneurons targeting dendrites of pyramidal cells in the CA1 area of the hippocampus. The European journal of neuroscience 30:947-957.

Kramer MA, Tort AB, Kopell NJ (2008) Sharp edge artifacts and spurious coupling in EEG frequency comodulation measures. Journal of neuroscience methods 170:352-357.

Kramis R, Vanderwolf CH, Bland BH (1975) Two types of hippocampal rhythmical slow activity in both the rabbit and the rat: relations to behavior and effects of atropine, diethyl ether, urethane, and pentobarbital. Experimental neurology 49:58-85.

Kunec S, Hasselmo ME, Kopell N (2005) Encoding and retrieval in the CA3 region of the hippocampus: a model of theta-phase separation. Journal of neurophysiology 94:70-82.

Lasztoczi B, Klausberger T (2014) Layer-specific GABAergic control of distinct gamma oscillations in the CA1 hippocampus. Neuron 81:1126-1139.

Lavenex P, Amaral DG (2000) Hippocampal-neocortical interaction: a hierarchy of associativity. Hippocampus 10:420-430.

Lawson VH, Bland BH (1993) The role of the septohippocampal pathway in the regulation of hippocampal field activity and behavior: analysis by the intraseptal microinfusion of carbachol, atropine, and procaine. Experimental neurology 120:132-144.

Lee AK, Wilson MA (2002) Memory of sequential experience in the hippocampus during slow wave sleep. Neuron 36:1183-1194.

Lee TW, Girolami M, Sejnowski TJ (1999) Independent component analysis using an extended infomax algorithm for mixed subgaussian and supergaussian sources. Neural computation 11:417-441.

Lisman J, Buzsaki G (2008) A neural coding scheme formed by the combined function of gamma and theta oscillations. Schizophrenia bulletin 34:974-980.

Lisman JE, Jensen O (2013) The theta-gamma neural code. Neuron 77:1002-1016.

Loomis AL, Harvey EN, Hobart G (1935a) Further Observations on the Potential Rhythms of the Cerebral Cortex during Sleep. Science 82:198-200.

Loomis AL, Harvey EN, Hobart G (1935b) Potential Rhythms of the Cerebral Cortex during Sleep. Science 81:597-598.

Lorente de No R (1934) Studies on the structure of the cerebral cortex. II. Continuation of the study of the ammonic system. J Psychol Neurol:113-177.

Mainen ZF, Sejnowski TJ (1995) Reliability of spike timing in neocortical neurons. Science 268:1503-1506.

Makarov VA, Makarova J, Herreras O (2010) Disentanglement of local field potential sources by independent component analysis. Journal of computational neuroscience 29:445-457.

Makarova J, Ibarz JM, Makarov VA, Benito N, Herreras O (2011) Parallel readout of pathway-specific inputs to laminated brain structures. Frontiers in systems neuroscience 5:77.

Makarova J, Ortuno T, Korovaichuk A, Cudeiro J, Makarov VA, Rivadulla C, Herreras O (2014) Can pathway-specific LFPs be obtained in cytoarchitectonically complex structures? Frontiers in systems neuroscience 8:66.

Makeig S, Bell AJ, Jung T-P, Sejnowski TJ (1996) Independent component analysis of electroencephalographic data. In: Advances in Neural Information Processing Systems (Touretzky D, Mozer M, Hasselmo M, eds), pp 145-151. Cambridge, MA, USA: MIT Press.

Manns JR, Eichenbaum H (2006) Evolution of declarative memory. Hippocampus 16:795-808.

Marshall L, Helgadottir H, Molle M, Born J (2006) Boosting slow oscillations during sleep potentiates memory. Nature 444:610-613.

Martin-Vazquez G, Makarova J, Makarov VA, Herreras O (2013) Determining the true polarity and amplitude of synaptic currents underlying gamma oscillations of local field potentials. PloS one 8:e75499.

Massimini M, Huber R, Ferrarelli F, Hill S, Tononi G (2004) The sleep slow oscillation as a traveling wave. The Journal of neuroscience : the official journal of the Society for Neuroscience 24:6862-6870.

McKenna JT, Vertes RP (2001) Collateral projections from the median raphe nucleus to the medial septum and hippocampus. Brain research bulletin 54:619-630.

Meier-Koll A, Bussmann B, Schmidt C, Neuschwander D (1999) Walking through a maze alters the architecture of sleep. Perceptual and motor skills 88:1141-1159.

Milne E, Scope A, Pascalis O, Buckley D, Makeig S (2009) Independent component analysis reveals atypical electroencephalographic activity during visual perception in individuals with autism. Biological psychiatry 65:22-30.

Milner B (2005) The medial temporal-lobe amnesic syndrome. The Psychiatric clinics of North America 28:599-611, 609.

Mitzdorf U (1985) Current source-density method and application in cat cerebral cortex: investigation of evoked potentials and EEG phenomena. Physiological reviews 65:37-100.

Molle M, Eschenko O, Gais S, Sara SJ, Born J (2009) The influence of learning on sleep slow oscillations and associated spindles and ripples in humans and rats. The European journal of neuroscience 29:1071-1081.

Montgomery SM, Sirota A, Buzsaki G (2008) Theta and gamma coordination of hippocampal networks during waking and rapid eye movement sleep. The Journal of neuroscience : the official journal of the Society for Neuroscience 28:6731-6741.

Monto S, Palva S, Voipio J, Palva JM (2008) Very slow EEG fluctuations predict the dynamics of stimulus detection and oscillation amplitudes in humans. The Journal of neuroscience : the official journal of the Society for Neuroscience 28:8268-8272.

Moore RY, Halaris AE (1975) Hippocampal innervation by serotonin neurons of the midbrain raphe in the rat. The Journal of comparative neurology 164:171-183.

Nadasdy Z, Hirase H, Czurko A, Csicsvari J, Buzsaki G (1999) Replay and time compression of recurring spike sequences in the hippocampus. The Journal of neuroscience : the official journal of the Society for Neuroscience 19:9497-9507.

Nadel L, Moscovitch M (2001) The hippocampal complex and long-term memory revisited. Trends in cognitive sciences 5:228-230.

Nazer F, Dickson CT (2009) Slow oscillation state facilitates epileptiform events in the hippocampus. Journal of neurophysiology 102:1880-1889.

Ngo HV, Martinetz T, Born J, Molle M (2013) Auditory closed-loop stimulation of the sleep slow oscillation enhances memory. Neuron 78:545-553.

Nir Y, Staba RJ, Andrillon T, Vyazovskiy VV, Cirelli C, Fried I, Tononi G (2011) Regional slow waves and spindles in human sleep. Neuron 70:153-169.

O'Keefe J, Dostrovsky J (1971) The hippocampus as a spatial map. Preliminary evidence from unit activity in the freely-moving rat. Brain research 34:171-175.

O'Neill J, Senior T, Csicsvari J (2006) Place-selective firing of CA1 pyramidal cells during sharp wave/ripple network patterns in exploratory behavior. Neuron 49:143-155.

O'Neill J, Pleydell-Bouverie B, Dupret D, Csicsvari J (2010) Play it again: reactivation of waking experience and memory. Trends in neurosciences 33:220-229.

O'Neill J, Senior TJ, Allen K, Huxter JR, Csicsvari J (2008) Reactivation of experience-dependent cell assembly patterns in the hippocampus. Nature neuroscience 11:209-215.

Palva JM, Palva S (2012) Infra-slow fluctuations in electrophysiological recordings, blood-oxygenation-level-dependent signals, and psychophysical time series. NeuroImage 62:2201-2211.

Papatheodoropoulos C (2010) Patterned activation of hippocampal network (approximately 10 Hz) during in vitro sharp wave-ripples. Neuroscience 168:429-442.

Penttonen M, Nurminen N, Miettinen R, Sirvio J, Henze DA, Csicsvari J, Buzsaki G (1999) Ultra-slow oscillation (0.025 Hz) triggers hippocampal afterdischarges in Wistar rats. Neuroscience 94:735-743.

Peyrache A, Battaglia FP, Destexhe A (2011) Inhibition recruitment in prefrontal cortex during sleep spindles and gating of hippocampal inputs. Proceedings of the National Academy of Sciences of the United States of America 108:17207-17212.

Pignatelli M, Beyeler A, Leinekugel X (2012) Neural circuits underlying the generation of theta oscillations. Journal of physiology, Paris 106:81-92.

Plihal W, Born J (1997) Effects of early and late nocturnal sleep on declarative and procedural memory. Journal of cognitive neuroscience 9:534-547.

Pritchard WS (1992) The brain in fractal time: 1/f-like power spectrum scaling of the human electroencephalogram. The International journal of neuroscience 66:119-129.

Rasch B, Born J (2013) About sleep's role in memory. Physiological reviews 93:681-766.

Roberts PD, Bell CC (2002) Spike timing dependent synaptic plasticity in biological systems. Biological cybernetics 87:392-403.

Rodriguez R, Haberly LB (1989) Analysis of synaptic events in the opossum piriform cortex with improved current source-density techniques. Journal of neurophysiology 61:702-718.

Saunders RC, Aggleton JP (2007) Origin and topography of fibers contributing to the fornix in macaque monkeys. Hippocampus 17:396-411.

Sceniak MP, MacIver MB (2006) Cellular actions of urethane on rat visual cortical neurons in vitro. Journal of neurophysiology 95:3865-3874.

Scheffer-Teixeira R, Belchior H, Leao RN, Ribeiro S, Tort AB (2013) On high-frequency field oscillations (>100 Hz) and the spectral leakage of spiking activity. The Journal of neuroscience : the official journal of the Society for Neuroscience 33:1535-1539.

Schiller D, Eichenbaum H, Buffalo EA, Davachi L, Foster DJ, Leutgeb S, Ranganath C (2015) Memory and Space: Towards an Understanding of the Cognitive Map. The Journal of neuroscience : the official journal of the Society for Neuroscience 35:13904-13911.

Schomburg EW (2014) Biophysical and network mechanisms of high frequency extracellular potentials in the rat hippocampus. Disstertation (PhD). In. http://resolver.caltech.edu/CaltechTHESIS:05202014-055842097: California Institute of Technology.

Schomburg EW, Fernandez-Ruiz A, Mizuseki K, Berenyi A, Anastassiou CA, Koch C, Buzsaki G (2014) Theta Phase Segregation of Input-Specific Gamma Patterns in Entorhinal-Hippocampal Networks. Neuron.

Schultz C, Engelhardt M (2014) Anatomy of the hippocampal formation. Frontiers of neurology and neuroscience 34:6-17.

Scoville WB, Milner B (1957) Loss of recent memory after bilateral hippocampal lesions. Journal of neurology, neurosurgery, and psychiatry 20:11-21.

Shadlen MN, Newsome WT (1994) Noise, neural codes and cortical organization. Current opinion in neurobiology 4:569-579.

Siapas AG, Wilson MA (1998) Coordinated interactions between hippocampal ripples and cortical spindles during slow-wave sleep. Neuron 21:1123-1128.

Siapas AG, Lubenov EV, Wilson MA (2005) Prefrontal phase locking to hippocampal theta oscillations. Neuron 46:141-151.

Sidman M, Stoddard LT, Mohr JP (1968) Some Additional Quantitative Observations of Immediate Memory in a Patient with Bilateral Hippocampal Lesions. Neuropsychologia 6:245-254.

Sirota A, Buzsaki G (2005) Interaction between neocortical and hippocampal networks via slow oscillations. Thalamus & related systems 3:245-259.

Sirota A, Csicsvari J, Buhl D, Buzsaki G (2003) Communication between neocortex and hippocampus during sleep in rodents. Proceedings of the National Academy of Sciences of the United States of America 100:2065-2069.

Skaggs WE, McNaughton BL (1996) Replay of neuronal firing sequences in rat hippocampus during sleep following spatial experience. Science 271:1870-1873.

Sloviter RS, Lomo T (2012) Updating the lamellar hypothesis of hippocampal organization. Frontiers in neural circuits 6:102.

Smythe JW, Colom LV, Bland BH (1992) The extrinsic modulation of hippocampal theta depends on the coactivation of cholinergic and GABA-ergic medial septal inputs. Neuroscience and biobehavioral reviews 16:289-308.

Smythe JW, Cristie BR, Colom LV, Lawson VH, Bland BH (1991) Hippocampal theta field activity and theta-on/theta-off cell discharges are controlled by an ascending hypothalamo-septal pathway. The Journal of neuroscience : the official journal of the Society for Neuroscience 11:2241-2248.

Steriade M (2001) Impact of network activities on neuronal properties in corticothalamic systems. Journal of neurophysiology 86:1-39.

Steriade M, Amzica F, Nunez A (1993a) Cholinergic and noradrenergic modulation of the slow (approximately 0.3 Hz) oscillation in neocortical cells. Journal of neurophysiology 70:1385-1400.

Steriade M, Nunez A, Amzica F (1993b) A novel slow (< 1 Hz) oscillation of neocortical neurons in vivo: depolarizing and hyperpolarizing components. The Journal of neuroscience : the official journal of the Society for Neuroscience 13:3252-3265.

Steriade M, Nunez A, Amzica F (1993c) Intracellular analysis of relations between the slow (< 1 Hz) neocortical oscillation and other sleep rhythms of the electroencephalogram. The Journal of neuroscience : the official journal of the Society for Neuroscience 13:3266-3283.

Steriade M, Timofeev I, Grenier F (2001) Natural waking and sleep states: a view from inside neocortical neurons. Journal of neurophysiology 85:1969-1985.

Steriade M, Contreras D, Curro Dossi R, Nunez A (1993d) The slow (< 1 Hz) oscillation in reticular thalamic and thalamocortical neurons: scenario of sleep rhythm generation in interacting thalamic and neocortical networks. The Journal of neuroscience : the official journal of the Society for Neuroscience 13:3284-3299.

Steward O (1976) Topographic organization of the projections from the entorhinal area to the hippocampal formation of the rat. The Journal of comparative neurology 167:285-314.

Stopfer M, Bhagavan S, Smith BH, Laurent G (1997) Impaired odour discrimination on desynchronization of odour-encoding neural assemblies. Nature 390:70-74.

Sullivan D, Mizuseki K, Sorgi A, Buzsaki G (2014) Comparison of sleep spindles and theta oscillations in the hippocampus. The Journal of neuroscience : the official journal of the Society for Neuroscience 34:662-674.

Sullivan D, Csicsvari J, Mizuseki K, Montgomery S, Diba K, Buzsaki G (2011) Relationships between hippocampal sharp waves, ripples, and fast gamma oscillation: influence of dentate and entorhinal cortical activity. The Journal of neuroscience : the official journal of the Society for Neuroscience 31:8605-8616.

Tallon-Baudry C, Bertrand O (1999) Oscillatory gamma activity in humans and its role in object representation. Trends in cognitive sciences 3:151-162.

Tort AB, Komorowski R, Eichenbaum H, Kopell N (2010) Measuring phase-amplitude coupling between neuronal oscillations of different frequencies. Journal of neurophysiology 104:1195-1210.

Tort AB, Komorowski RW, Manns JR, Kopell NJ, Eichenbaum H (2009) Theta-gamma coupling increases during the learning of item-context associations. Proceedings of the National Academy of Sciences of the United States of America 106:20942-20947.

Vanderwolf CH (1969) Hippocampal electrical activity and voluntary movement in the rat. Electroencephalography and clinical neurophysiology 26:407-418.

Varela C, Kumar S, Yang JY, Wilson MA (2014) Anatomical substrates for direct interactions between hippocampus, medial prefrontal cortex, and the thalamic nucleus reuniens. Brain structure & function 219:911-929.

Vertes RP (2015) Major diencephalic inputs to the hippocampus: supramammillary nucleus and nucleus reuniens. Circuitry and function. Progress in brain research 219:121-144.

Vertes RP, Eastman KE (2000) The case against memory consolidation in REM sleep. The Behavioral and brain sciences 23:867-876; discussion 904-1121.

Vertes RP, McKenna JT (2000) Collateral projections from the supramammillary nucleus to the medial septum and hippocampus. Synapse 38:281-293.

Vertes RP, Fortin WJ, Crane AM (1999) Projections of the median raphe nucleus in the rat. The Journal of comparative neurology 407:555-582.

Vertes RP, Hoover WB, Viana Di Prisco G (2004) Theta rhythm of the hippocampus: subcortical control and functional significance. Behavioral and cognitive neuroscience reviews 3:173-200.

Vertes RP, Kinney GG, Kocsis B, Fortin WJ (1994) Pharmacological suppression of the median raphe nucleus with serotonin1A agonists, 8-OH-DPAT and buspirone, produces hippocampal theta rhythm in the rat. Neuroscience 60:441-451.

Vertes RP, Hoover WB, Szigeti-Buck K, Leranth C (2007) Nucleus reuniens of the midline thalamus: link between the medial prefrontal cortex and the hippocampus. Brain research bulletin 71:601-609.

Viana Di Prisco G, Albo Z, Vertes RP, Kocsis B (2002) Discharge properties of neurons of the median raphe nucleus during hippocampal theta rhythm in the rat. Experimental brain research 145:383-394.

Viczko J, Sharma AV, Pagliardini S, Wolansky T, Dickson CT (2014) Lack of respiratory coupling with neocortical and hippocampal slow oscillations. The Journal of neuroscience : the official journal of the Society for Neuroscience 34:3937-3946.

Waldert S, Lemon RN, Kraskov A (2013) Influence of spiking activity on cortical local field potentials. The Journal of physiology 591:5291-5303.

Wang G, Teng C, Li K, Zhang Z, Yan X (2015) The Removal of EOG Artifacts from EEG Signals Using Independent Component Analysis and Multivariate Empirical Mode Decomposition. IEEE journal of biomedical and health informatics.

Watrous AJ, Lee DJ, Izadi A, Gurkoff GG, Shahlaie K, Ekstrom AD (2013) A comparative study of human and rat hippocampal low-frequency oscillations during spatial navigation. Hippocampus 23:656-661.

Whishaw IQ, Vanderwolf CH (1973) Hippocampal EEG and behavior: changes in amplitude and frequency of RSA (theta rhythm) associated with spontaneous and learned movement patterns in rats and cats. Behavioral biology 8:461-484.

Whitten TA, Hughes AM, Dickson CT, Caplan JB (2011) A better oscillation detection method robustly extracts EEG rhythms across brain state changes: the human alpha rhythm as a test case. NeuroImage 54:860-874.

Wilson MA, McNaughton BL (1994) Reactivation of hippocampal ensemble memories during sleep. Science 265:676-679.

Winslow JB (1732) Exposition anatomique de la structure du corps humain. Paris: G. Desprez, J. Desessartz.

Winson J (1978) Loss of hippocampal theta rhythm results in spatial memory deficit in the rat. Science 201:160-163.

Wolansky T, Clement EA, Peters SR, Palczak MA, Dickson CT (2006) Hippocampal slow oscillation: a novel EEG state and its coordination with ongoing neocortical activity. The Journal of neuroscience : the official journal of the Society for Neuroscience 26:6213-6229.

Woolf V, Nicolson N, Banks JT (1975) The letters of Virginia Woolf. London: Hogarth Press.

Wouterlood FG, Saldana E, Witter MP (1990) Projection from the nucleus reuniens thalami to the hippocampal region: light and electron microscopic tracing study in the rat with the anterograde tracer Phaseolus vulgaris-leucoagglutinin. The Journal of comparative neurology 296:179-203.

Yaroush R, Sullivan MJ, Ekstrand BR (1971) Effect of sleep on memory. II. Differential effect of the first and second half of the night. Journal of experimental psychology 88:361-366.

Ylinen A, Soltesz I, Bragin A, Penttonen M, Sik A, Buzsaki G (1995a) Intracellular correlates of hippocampal theta rhythm in identified pyramidal cells, granule cells, and basket cells. Hippocampus 5:78-90.

Ylinen A, Bragin A, Nadasdy Z, Jando G, Szabo I, Sik A, Buzsaki G (1995b) Sharp wave-associated high-frequency oscillation (200 Hz) in the intact hippocampus: network and intracellular mechanisms. The Journal of neuroscience : the official journal of the Society for Neuroscience 15:30-46.

Zar JH (2010) Biostatistical Analysis, 5 Edition. Upper Saddle River, NJ, USA: Prentice Hall, Inc.

Zhang Y, Yoshida T, Katz DB, Lisman JE (2012) NMDAR antagonist action in thalamus imposes delta oscillations on the hippocampus. Journal of neurophysiology 107:3181-3189.